

# **Corrosion Mechanisms of Diamond-like Carbon Coated Interlayers & Interfaces**

**Thèse N° 7487**

Présentée le 23 septembre 2019

à la Faculté des sciences et techniques de l'ingénieur  
Groupe SCI STI SM  
Programme doctoral en science et génie des matériaux

pour l'obtention du grade de Docteur ès Sciences

par

**Emilija ILIĆ**

Acceptée sur proposition du jury

Prof. F. Nüesch, président du jury  
Dr. S. Mischler, Dr R. Hauert, directeurs de thèse  
Prof. C. Olsson, rapporteur  
Prof. S. Virtanen, rapporteuse  
Prof. V. Tileli, rapporteuse

2019

*To my parents, Andjelka Mastilo-Ilić and Nenad Ilić*

*Za mamu i tatu*

# Acknowledgements

This thesis work was performed at the Swiss Federal Laboratories for Materials Science and Technology (Empa) in the Laboratory for Joining Technologies and Corrosion, in collaboration with the École Polytechnique Fédérale de Lausanne (EPFL) Tribology and Interfacial Chemistry Group.

I would first like to express my gratitude to my Empa supervisors Dr. Roland Hauert and Dr. Patrik Schmutz for providing me with this opportunity and for their continuous support and guidance, also to Dr. Lars Jeurgens for welcoming me into the laboratory. Thank you also to my EPFL supervisor Prof. Stefano Mischler for his support and for allowing me to pursue my PhD degree in the EDMX doctoral program.

Thank you to Dr. Thomas Suter for his training in micro-electrochemical techniques, as well as Martin Sauder for training me in sample preparation and surface characterization.

A particular thanks to Dr. Ainhoa Pardo for our close collaboration and PhD advice during her two years at Empa, as well to Dr. Noemie Ott for translation of the abstract.

I would like to thank all of my current and former Empa colleagues who contributed to this work either by providing technical/administrative support, training, and measurements or by keeping me cheerful with their friendship. Thank you to, Claudia Frey, Arie Bruinink, Tobias Burgdorf, Claudia Cancellieri, Lars Dörner, Markus Faller, Miriam Gonzalez, Urs Gfeller, Olga Guseva, Ulrik Hans, Alexandra Lau, Ronald Lay, Luchan Lin, Bastian Rheingans, Sebastian Siol, Martin Tuchscheid, Yeliz Unutulmazsoy, Thomas Geldmacher, David Hahn, Mirco Chiodi, Nikola Gojkovic, Valerie Kroeni, Fabio Evangelisti, and Adrian Lis. Thanks Lisa Neu and Caitlin Proctor from Eawag for the Agar and for the fun outings.

In addition, I do not want to forget the EPFL Tribology and Interfacial Chemistry Group for their helpful feedback on presentations as well for their friendship and nice times. Thank you to, Anna Igual-Munoz, Laili Batooli, Angela Bermudez Castaneda, Fabio Cova Caiazza and Valentine Magnin.

Finally, thank you to the Swiss National Science Foundation (SNSF) for financially supporting this project (number 200021\_156085), as well to the jury member; Prof. Frank Nüesch, Prof. Sannakaisa Virtanen, Prof. Claes Olsson, and Prof. Vasiliki Tileli for taking the time to evaluate this thesis work.

# Abstract

Diamond-like carbon (DLC) coatings can improve the wear resistance of articulating implants. However despite successful in-vitro testing, some DLC coated joint replacements had to be revised prematurely, mainly due to coating delamination induced by corrosion at the substrate/DLC interface. Body fluid will enter defective coating sites and if the reactively formed interface or interlayer materials are instable in the confined fluid, they will dissolve, resulting in delamination of the DLC and ultimate failure of the implant.

The aim of this thesis is therefore to investigate the corrosion mechanisms responsible for delamination at a substrate/DLC interface in body-like media. This is achieved by developing and implementing experimental methodologies addressing/simulating aggravating factors such as confinements/crevices, galvanic coupling, stress and fatigue on the interface to investigate corrosion initiation, propagation, and failure.

Firstly, corrosion initiation and galvanic coupling risk are addressed with a methodology for accessing and characterizing the reactivity of buried interlayers. The interlayer is revealed by ion beam polishing, forming a wedge-like profile of the substrate/interlayer/DLC. The composition and chemical state of the interlayer/interface is determined by Auger electron spectroscopy. Reactive interlayers/interfaces, Si, titanium (Ti) and chromium (Cr), formed new phases (carbides and oxides). These new materials are then characterized with a local-electrochemical microcapillary technique. Cr and Si-DLC based interlayers presented good passive behavior, while a Si interlayer corroded in bovine-based wear test fluid (HyClone® WTF). The influence of coating defects on the current response of DLC surfaces was also investigated by varying the exposed working area ( $\text{cm}^2$  to  $\mu\text{m}^2$  range).

To address the failure case of a TiAlV/Si/DLC implant, the influence of confinements/crevices on corrosion propagation is investigated. It is shown that Si is highly vulnerable to corrosion in confined conditions. Pitting corrosion susceptibility is found in a crevice, whereas a Si dissolution rate of ca. 3.6 nm/h at 37 °C occurs within a confined area. The corrosion rates increased at elevated temperatures and yielded linear Arrhenius relations, with activation energies of 106 KJ/mol in phosphate buffered saline (PBS) and 109 KJ/mol in HyClone® WTF. Phosphorous species enhanced Si dissolution, while chlorides were not so influential. Galvanic coupling with Ti and applied stress further accelerated the Si dissolution.

Finally, corrosion related fracture of a CoCrMo/DLC interface is investigated by applying static and cyclic load. A reciprocating sliding rig is utilized to determine the number of sliding cycles required for interface delamination to occur at a critical load, in PBS at 37 °C. The results followed a Wöhler curve relation. Small  $\text{O}_2$  contaminations (0.5 and 1.0%) at the interface adversely affected the CF behavior by lowering the critical load and endurance limit. The fitted Wöhler curves could be extrapolated and were found to be in good agreement with long-term experimental results previously obtained on an implant in a spinal disk simulator.

## Keywords

DLC coating, interface, interlayer, silicon, crevice corrosion, corrosion fatigue, electrochemistry microcapillary technique, surface analysis.

# Résumé

Les revêtements de carbone de type diamant (DLC) permettent d'améliorer la résistance à l'usure des prothèses d'articulation. Malgré des tests in-vitro concluants, les implants revêtus de DLC faillissent, notamment dus au décollement prématuré du revêtement DLC causé par des attaques de corrosion à l'interface. Le liquide physiologique pénètre dans les défauts du revêtement et si cette interface (couche réactionnelle ou couche d'adhésion intermédiaire) n'est pas stable dans le fluide agressif développé dans le confinement, elle se dégrade, provoquant le décollement du revêtement DLC et donc la défaillance de l'implant.

Le but de cette thèse est de déterminer les mécanismes de corrosion qui mènent au décollement du revêtement DLC en milieu physiologique. Différentes procédures de caractérisation adressant des facteurs aggravants tels que milieux confinés/crevasse, couplages galvaniques, contraintes mécaniques ont donc été développées et appliquées afin d'étudier les mécanismes de dégradation (initiation, propagation, défaillance) de l'interface.

Une méthodologie a tout d'abord été établie pour caractériser l'initiation de la corrosion et les risques de couplage galvanique en accédant à la structure interne des interfaces et caractérisant leurs réactivités. Un polissage ionique en biais permet de créer un profil métal/couche intermédiaire/revêtement DLC latéralement étendu. La composition et les états chimiques de la couche intermédiaire ont été déterminés par spectroscopie Auger. Les couches réactives à base de Si, Ti and Cr, forment de nouvelles phases (carbures et oxydes). La stabilité de ces nouveaux matériaux en contact avec un sérum bovin (HyClone WTF) a été caractérisée par microcellule électrochimique. Les couches de Cr et de DLC dopé au Si présentent une bonne passivation alors que celle composée de Si se dissout. L'influence des défauts du revêtement DLC sur la réponse en courant a également été étudiée en variant la surface en contact avec l'électrolyte (de  $\text{cm}^2$  à  $\mu\text{m}^2$ ).

L'effet du confinement/crevasse et du couplage galvanique à l'interface entre l'alliage de Ti et le revêtement DLC sur la propagation de la corrosion a été étudié pour une couche intermédiaire de Si car elle est susceptible à la corrosion en milieux confinés. Dans les crevasses, des attaques de corrosion par piqûres sont détectées alors qu'en milieu confiné, le Si se dissout activement à une vitesse d'environ 3.6 nm/h à 37°C. Cette vitesse de dissolution augmente en fonction de la température avec les énergie d'activation suivantes déduites de la loi d'Arrhenius: 106 kJ/mol dans un tampon phosphate salin (PBS) et 109 kJ/mol dans l'HyClone WTF. La présence de phosphates accentue la dissolution du Si alors que les chlorures n'ont que peu d'influence.

Finalement, la défaillance liée à la corrosion de l'interface en présence de contraintes appliquées entre le DLC et un substrat CoCrMo a été étudié. Des essais tribologiques (mouvement réciproque) ont été effectués pour déterminer le nombre de cycles nécessaires à la délamination d'un

revêtement exposé à une pression critique dans le PBS à 37°C. Les résultats obtenus suivent une courbe de Wöhler. De faibles contaminations d'O<sub>2</sub>, entre 0.5 et 1.0 %, à l'interface affectent la tenue à la corrosion en fatigue, réduisant la limite d'endurance. L'extrapolation des courbes de Wöhler obtenues a démontré une bonne concordance avec les résultats des essais à long terme dans un simulateur de disque intervertébral.

## Mots-clés

Revêtement DLC, interface, couche intermédiaire, silicium, corrosion par crevasse, fatigue par la corrosion, électrochimie, technique de micro-capillaire, analyse de surface.

# Contents

|  |             |
|--|-------------|
| <b>Acknowledgements.....</b>   | <b>v</b>    |
| <b>Abstract .....</b>  | <b>vi</b>   |
| <b>Keywords.....</b>   | <b>vii</b>  |
| <b>Résumé.....</b>   | <b>viii</b> |
| <b>Mots-clés .....</b>   | <b>ix</b>   |
| <b>List of Figures .....</b>   | <b>13</b>   |
| <b>List of Tables .....</b>  | <b>17</b>   |
| <b>Abbreviations &amp; Nomenclature .....</b>  | <b>18</b>   |
| <b>Chapter 1 Introduction.....</b>   | <b>21</b>   |
| 1.1 Motivation.....  | 21          |
| 1.2 Literature Review .....  | 21          |
| 1.2.1 DLC Coatings .....   | 21          |
| 1.2.2 DLC as a coating in joint replacements.....  | 22          |
| 1.2.3 Failure cases of DLC coated articulating implants.....   | 23          |
| 1.2.4 Mechanical and chemical stability of interlayers/interfaces .....                              | 24          |
| 1.2.5 Factors influencing corrosion of coating/substrate systems .....                               | 25          |
| 1.3 Thesis objective .....   | 33          |
| <b>Chapter 2 Chemical composition and reactivity characterization of deposited interlayers .....</b> | <b>35</b>   |
| 2.1 Chapter overview .....   | 36          |
| 2.2 Experimental .....   | 37          |
| 2.2.1 Materials and coating deposition .....   | 37          |
| 2.2.2 Ion beam angled polishing (wedge-milling) .....  | 38          |
| 2.2.3 Auger electron spectroscopy (AES) analysis of the interlayer/interfaces...                     | 39          |



|                  |  |           |
|------------------|--|-----------|
| 2.2.4            | Macro and local microcapillary electrochemical characterization .....                    | 40        |
| 2.3              | Results and Discussion .....   | 43        |
| 2.3.1            | Electrochemical characterization of DLC surfaces on interlayers .....                    | 43        |
| 2.3.2            | Composition characterization of the interlayer and interfaces by AES .....               | 45        |
| 2.3.3            | Interlayer electrochemical reactivity investigated by potentiodynamic polarization ..... | 50        |
| 2.3.4            | Long-term interlayer stability assessment at OCP .....                                   | 53        |
| 2.4              | Chapter conclusions .....  | 56        |
| <b>Chapter 3</b> | <b>Corrosion of silicon in confined and crevice environments .....</b>                   | <b>59</b> |
| 3.1              | Chapter overview .....   | 60        |
| 3.2              | Chapter specific introduction.....   | 60        |
| 3.2.1            | Si stability in physiological environments .....   | 60        |
| 3.2.2            | Electrochemistry of semiconductors.....  | 62        |
| 3.3              | Experimental .....   | 65        |
| 3.3.1            | Samples and solutions .....  | 65        |
| 3.3.2            | Immersion experiments.....   | 65        |
| 3.3.3            | Electrochemical Experiments .....  | 65        |
| 3.3.4            | Post immersion characterization.....   | 68        |
| 3.4              | Results and Discussion .....   | 68        |
| 3.4.1            | Long-term immersion experiments in physiological simulating conditions                   | 68        |
| 3.4.2            | Accelerated immersion experiments in confined/crevice conditions .....                   | 71        |
| 3.4.3            | Influence of phosphorous species .....   | 72        |
| 3.4.4            | Electrochemical characterization of Si passive film stability.....                       | 74        |
| 3.4.5            | Open circuit potential (OCP) measurements .....  | 78        |
| 3.4.6            | Influence of Si wafer doping and resistivity on corrosion .....                          | 80        |
| 3.4.7            | pH determination in the confined cell and surface characterization .....                 | 81        |
| 3.4.8            | Discussion of the corrosion mechanism .....  | 85        |
| 3.4.9            | Si corrosion in the TiAlV/Si/DLC system with static stress .....                         | 87        |
| 3.5              | Chapter conclusions .....  | 88        |
| <b>Chapter 4</b> | <b>Influence of stress and fatigue on interface corrosion susceptibility.....</b>        | <b>91</b> |

|                         |  |            |
|-------------------------|--|------------|
| 4.1                     | Chapter overview .....   | 92         |
| 4.2                     | Experimental .....   | 92         |
| 4.2.1                   | Materials and methods.....   | 92         |
| 4.3                     | Results and Discussion .....   | 94         |
| 4.3.1                   | Influence of the electrolyte .....                                   | 94         |
| 4.3.2                   | Influence of fatigue.....  | 95         |
| 4.3.3                   | Influence of static stress .....                                     | 99         |
| 4.4                     | Chapter conclusions .....  | 100        |
| <b>Chapter 5</b>        | <b>Discussion summary, overall conclusions and future work .....</b> | <b>101</b> |
| 5.1                     | Discussion summary and overall conclusions .....                     | 102        |
| 5.2                     | Future work .....  | 104        |
| <b>References</b>       | <b>.....</b>   | <b>107</b> |
| <b>Curriculum Vitae</b> | <b>.....</b>   | <b>117</b> |

## List of Figures

|   |    |
|---|----|
| Fig. 1.1: (left) Retrieved DLC coated femoral head; numerous pits can be observed revealing the metallic substrate [29]. (right) Retrieved DLC coated toe joint, some remaining DLC coating can be seen on the convex component [30]. .....   | 24 |
| Fig. 1.2: Aggravating factors influencing corrosion of a coating/substrate interface. ....  | 26 |
| Fig. 1.3: Schematic of a crevice corrosion mechanism on a metal (M). ....   | 27 |
| Fig. 1.4: Diagram illustrating the typical stages of stress corrosion cracking (SCC). ....  | 29 |
| Fig. 1.5: Influence of corrosive environment on the fatigue fracture of a material.....   | 32 |
| Fig. 2.1: PACVD chamber used for DLC deposition. A schematic of the chamber interior is shown on the right.....   | 38 |
| Fig. 2.2: Schematic of Ar <sup>+</sup> beam polishing at an angle of a DLC coated substrate with an interlayer. A wedge-like profile is milled into the sample exposing the underlying materials. ....  | 39 |
| Fig. 2.3: Three-electrode macro-electrochemical cell consisting of: a platinum counter electrode (Pt CE), a 3 M silver/silver chloride reference electrode (RE <sub>Ag/AgCl</sub> ) with a Luggin capillary, and an exposed working electrode (WE) area of diameter 0.5 cm. ....  | 41 |
| Fig. 2.4: (left) Schematic of the use of the microcapillary technique for local electrochemical characterizations. In this case, the exposed area (working electrode, WE) is a wedge-milled Ti/interlayer/DLC area. (right) photograph of the microcapillary mounted in an optical microscope.....                                      | 42 |
| Fig. 2.5: Electrochemical potentiodynamic polarization curves of DLC coated samples performed with macroscale cell (0.2 cm <sup>2</sup> working area), solid lines, and microcapillary (3.85E-5 cm <sup>2</sup> working area) dashed lines. Electrolyte used was HyClone <sup>®</sup> WTF at room temperature. ....                     | 43 |
| Fig. 2.6: SEM image of wedge-milled Ti/Si/DLC sample after local electrochemical characterization with the microcapillary. Si interlayer has been laterally exposed and its corresponding interfaces with Ti and DLC. ....  | 46 |
| Fig. 2.7: AES spectra used to fit the at% composition curves for the wedge milled Ti/Si/DLC sample of Fig. 7a. a) Stack plot of C(KLL) spectra, b) C(KLL) spectra measured in DLC and Ti/Si interface, c) Si(LMM) spectra measured in Si interlayer and Si/DLC interface, d) Ti(LMM) measured in Ti substrate and Ti/Si interface. .... | 46 |
| Fig. 2.8: AES at% composition curves of wedge-milled samples: a) Ti/Si/DLC, b) Ti/Cr/DLC, c) Ti/Co/DLC and d) Ti/Si-DLC/DLC. Carbodic forms have been assigned by comparison to published reference spectra.....  | 49 |
| Fig. 2.9: AES of normalized C(KLL) spectra at a Cr/DLC interface compared to the spectra at a Ti/Si interface (peak assigned to TiC), the shoulder at 275 eV is characteristic of Cr-C. The peaks have been slightly offset for comparison purposes. ....   | 49 |
| Fig. 2.10: Local electrochemical potentiodynamic polarization measurements conducted with microcapillary filled with HyClone WTF as electrolyte, on wedge-milled samples: a) Ti/Co/DLC, b)  |    |

|   |    |
|---|----|
| Ti/Cr/DLC, c) Ti/Si/DLC, d) Ti/Si-DLC/DLC. Corresponding interlayer magnetron sputter targets were also characterized to show differences in behavior of bulk material. ....  | 51 |
| Fig. 2.11: Local open circuit potential (OCP) evolution measurements conducted with microcapillary filled with HyClone® WTF as electrolyte, on: a) Si-DLC, Cr-C and Si interlayers, and Ti substrate. b) Comparison of the OCP evolution of bulk Si (on left y-axis) and Si interlayer (on right y-axis). ....  | 54 |
| Fig. 2.12: a) SEM image of newly wedge-milled Ti/Si/DLC sample before immersion in HyClone® WTF, and, b) SEM image of the same sample after immersion in HyClone® WTF for 1.5 years, showing retracted (corroded) Si interlayer and adjacent DLC delamination front. ....   | 55 |
| Fig. 3.1: FIB cross-section of explanted DLC coated Ti6Al4V femoral head. Si interlayer has dissolved away. ....  | 61 |
| Fig. 3.2: Pourbaix diagram for the silicon-water system, at 25 °C [102]. ....   | 62 |
| Fig. 3.3: Influence of an applied potential (E) on the band bending behavior of a p-type semiconductor at an electrolyte interface: a) $E=E_{fb}$ , b) $E<E_{fb}$ , c) $E>E_{fb}$ [115]. ....   | 63 |
| Fig. 3.4: Schematic description of the confinement cell setup (referred as confined/crevice setup in the paper): (a) used for conducting electrochemical measurements, (b) modified cell used to determine pH evolution inside a confinement: agar is infiltrated with phenolphthalein (turns pink at pH 8.5-10), or thymolphthalein (turns blue above pH 10) pH indicator, and imbedded in the top clamp. ....   | 67 |
| Fig. 3.5: Reference test of the confined/crevice cell from Fig. 3.2a; using 13Cr-steel as the WE and 1 M NaCl solution at room temperature as the electrolyte, the OCP evolution is recorded. b) Severe corrosion of the 13Cr-steel WE can be seen after the experiment. ....   | 68 |
| Fig. 3.6: (a) Schematic description (exaggerated for clarification) of the corrosion processes occurring in a Si Si confined/crevice configuration showing the initial immersion situation, and the resulting situation after 35 days; at the crevice mouth (indicated by "0") a uniformly corroded area occurs to the right in the confinement ("+" arrow), while pits are found to the left inside the crevice ("- " arrow). (b) Resulting SEM image of the bottom Si wafer close to the vicinity of the crevice mouth; unclamped after 35 days in a HyClone® WTF containing crevice at 37°C. Pyramidal pits are present in the crevice area, and a distinct step occurs at the crevice mouth where the smaller opposing Si was clamped. .... | 70 |
| Fig. 3.7: A profilometer topography scan corresponding to Fig. 3.2b shows a significant corroded depth with a maximum of ca. 3 µm at the mouth (indicated at 0 mm) of the Si Si confined/crevice area, after 35 days immersion in HyClone® at 37°C. ....  | 70 |
| Fig. 3.8: Arrhenius plot demonstrating a linear active Si dissolution mechanism in 0.01 M PBS and HyClone® WTF measured in the confined area. ....  | 72 |
| Fig. 3.9: Corrosion rates of Si at the confined area when immersed in NaCl and phosphate-containing crevices ( $K_2HPO_4$ , $Na_2HPO_4$ , PBS) at 90°C for 2 h. For NaCl solutions, pH was initially adjusted by NaOH addition. ....  | 74 |
| Fig. 3.10: Anodic polarization measurements of Si at different temperatures in bulk solutions: 0.01 M NaCl (pH 5), 0.01 M PBS (pH 7.4), HyClone® WTF (pH 7.4-7.7), and NaOH (pH 13). ....   | 75 |

|  |    |
|--|----|
| Fig. 3.11: Potentiostatic polarization measurements of Si in bulk NaOH, pH 13. Influence of applied potential on the passivation behavior. ....  | 76 |
| Fig. 3.12: Nyquist plots of EIS measurements performed around the active-pseudo passive potential domain on a Si surface (exposed area 78 mm <sup>2</sup> ) immersed in NaOH (pH 13).....  | 78 |
| Fig. 3.13: Open circuit potential (OCP) measurements of Si over 48 h in bulk solution and in the confined/crevice cell configuration: (a) 0.01 M PBS at 50°C, (b) 0.01 M PBS at 70°C, (c) HyClone® WTF at 37°C and (d) HyClone WTF at 50°C. ....   | 79 |
| Fig. 3.14: Optical images of Si surfaces after immersion in confined/crevice cells at E <sub>corr</sub> in: (a) 0.01 M PBS at 50°C for 48 h, then at 70°C for 48 h, and (b) HyClone® WTF at 37°C for 48 h, then at 50°C for 48 h. ....   | 80 |
| Fig. 3.15: Si after immersion in HyClone® WTF (pH 7.4-7.7) for 10 days at 50°C, using the confined configuration from Fig. 3.1b. Area close to the confinement mouth is shown. (b) Agar infiltrated with phenolphthalein turned pink, indicating a pH above 8.5 occurred. ....   | 82 |
| Fig. 3.16: Si2p XPS spectrum from a point measured on an as received Si wafer. The SiO <sub>2</sub> and Si contributions are fitted and the area of intensity (I) beneath the fittings is determined, corresponding to a native SiO <sub>2</sub> with a thickness of ca. 1 nm. ....  | 82 |
| Fig. 3.17: XPS depth profile through a heavily corroded area on Si, after immersion in a confined cell containing HyClone® WTF at 50 °C for 10 days. At a sputter rate of 6.9 nm/min, an oxy-hydroxide layer over 400 nm in thickness is present. ....   | 83 |
| Fig. 3.18: Nyquist plot of EIS measurements performed on Si (exposed area of 78 mm <sup>2</sup> ) in HyClone® WTF at 50°C over 24 h at the OCP. ....   | 84 |
| Fig. 3.19: Schematic description of reaction mechanisms showing the influence of a confined/crevice geometry on the dissolution of Si in physiological solutions: a) initial chemistry at the beginning of the immersion experiment, b) corrosion mechanisms in the confined/crevice areas at longer immersion times, the areas of interest are enlarged for clarification.....  | 85 |
| Fig. 3.20: Average delamination radius around a Rockwell indent performed in a TiAlV/Si/DLC explant and immersion in PBS, then HyClone® WTF, at 37°C. The delamination front is averaged as a circle with radius R <sub>a</sub> , and the edge of the Rockwell indent is at radius R <sub>0</sub> (Reprinted from Acta Biomaterialia [104], with permission from Elsevier). .... | 87 |
| Fig. 4.1: (left) High frequency reciprocating sliding apparatus (HFRR, PCS Instruments) used for applying fatigue load over samples. (right) Enlarged schematic of the reciprocating pair; an alumina counter sphere slides over the DLC coated sample leaving a wear track. ....  | 93 |
| Fig. 4.2: Influence of various electrolytes on the delamination behavior of a CoCrMo/Si-DLC(1.0%O <sub>2</sub> )/DLC sample at 37 C. Optical microscope images after 13,500 reciprocating sliding cycles over a pre-scratch under a normal load of 5 N at 15 Hz. ....  | 95 |
| Fig. 4.3: Experimental methodology used to create the Wöhler curve. The load is increased by increments of 0.5 N, grey squares, until delamination occurs at the critical load (L <sub>c</sub> ), red dots. ....   | 96 |
| Fig. 4.4: Wöhler-like curves for CoCrMo/Si-DLC(x%O <sub>2</sub> )/DLC system. The critical load required for coating delamination to occur is recorded vs. the cycles to delamination. Filled-squares represent  |    |

---

|  |     |
|--|-----|
| experimental data and dotted lines are the fittings. Empty-squares correspond to long-term experiments from a spinal disk simulator.....   | 97  |
| Fig. 4.5: SEM image of a CoCrMo/Si-DLC(1.0%O <sub>2</sub> )/DLC cross-section performed in the vicinity of a delamination area, after 13,500 loading cycles under 4 N load in PBS at 37 °C. a) Overview with 8 µm long crack at interface. b) Close up of a shear band initiating from interface through interlayer and into DLC. Plastic deformation of the Si-DLC interlayer is also seen. c) Discontinuous cracks within the shear band. .... | 98  |
| Fig. 4.6: Evolution of a Rockwell indentation placed in: a) CoCrMo/Si-DLC(0.5%O <sub>2</sub> )/DLC and b) CoCrMo/Si-DLC(2.0%O <sub>2</sub> )/DLC and immersed in 0.01 M PBS at 37°C. ....  | 99  |
| Fig. 4.7: Evolution of a Rockwell indentation placed in: a) TiAlNb/Si-DLC(0.5%O <sub>2</sub> )/DLC and b) TiAlNb/Si-DLC(2.0%O <sub>2</sub> )/DLC and immersed in 0.01 M PBS at 37°C.....   | 100 |
| Fig. 5.1: Still frame from a video clip of a FEA on a defective interface. Compressive and tensile stresses are present around the deboning interface when a sliding load is applied on the coated surface ( <i>Performed by Christian Affolter, Empa</i> ). ....  | 106 |

# List of Tables

Table 3.1: Corrosion rates of Si|Si confined/crevices in different solutions at 90°C. (–) refers to no corrosion detected.....73

Table 3.2: Influence of Si wafer resistivity on uniform corrosion rate measured at the confined/crevice border. ....81

Table 4.1: Fitted parameters from the Wöhler curves corresponding to Equation 4-1.....97

## Abbreviations & Nomenclature

|                    |  |
|--------------------|--|
| DLC                | Diamond-like carbon  |
| PACVD              | Plasma activated chemical vapor deposition                 |
| Si-DLC             | a-C:H:Si ( <i>Si</i> -doped hydrogenated amorphous carbon) |
| TMS                | Si(CH <sub>3</sub> ) <sub>4</sub> (Tetramethylsilane)      |
| CC                 | Crevice corrosion  |
| SCC                | Stress corrosion cracking                                  |
| CF                 | Corrosion fatigue  |
| COF                | Coefficient of friction                                    |
| FEA                | Finite-element-analysis                                    |
| PBS                | Phosphate buffered saline                                  |
| WTF                | Wear test fluid  |
| AES                | Auger electron spectroscopy                                |
| RE                 | Reference electrode  |
| WE                 | Working electrode  |
| CE                 | Counter electrode  |
| OCP                | Open circuit potential                                     |
| KE                 | Kinetic energy   |
| LLSF               | Linear least square fitting                                |
| K <sub>IC</sub>    | Critical stress intensity                                  |
| G <sub>c</sub>     | Critical strain energy release rate                        |
| E <sub>corr</sub>  | Corrosion potential  |
| i <sub>corr</sub>  | Corrosion current density                                  |
| Δh <sub>corr</sub> | Average maximum uniform dissolution height                 |
| E <sub>a</sub>     | Activation energy  |



$Z''$  Imaginary impedance component

$Z'$  Real impedance component

$L_c$  Critical load

$L_e$  Endurance limit



# Chapter 1 Introduction

## 1.1 Motivation

The motivation behind this research initiated with investigations of failed Diamond-like Carbon (DLC) coated articulating biomedical implants. In the last decades, several series of DLC coated implants which initially showed good in-vitro testing results had to be retrieved after only a few years of implantation in patients. The implants showed severe coating delamination, which caused abrasion of the implant by DLC particles, and ultimately led to their failure.

When applying a hard coating onto a substrate, a new material is formed between the coating and the substrate, a reaction product of the coating and substrate composed of a few atomic rows. This reactively formed interface is responsible for adhering the coating onto the substrate. Often times adhesion-promoting interlayers are used, which depending on the deposition conditions, can themselves be a new material, and will form a bond at the coating/interlayer as well at the interlayer/substrate interface. These buried interlayers and interfaces of new material will usually contain different and unknown corrosion and mechanical properties that must be investigated.

Many studies have focused on assessing the mechanical adhesion of hard coatings on substrates, but few have looked at how surrounding corrosive environments can influence the coating/substrate interface stability. When applying a coating, it is particularly important to consider corrosion mechanisms that may be occurring at the interlayer or interface. Therefore, the target of this thesis is to investigate the local corrosion mechanisms affecting the substrate/DLC interface in body-like media. New and existing methodologies will be developed and utilized in order to investigate corrosion initiation and propagation by the influence of confined geometries and stress on the interface/interlayer stability. The new results presented will consistently be compared and correlated with previous work on the failed implant cases. This knowledge can improve interface/interlayer design and engineering, and provide better lifetime assessments of coated systems in corrosive media.

## 1.2 Literature Review

### 1.2.1 DLC Coatings

Hard coatings such as metal nitrides, metal carbides and diamond-like carbon (DLC), can significantly reduce surface wear and increase the lifetime of articulating components, spanning from tooling to biomedical implant applications [1]. For example, titanium nitride (TiN) coated tools can withstand numerous drilling and cutting cycles without any significant wear [2]. DLC has been extensively used

to reduce abrasion in car engine parts, which can sustain more than  $10^9$  high force loading cycles without any relevant wear [3–5]. Although the findings presented in this thesis are relevant to any hard-coated system, DLC will be used as the test material.

DLC is a class of amorphous carbon (a-C:H) that exhibits many of the desirable properties of diamond such as, low friction, high hardness, and resistance to wear [6]. It is comprised of alternating  $sp^2$  and  $sp^3$  bonds and is not crystalline but rather amorphous. Having no long-range order means there are no fracture planes along which to break. DLC films are commonly produced by plasma activated chemical vapor deposition (PACVD) using acetylene ( $C_2H_2$ ) as the precursor gas [7]. DLC films exhibit very high amounts of intrinsic residual stress (up to ca. 10 GPa) and are hence not deposited in thicknesses over 4  $\mu m$  [7]. The high residual stress also makes it more difficult to bond the DLC coating onto the substrate, to combat this, adhesion promoting interlayers, such as silicon (Si), Si-doped hydrogenated amorphous carbon (a-C:H:Si, denoted *Si-DLC* throughout the text), and chromium (Cr), are often used to mitigate stresses at the DLC/substrate interface [8]. If the substrate material has a high tendency to bond with carbon such as titanium (Ti), Cr, and iron (Fe), a carbide of a few atomic rows is formed at the interface, which can sometimes also effectively bond the DLC onto the substrate.

### 1.2.2 DLC as a coating in joint replacements

Total joint replacement (TJR) surgery is one of the most frequently performed elective procedures in the United States and the UK [9,10]. The number of hip and knee replacements has continuously risen over the past decades, while the ages of the patients has significantly decreased [9]. Metal-on-polymer (MoP) bearings are of the most commonly implanted, followed by ceramic-on-polymer (CoP). Metal-on-metal (MoM) hip implants made up only 0.6% of the total number of hip replacements performed in the UK in 2017 [10]. The average lifespan of a hip implant is currently 15 years [11,12], in younger patients this is problematic, and the probability the implant needs to be revised increases, there is hence a growing need for longer lasting implants. The most common reason for a revision is aseptic loosening (bondage failure between implant and bone) caused by inadequate initial fixation, loss of mechanical fixation over time, or biological loss of fixation induced by implant wear debris [13]. In MoP and CoP pairings, wear of the polymer counterpart remains an issue. While MoM pairings have lower wear rates, the release of even small amounts of metal ions in the human body can cause severe medical complications such as pseudotumours and metal poisoning [14]. Considerable efforts have hence been placed on reducing the wear or articulating implants by coating the metal component (most commonly a Ti-based, or CoCrMo, alloy) with a hard biocompatible coating such as DLC.

In-vivo and in-vitro experiments have demonstrated that DLC is biocompatible and does not trigger adverse effects on attached body cells [15,16]. Numerous body cell types have been successfully grown on DLC surfaces, including fibroblasts, macrophages and other body tissues [17]. As well DLC surfaces have excellent haemocompatibility (compatible with blood), and have successfully been applied to cardiovascular-based implants such as stents and prosthetic heart valves [16]. Various

authors have studied the tribological performance of DLC as an implant material in various body-like media. Pin-on-disc testing is one of the most common methods used for early stage testing of articulating biomaterials, and has been extensively utilized to analyze the wear behavior of DLC against ultra-high-molecular-weight polyethylene (UHMWPE) [11,18–22]. DLC coated disks of various medical alloys (CoCrMo, AISI316L, TiAlV) improved the wear resistance of UHMWPE pins up to 30 – 600 times up to 7 million loading cycles in 1% NaCl solution [19]. Similarly a wear volume reduction of 2 orders in magnitude was observed for DLC coated pins articulating against stainless steel disks in bovine serum [20]. On the contrary, CoCrMo/DLC disks showed no significant reduction in UHMWPE pin wear, and an increased coefficient of friction (CoF) in simulated body fluid (SBF) [18]. Although pin-on-disk studies generally indicate improved tribological properties, the results mainly focus on the improved wear behavior of the polymer part, and do not thoroughly comment on the influence of the corrosive environment on the substrate/DLC counterpart. Further there is significant variance in the materials and testing conditions, with applied loads varying from 10 – 617 N, and the number of reciprocating cycles from 3600 – 1 million [11]. Mutli-directional, ball-in-socket hip joint simulators can provide more accurate conditions experienced by articulating implants and have more standardized testing procedures [11]. Generally studies indicate that MoM articulating counterparts show reduced wear when one or both of the surfaces is coated with DLC (or another hard coating) [11,23–25]. In NaCl solution wear reduction is significant, by a factor of  $10^5$ – $10^6$  [23], and less so in diluted bovine serum [24,25]. DLC coated balls against UHMWPE sockets also show improvements in wear in distilled water [26] and in diluted bovine serum [11,27,28]. Despite the general optimistic studies, the relatively short-term in vitro results were not an accurate depiction of how the substrate/DLC system would behave long-term in the body [11], and many DLC coated artificial joints failed in the body after only a few years of implantation [29]. The few follow-up investigations of these failure cases are described in the following section.

### 1.2.3 Failure cases of DLC coated articulating implants

Between 1993 – 95 a study was carried out in which 101 total hip arthroplasty procedures were performed with DLC coated titanium alloy (Ti6Al4V) femoral heads, containing a Si adhesion promoting interlayer, and polyethylene (PE) articulating counter cups [29]. After an average implantation time of 9 years, approximately half of the implants had to be revised. The retrieved femoral heads were severely worn and contained several spots where the coating (2-3  $\mu\text{m}$  in thickness) had locally delaminated, as seen Fig. 1.1 (left). The delaminated DLC particles caused severe abrasion of the PE counter cup, which lead to an inflammatory response and resulted in aseptic loosening of the implant [29]. Similarly, a MoM CoCrMo toe joint with both surface coated with DLC, and a Si interlayer, was retrieved after only 4 years in the body, the retrieved implant showed several points of coating delamination mainly near scratches, as shown in Fig. 1.1 (right) [30,31].



*Fig. 1.1: (left) Retrieved DLC coated femoral head; numerous pits can be observed revealing the metallic substrate [29]. (right) Retrieved DLC coated toe joint, some remaining DLC coating can be seen on the convex component [30].*

Another attempt to produce DLC coated joint implants was made by the Swiss company Implant Design AG in 2001. A DLC coated CoCrMo knee component, by the trademark name Diamond Rota Gliding, was recalled after the implants were retrieved from several patients after a few years of implantation. The Swiss Federal Office of Public Health banned the knee implants, and no detailed follow-up studies were performed to date.

While DLC itself has very good mechanical properties and is considered inert, miniature defects in the coating such as micro-pinholes create entry points for surrounding joint fluid to contact the interlayer/interface [32]. This was confirmed by characterizing DLC coated surfaces with XPS after exposure to various fluids [33]. The presence of Si peaks suggested that the underlying interlayer must have been exposed at defects, allowing fluid to penetrate and attack the thin silicon carbide (SiC) transition layer [33]. If the deposited interlayer or formed carbide is chemically unstable and susceptible to corrosion, the material will disintegrate, resulting in coating delamination and failure of the implant.

#### 1.2.4 Mechanical and chemical stability of interlayers/interfaces

Interlayers reduce the likelihood of coating delamination and many studies have investigated the influence of interlayers on the interfacial toughness of the system using various adhesion tests. For example, scratch tests and Rockwell indentations showed that Ti interlayers improved the adhesion of TiN coatings on substrates, due to strong Ti bonding with N atoms [34–36]. Rockwell indentations also showed that the addition of a Cr interlayer improved the interfacial toughness of DLC coated steel [37], and improved tribological properties such as low coefficient of frictions were demonstrated for CrN and CCr multi-interlayers [38]. Reciprocating wear tests on DLC coated steel demonstrated that samples with a Si interlayer provided greater resistance to delamination failure than samples with Cr interlayers [39]. Scratch tests further showed better adherence of DLC coatings

on TiAlV substrates when a 20 nm Si interlayer was used [40]. In other applications, Si interlayers have also been used to improve the electrical properties at the germanium/silicon dioxide interface of photonic devices [41,42]. However, in the presence of a corrosive environment (such as human synovial fluid), the strong mechanical integrity of these coated systems can be adversely affected. Although the hard coatings themselves are relatively inert, the corrosive media can penetrate through local coating defects and attack the underlying material. For example the interfacial adhesion strength of Si-doped DLC coatings on stainless steel was reduced up to 75% when the samples were immersed in fetal calf serum and artificial saliva [43]. Pits were observed at a TiN/stainless steel interface at locations where NaCl solution penetrated through columnar grain boundaries within the coating [44].

Based on these observations, some studies have also focused on the chemical stability investigation of hard-coated surfaces. Macroscale (consisting of a characterization area in the cm<sup>2</sup> range) electrochemical characterization methods such as potentiodynamic polarization and electrochemical impedance spectroscopy (EIS) have been widely used to provide fast information about the corrosion susceptibility of coated metallic substrates. For dental applications, EIS was used to study the corrosion behavior in saline solution of DLC coatings on Ti-based substrates, with Ti and Cr interlayers [45]. The coated samples that included a Cr interlayer showed the highest resistance to charge transfer. Potentiodynamic polarization measurements were performed on 316L steel/DLC systems with various SiN<sub>x</sub> interlayers and the corrosion protection behavior of the substrate increased with each deposited film [46]. Long-term immersion of 304L/TiN samples in H<sub>2</sub>SO<sub>4</sub> showed increasing open circuit potential (OCP) over time, due to the high tendency of 304L to passivate at coating defects. However when a weaker passivating substrate such as Fe was used, the OCP of the Fe/TiN sample rapidly decreased to the same potential as that of bare Fe [47].

As the macroscale electrochemical behavior is highly correlated with a convolution of the extent of coating defects, passivity of the underlying material, and the size of the exposed electrode area, determination of the coating porosity is essential in order to compare the corrosion resistance of different coated systems [48,49]. However, this information is often excluded in many corrosion studies, and hence comparison between different deposition batches and interlayers becomes restricted. Macroscale characterization on the coating surface is also not suitable to assess the corrosion mechanisms and stability of the actual buried interlayer/interface itself. The deposited interlayer will act as a new material with corrosion susceptibility characteristics different from that of the bulk material analog. Especially when the interlayer is a blend of more than one material, for example Si-DLC, or chromium carbide (Cr-C), that may also contain some contaminations (e.g. oxygen, carbon) from the deposition processes.

### 1.2.5 Factors influencing corrosion of coating/substrate systems

If corrosive media penetrates the coating at a local defect, several aggravating factors can adversely affect the stability of the coating/substrate interface such as crevices and confined geometries, galvanic coupling, stress, and fatigue. A schematic showing how each of these aggravating factors

can influence the stability of the interlayer or interface at a defective site is presented in Fig. 1.2. A description of the contribution of each aggravating factor to the corrosion mechanisms is given in the following, along with common experiments/tests that can be performed in order to determine if the specific aggravating factor influences the corrosion behavior of the material of interest.

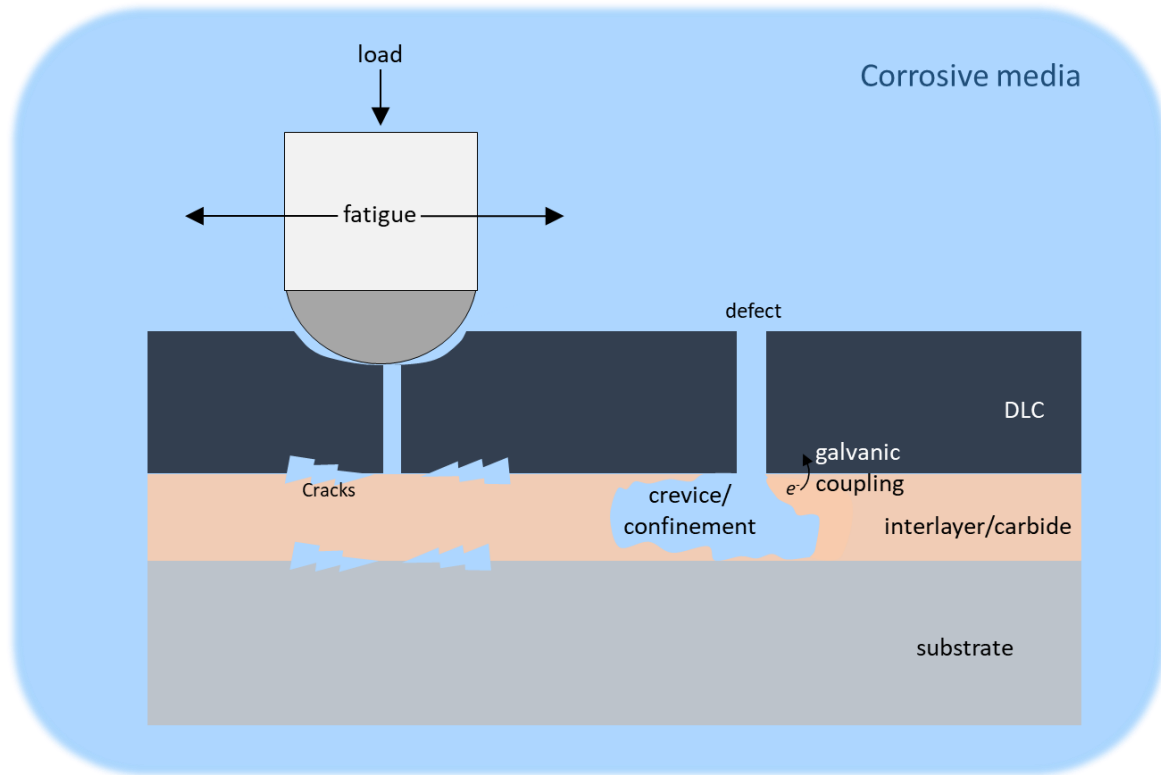


*Fig. 1.2: Aggravating factors influencing corrosion of a coating/substrate interface.*

#### 1.2.5.1 Localized corrosion - confined geometry induced corrosion

In a confined geometrical feature such as a pit, crevice, or crack, localized corrosion attack on a normally passive material may occur. The corrosion is initiated by a difference in oxygen availability between the confined and accessible areas of the metal, leading to the formation of a local anode (in the confinement), and local cathode (the surrounding passive surface), this is commonly referred to as an aeration cell [50,51]. The standard mechanism for crevice corrosion is based on iron or steel in chloride containing environments, and is outlined in the schematic of Fig. 1.3. Inside the crevice, oxygen ( $O_2$ ) is consumed relatively rapidly via the  $O_2$  reduction reaction, impairing further passivation and resulting in the accumulation of metal cations. This pulls negatively charged chloride ions ( $Cl^-$ ) into the crevice, which can couple with  $H^+$  to produce hydrochloric acid ( $HCl$ ), resulting in local acidification. As the environment in the crevice becomes more acidic, hydrogen reduction can also take place, which is a charge transfer controlled reaction and can hence increase the metal dissolution rate within the crevice. As the outside of the crevice continues to passivate, a potential difference is created and a coupling process is established between the cathodic passive area, and the anodic active area within the crevice, resulting in further corrosion inside the crevice. The



combination of all of these processes induces an ongoing autocatalytic process [50,51]. Although this mechanism is widely accepted as the crevice/pitting corrosion model occurring on metals, it is important to recall that the formulation of this mechanism is based on Fe and Fe alloys. Other materials, such as Si, may have different initiation and propagation processes, as is discussed in Chapter 3.

Confined geometries as they relate to hard-coated systems can be inherent of the component's design, but defects in the coating can themselves form small confinements. A small amount of electrolyte in the defect will have restricted access to  $O_2$  and solution exchange, and a pit may initiate at the interlayer/interface via the mechanism in Fig. 1.3. An initial pit can grow into a crevice beneath the coating, resulting in delamination [52]. The situation is often worsened due to galvanic coupling between the coating and underlying material, and these two process often occur simultaneously. For example corrosion seemed to initiate at defective sites of CrN/NbN multilayered coatings, due to a combination of crevice and galvanic coupling effects [52]. As already mentioned, a TiAlV/DLC hip implant which contained a Si interlayer failed after a few years in the body [29]. The investigations presented in Chapter 3 reveal that the cause of this failure was crevice corrosion of the Si interlayer.

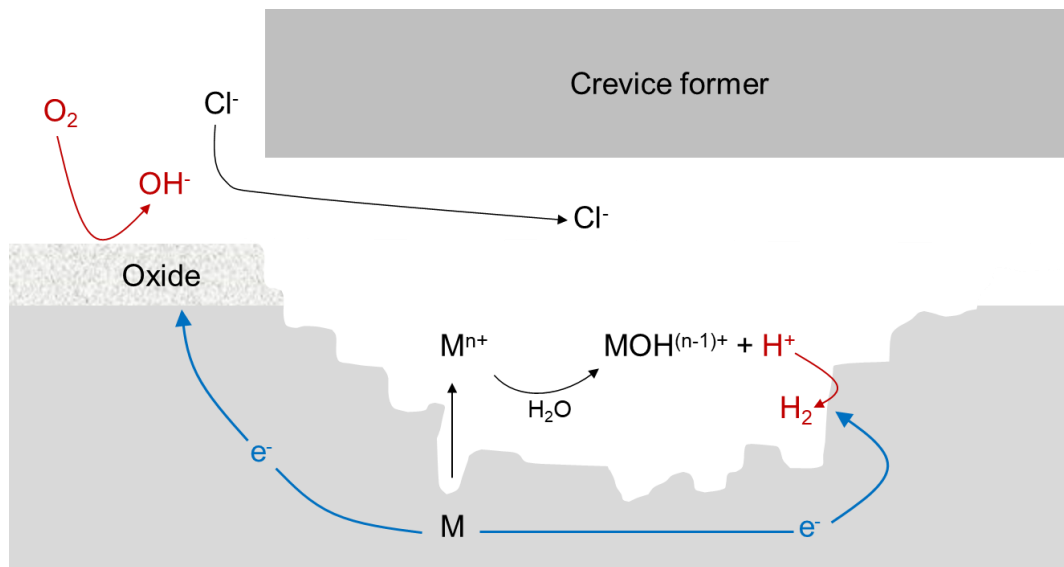


Fig. 1.3: Schematic of a crevice corrosion mechanism on a metal (M).

#### 1.2.5.1 Galvanic corrosion

When two different metals (or semi-conductive materials) are in contact and in the presence of a conductive electrolyte, galvanic corrosion can occur [53,54]. A potential difference usually exists between the two metals and the nobler (of more positive electrochemical potential) metal acts as a cathode to the more active metal (more negative electrochemical potential), which acts as an anode. In such a case, corrosion of the more active metal increases, while corrosion of the nobler

metal reduces. The further apart the electrochemical potentials of the metals are, the higher the rate of galvanic corrosion [53,54]. Determining the galvanic corrosion susceptibility of one bulk material with respect to another is relatively straight forward and is done so by comparing their corrosion potentials ( $E_{corr}$ ) in the desired electrolyte. The corrosion loss of a metal can also be determined and compared in the presence and absence of another material.

As it relates to coated systems, determining the influence of galvanic coupling at the interface is more challenging. Generally the hard coating usually makes up the noble component and the substrate, or interlayer, makes up the active component [55]. The influence of galvanic corrosion at interfaces was studied by depositing conducting TiN and ZrN coatings on insulating glass substrates in order to measure their intrinsic corrosion potentials. The measured values were higher compared to the ones obtained when the coatings were deposited on steel. In this case nearly the same negative potentials as on the bare steel were obtained, the potential shift interpreted in terms of galvanic coupling and polarization of the nitride coating surface [55,56]. Pits were observed at a TiN/stainless steel interface at locations where NaCl solution penetrated through columnar grain boundaries within the coating. Local galvanic coupling was believed to occur between the nobler TiN coating and more active substrate [44]. If the substrate material can passivate in the corresponding electrolyte, the galvanic couple becomes negligible [47]. For example, long-term immersion experiments of 304L/ TiN samples in  $H_2SO_4$  showed an increasing OCP over time, due to the high tendency of 304L to passivate at coating defects. However when a weaker passivating substrate such as Fe was used, the OCP of the Fe/TiN sample rapidly decreased to the same potential as that of bare Fe. When the small Fe anodic area (corresponding to defects) was coupled to the large cathodic area (TiN), galvanic corrosion of the Fe occurred [47]. Further, deposited interlayer materials nobler than the substrate can reduce corrosion, for example lower current densities were observed for Fe/Ti/TiN systems compared to Fe/TiN systems with no Ti interlayer [47].

### 1.2.5.2 Stress Corrosion Cracking (SCC)

When a static stress or load is applied to a material in the presence of specific environmental conditions (temperature, electrolyte), SCC may occur. There are normally three conditions that must be present in order to produce SCC; a susceptible material, a specific critical environment, and a static stress exerted on the material. For example under a certain tensile load, stainless steels can crack in the presence of hot chlorides, brass in ammonia, and titanium in methanol [50,51]. SCC susceptibility can be experimentally assessed by fracture mechanics based testing. A typical test consists of applying a constant stress on a pre-cracked sample and measuring the crack propagation rate ( $\Delta d/\Delta t$ ) in different media. By plotting the  $\Delta d/\Delta t$  against the stress intensity factor,  $K$  (magnitude of stress distribution at the crack tip) a curve such as the one in presented Fig. 1.4 can be used to determine the influence of SCC on the material of interest [57]. The curve consist of three prominent regions: crack initiation (*Stage 1*), steady state crack propagation (*Stage 2*), and final crack propagation and fracture (*Stage 3*). Stages 1 and 2 are highly dependent on the material/environment combination and the plateau is characteristic of mass transport of

environmental species into the crack tip [57,58]. Below a certain stress intensity threshold value,  $K_{ISCC}$  (dependent on the material and environment combination), a crack will not propagate. When the material's critical stress intensity value,  $K_{IC}$  (independent of the environment), is reached final fracture occurs. The closer  $K_{ISCC}$  is to  $K_{IC}$ , the less the corresponding environment influences the material [57,58].

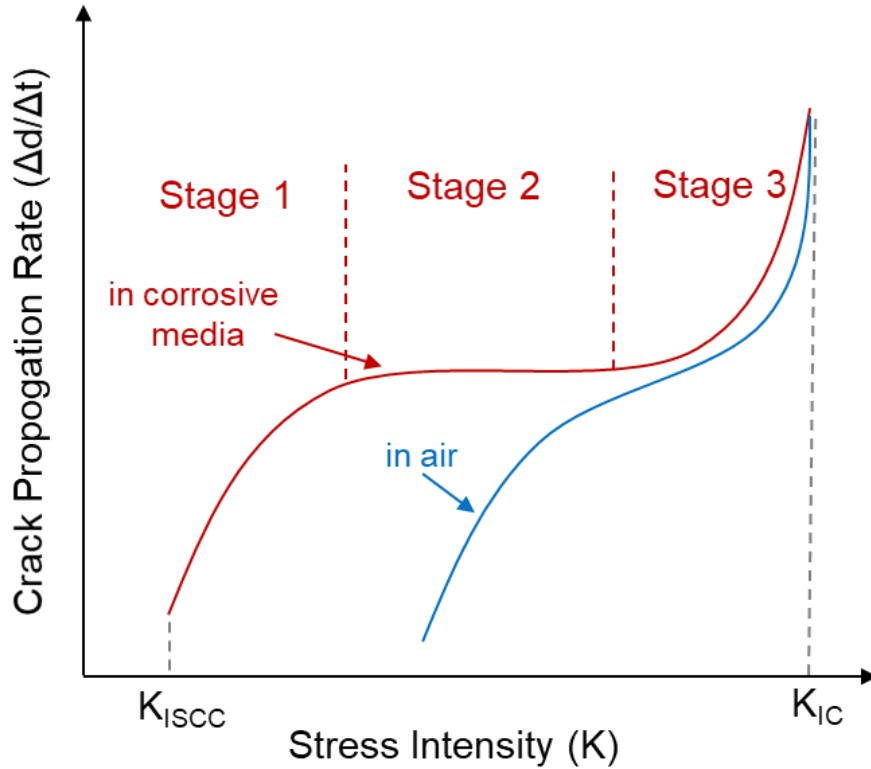


Fig. 1.4: Diagram illustrating the typical stages of stress corrosion cracking (SCC).

Different mechanical techniques have been utilized to study SCC as it relates to hard coatings on substrates. For example, a four point micromechanical piezo-electric setup was utilized to quantitatively measure the fracture resistance of  $\text{SiO}_2/\text{TiN}$  interfaces in microelectronic interconnect structures [59]. It was concluded that the interface showed to be susceptible to environmentally assisted debonding, similar to a SCC mechanism [59,60]. The stress can come from an external source (such as a bending device), but the internal residual stress of the coating itself can cause crack propagation along the interface [61]. The influence of residual stress on the interfacial toughness of DLC coatings on various metallic substrates (Ti, Al, stainless steels) was investigated by [61]. By depositing coatings of different thicknesses, they determined the critical strain energy release rate ( $G_c$ ), analogous to  $K_{IC}$ , needed for debonding to occur when the sample cooled to room temperature after deposition [61,62]. Similarly, the  $G_c$  of hard coatings on different substrates has been determined after prolonged exposure in air [63]. A Rockwell indentation method developed by Drory and Hutchinson can also be utilized to determine the strain energy release rate ( $G$ ) by tracking the delamination area around the indent [64]. A Rockwell indent causes plastic deformation of the substrate, exerting a tensile stress on the interface (in addition to the

intrinsic stress generated by the coating), as was previously shown by finite-element-analysis (FEA) [65]. While many studies have utilized these techniques to determine the interfacial toughness in air, the influence of different media (eg. acids, chloride-rich, body-like fluids) on the interfacial stability of hard coated samples has seldom been investigated. In previous work, Falub et al. studied the influence of stress on DLC coated CoCrMo alloys by performing Rockwell indentions on samples and tracking the delamination area around the indentation [66,67]. The samples initially showed good adhesion in air, however the rate of delamination significantly increased when the samples were immersed in phosphate-buffered saline (PBS). TEM micrographs near the delaminated area revealed a crack through the center of the carbidic interface layer [67,68]. By determining the average speed of delamination from the edge of the indentation and plotting it against the  $G$ , it was shown that the delamination followed a SCC mechanism (with a threshold  $G$  and *Stage 1* crack propagation behavior) [66,67]. Similarly, TEM analysis performed on DLC coated aluminum interfaces revealed a break at the mixing layer of oxide and DLC [69]. This usually occurs when no interlayer is used or a weakly-bonded reactively formed interface is grown [65,70]. The SCC situation is significantly improved however when a good interlayer material is used. For example tantalum (Ta) behaves as a very good interlayer due to its strong carbidic form (Ta-C) [70]. A 90 nm Si-DLC interlayer between DLC and CoCrMo also improved the  $G_c$  eight times [66]. Small contaminations at the Si-DLC/CoCrMo interface can however adversely affect this interface when a static stress is applied, this is further discussed in Chapter 4.

### 1.2.5.3 Corrosion Fatigue (CF)

When a metal is exposed to a cyclic load in a corrosive environment, its fatigue strength can be significantly lowered, this is known as corrosion fatigue (CF). CF differs from SCC in that it can occur on any metal in any environment, as opposed to requiring a specific metal/environment combination [71]. Metals that would normally re-passivate under a static load become of concern, as each load cycle can induce oxide film breakdown. By visual inspection, materials suffering from CF often show the characteristic beach marks (striations) and shear bands produced by plastic deformation associated with fatigue, infused with corrosive species and corrosion products. Further, CF cracks are typically transgranular (along slip planes) as opposed to intergranular (along grain boundaries) [50,71]. For CF testing, a periodic stress, or load, is applied to the metal in a corrosive environment (gas or liquid). The stress required to cause fatigue failure after some number of cycles is noted, and expressed in a Wöhler curve (or S-N curve), the standard representation for fatigue assessment. A sample Wöhler curve is displayed in Fig. 1.5, along with one effected by CF. It displays the relationship between cyclic load amplitude and the number of loading cycles to failure. The curve allows for determination of the *fatigue limit*, defined as the highest stress below which no failure occurs, which is expressed as a plateau in the curve. Not all metals exhibit an obvious *fatigue limit*, in which case an *endurance limit* is defined as the maximum load where the material does not fail to at least  $10^8$  cycles [51]. If the system is simultaneously affected by corrosion, the cycles to failure are reduced and the *fatigue/endurance limit* eliminated, as depicted in Fig. 1.5 [51,71].

Several authors have studied the influence of different environments on the fatigue behavior of hard-coated systems, by analysis of the coefficient of friction (COF) and wear volumes. However, fewer have investigated the role of the interface material in these studies. It was calculated that the highest load at an interface occurs at sufficiently large defects, and from here delamination can initiate and propagate [72]. Further the highest shear stress acting on the interface occurs at the edge of the deposited hard coatings [73]. Cross-sections after cyclic indentation and scratch tests revealed that lateral cracks initiated at the interface of steel/DLC due to plastic/elastic mismatch between the substrate and coating [74]. The influence of simulated body fluid (SBF) and NaCl solution on the sliding wear of 316L steel/Cr/DLC was investigated [75]. Under a load of 5 N, the wear volume of the sample tested in SBF was double that of the one tested in NaCl solution and exhibited a much higher coefficient of friction. However at a load of 2 N (smaller shearing action), nearly identical COFs were observed irrespective of the solution. This indicated that the stress state to which the substrate/coating is subjected to highly influences the delamination mechanism when in contact with certain corrosive media [75]. It was also calculated that coating delamination occurs when a stress threshold value of 370 MPa is reached at the vicinity of the interface, from which nucleation and crack propagation leads to coating failure [75]. Comparison across different literature indicates that this threshold value is attained much sooner depending on the test solution and interlayer used (or interface formed) [75–81]. For example in air, wear tests on DLC films deposited on nitrided TiAlV alloys presented longer lifetimes than films deposited on the bare alloy. However when immersed in PBS, the nitride alloy/DLC system failed 10 times faster than the bare alloy/DLC, this was attributed to poor chemical stability of the nitride/DLC layer interface [80]. Similarly, ball-on-disk wear tests on TiAlV/DLC presented much higher delamination in deionized water than in ambient air of 25% relative humidity [82]. Even small contaminations of an interlayer material can have detrimental effects on the CF behavior of a coated system. For example in previous work, the performance of CoCrMo/Ta/DLC spinal disk implant pairs was assessed in an articulating ball-on-socket spinal disk simulator [83]. The DLC-on-DLC implant pair successfully passed 101 million loading cycles (corresponding to a lifetime of motion in-vivo) in HyClone® Wear Test Fluid (WTF) without any significant wear [3,83]. However when the Ta interlayer was intentionally contaminated with a small amount of O<sub>2</sub> during deposition, much earlier failure occurred in the simulator [83]. An intentionally contaminated Si-DLC interlayer showed failure after just 100 000 loading cycles, the delamination always originated from a coating defect [84]. It was concluded that the highest load acting at the interface is at the edge of a defect. The influence of small contaminations on the CF behavior of a coated system is further investigated in Chapter 4.

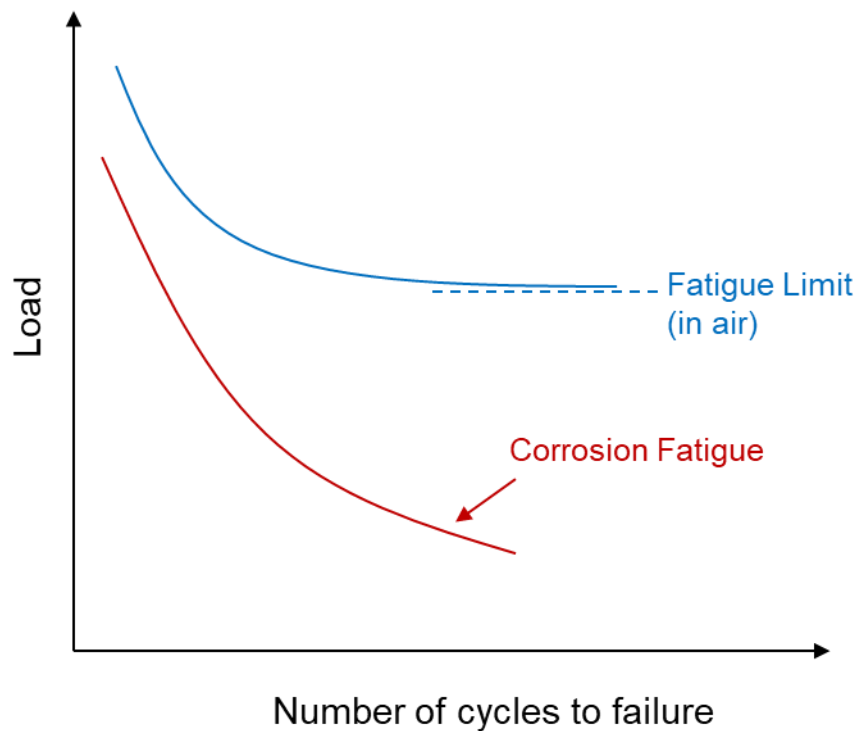


Fig. 1.5: Influence of corrosive environment on the fatigue fracture of a material

Of course, all of these corrosion processes can occur simultaneously on a material, or often times propagate from one another. A common sequence of events is as follows.

- 1) At a coating defective site, the interlayer or interface is initially protected from corrosive species by a passivating film (an oxide). Corrosion can be *initiated* if a local breakdown of this passivating film occurs.
- 2) Constricting geometries, such as pits and crevices at the interface, can support *propagation* of the corrosion attack by locally restricting diffusion of aggressive species. This is often accompanied by a pH change. Galvanic coupling of the interlayer/interface material with the substrate or coating can further accelerate the attack.
- 3) Added stress on the system, either static or cyclic, can accelerate the corrosion processes through propagating cracks (along the interface) formed at weakened confinement sites, resulting in interface fracture, delamination, and ultimate failure.

Investigations into this sequence of events occurring at the coating/substrate interface make up the objective of this thesis.

### 1.3 Thesis objective

The reported cases of early in-vivo failures of substrate/DLC implants reveals a need for a detailed analysis and understanding of the possible degradation mechanisms acting on the adhesion promoting interlayer and reactively formed interface. While the mechanical integrity of hard coated systems and their interfaces has been assessed by numerous authors, there is little research on the influence of corrosive environments on the chemical stability of the interlayer/interface material. Without a fundamental understanding of the corrosion mechanisms taking place at the interlayer and reactively formed interfaces, an accurate prediction of the implant lifetime is very difficult to achieve. Further, as implants have to survive several years in the body, testing of implants usually requires extensive long-term in-vitro experiments. While this is definitely needed, there is a growing interest in reliable accelerated methodologies for determining a coated material's lifetime in corrosive media.

The aim of this thesis is therefore to investigate corrosion *initiation*, *propagation* and *failure* at substrate/DLC interfaces. The influence some aggravating factors such as confinements, galvanic coupling, stress and fatigue, have on the chemical stability of the interlayer and interface materials have been studied. Failed DLC coated implant cases have been used as reference systems, and the environments in which they failed were simulated on replica samples. In order to achieve a mechanistic understanding, surface characterization, electrochemical and mechanical techniques were applied to investigate the following phenomena:

- Corrosion initiation (due to substrate and interlayer oxide dissolution at defective sites) of the deposited interlayer or interface in physiological-relevant media were investigated by implementing a methodology for characterizing the chemical composition and corrosion susceptibility of buried interlayers. For this, angled flat-milling and a microcapillary electrochemical technique was utilized. The influence of galvanic coupling between the coating and underlying material was addressed. As well, the influence of defects on the electrochemical behavior of macro vs. local electrochemical techniques was analyzed.
- Corrosion propagation at the interface was investigated by determining the influence of constricting geometries on the corrosion susceptibility of interfaces and interlayer materials. Particularly the influence of confinements and crevices on Si, and Si-based interlayers, in physiological simulating solutions was investigated. As there is no, to our knowledge, prior research on the crevice corrosion mechanism of Si, a thorough investigation using Si substrates was first conducted in crevices and confined geometrical environments. This gave strong insight into the failure cases of the TiAlV/Si/DLC hip joint implants.
- Final corrosion failure at the interface was investigated by determining the influence of static and cyclic load on the substrate/DLC systems in physiological relevant media. This was accomplished by developing an accelerated methodology for investigating the influence of stress and fatigue on the corrosion behavior of buried interfaces by utilizing a reciprocating

sliding instrument. Modified Wöhler-like curves were generated in order to study the relation between coating delamination and load at the interface.

Experimental results obtained with accelerated protocols and dedicated setups have been consistently compared with long-term experiments performed during this PhD work and with prior studies performed in the Empa laboratory, in order to determine whether the accelerated experiments could successfully be correlated with the long-term experiments.



## Chapter 2 Chemical composition and reactivity characterization of deposited interlayers

*The contents of this chapter are reproduced with permission from the published article [85]:*

**A methodology for characterizing the electrochemical stability of DLC coated interlayers and interfaces**

*Emilija Ilic<sup>1,2</sup>, Ainhoa Pardo<sup>1</sup>, Thomas Suter<sup>1</sup>, Stefano Mischler<sup>2</sup>, Patrik Schmutz<sup>1</sup> and Roland Hauert<sup>1</sup>*

<sup>1</sup> Empa, Swiss Federal Laboratories for Materials Science and Technology, Laboratory for Joining Technologies and Corrosion, Switzerland

<sup>2</sup> EPFL, École Polytechnique Fédérale de Lausanne, Tribology and Interfacial Chemistry Group, Switzerland

*Surface & Coatings Technology (2019)*

*Volume 375, pages 402-413*

*10.1016/j.surfcoat.2019.07.055*

*© 2019 Elsevier B.V.*

**Contributions of E.Ilic:** Performed sample preparations, coating depositions, experimental work, characterizations, and data analysis. Formulated key ideas and discussion points, and wrote the manuscript. Performed AES fitting in collaboration with R. Hauert.

## 2.1 Chapter overview

DLC coatings are often deposited on Si and Cr based interlayers to promote bonding with the substrate. While these interlayers present good adhesive properties, their chemical stability at coating defects may be adversely affected in corrosive environments, like the human body where DLC coated implants are of interest. A methodology is presented for accessing and characterizing the electrochemical reactivity of buried interlayers and interfaces. The interlayer/interface is revealed by ion beam polishing at an angle, forming a wedge-like profile of the substrate/interlayer/DLC, and characterized with a local electrochemical microcapillary technique. The chemical composition of the interlayer/interface is determined by Auger electron spectroscopy (AES) spectra recording and fitting. Assigning peak shapes to reference spectra from known components allowed for the resolution of carbidic compounds at substrate/interlayer and interlayer/DLC interfaces. Cr and Si-DLC based interlayers presented stable electrochemical behavior, while a mainly Si interlayer corroded in bovine-based wear test fluid (HyClone® WTF), analogous to a failed implant case and a long-term immersion experiment. The influence of coating defects on the current response of DLC surfaces was also investigated by varying the exposed characterization area (from the  $\mu\text{m}^2$  to the  $\text{cm}^2$  range). Microscale areas allowed for a better representation of the intrinsic reactivity of DLC, while larger areas were highly dependent on the underlying interlayer due to incorporation of coating defects.

## 2.2 Experimental

### 2.2.1 Materials and coating deposition

Titanium disk substrates (99.5 % Ti, diameter 2.5 cm, from Brüttsch-Rüeggger AG) were ground (320 grit CarbiMet SiC paper, Buehler) and polished (9  $\mu\text{m}$  MetaDi paste, 0.06  $\mu\text{m}$  Master-Met colloidal silica, Buehler) to mirror finish accordingly to the metallographic preparation standard for Ti, ultrasonically cleaned in acetone then ethanol for 15 min in each agent, and dried under argon (Ar).

A custom-built 13.56 MHz radio frequency (RF) plasma-activated chemical vapor deposition (PACVD) chamber (under a vacuum base pressure on the order of  $10^{-5}$  Pa) was used for interlayer and coating deposition, the chamber is shown in Fig. 2.1. The sample holder, the *hot* electrode, is connected to a RF power supply in order to generate a plasma from the incoming gas (Ar or  $\text{C}_2\text{H}_2$ ). The stainless steel chamber walls act as the counter electrode. The difference in mobility of ions and electrons in the high frequency plasma results in a negative bias voltage on the sample holder (and thus the sample) so that positively charged plasma ions are accelerated and deposited onto the sample surface. The upper portion of the chamber contains a magnetron that allows solid substances to be deposited onto the substrate (as interlayers for example) via a sputter target. A DC power supply and magnetic field are utilized to produce and confine Ar plasma close to the magnetron sputter target. Once the target has been pre-cleaned via Ar bombardment, the shutter just below the target is opened, allowing the sputtered target atoms to deposit onto the substrate.

Prior to deposition, the substrates were cleaned in situ for 30 min with Ar plasma with a flow rate of 19  $\text{cm}^3/\text{min}$  at -600 V self-bias. Secondly, 60 – 100 nm adhesion promoting interlayers, cobalt (Co), chromium (Cr), and silicon (Si) were grown onto the substrates via magnetron sputtering with a target using an Ar flow rate of 3  $\text{cm}^3/\text{min}$  at 60 W. A Si-doped hydrogenated amorphous carbon, a-C:H:Si (denoted *Si-DLC* throughout the thesis), interlayer was grown using tetramethylsilane (TMS),  $\text{Si}(\text{CH}_3)_4$ , gas at a flow rate of 9.6  $\text{cm}^3/\text{min}$ . Lastly a 2  $\mu\text{m}$  DLC, a-C:H, coating was deposited using acetylene ( $\text{C}_2\text{H}_2$ ) gas with a flow rate of 7.2  $\text{cm}^3/\text{min}$  at -600 V self-bias. Throughout the paper, a sample will be denoted as substrate/interlayer/coating (for example; Ti/Si/DLC).

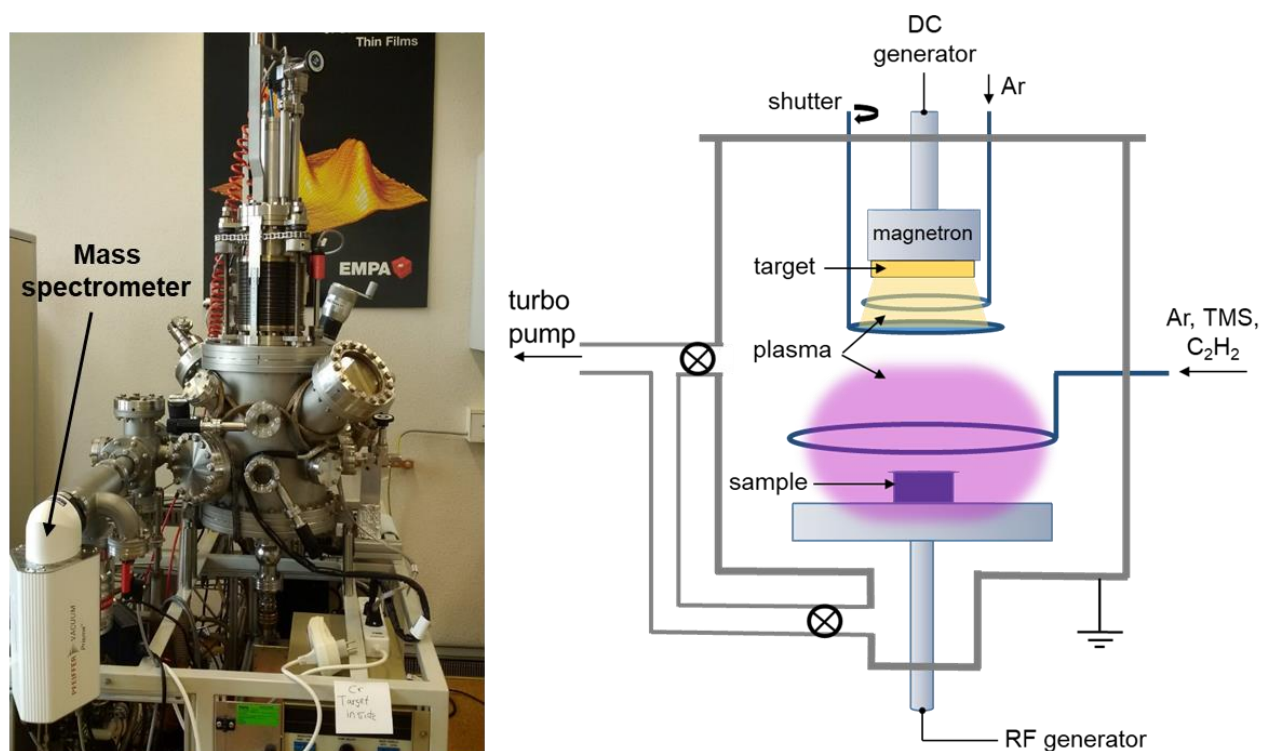


Fig. 2.1: PACVD chamber used for DLC deposition. A schematic of the chamber interior is shown on the right.

After the coated samples were prepared, a three-step methodology was applied in which the buried interlayer was revealed and characterized by:

- 1) Ion beam polishing of the sample at an angle in order to expose and laterally widen the interlayer.
- 2) Chemical composition determination of the interlayer and its corresponding interfaces with the substrate and coating, by local and quantitative AES measurements.
- 3) Local electrochemical characterization of the interlayer material reactivity using a microcapillary technique in order to determine its corrosion susceptibility in physiological simulating solution.

The three characterization steps are further described in the following.

### 2.2.2 Ion beam angled polishing (wedge-milling)

In order to expose and access the buried interlayer material for compositional and electrochemical characterization, ion beam polishing was conducted on the coated samples with an IM4000 Ion Milling System (Hitachi). Using an Ar ion beam (6 kV accelerating voltage, 1.5 kV discharge and 0.09 cm<sup>3</sup>/h Ar gas flow), a "wedge-like" profile was sputtered into the sample, exhibiting a deeper center and shallower edges, as seen in the schematic of Fig. 2.2. The beam irradiation angle, referring to the angle formed by the axis of rotation (normal to the sample surface) and the beam's center axis,

can be set from  $0^\circ$  to  $90^\circ$ . The eccentricity of the ion beam (from the beam center) can be set from 0 to 5 mm; the range of central uniform sputtering increases with larger eccentricity. For this study, an irradiation angle of  $70^\circ$  and an eccentricity of 0 was used. The sample was ion polished until the substrate was reached and visually revealed. With these parameters, the substrate is exposed, and the interlayer spread laterally up to ca. 1000 times its deposited thickness. After this ion beam polishing procedure, the sample will be referred to as a *wedge-milled sample*, whereas the term *coated sample* will be used prior to the ion beam polishing procedure. The lateral width of the wedge-milled interlayers varies between the samples, as it is dependent on the time at which the ionic polishing was stopped (i.e. longer polishing results in a narrower interlayer). The ion polishing process was simply stopped once the substrate could be visually seen, so additional minutes between samples resulted in slight variation in the width of the exposed interlayer.

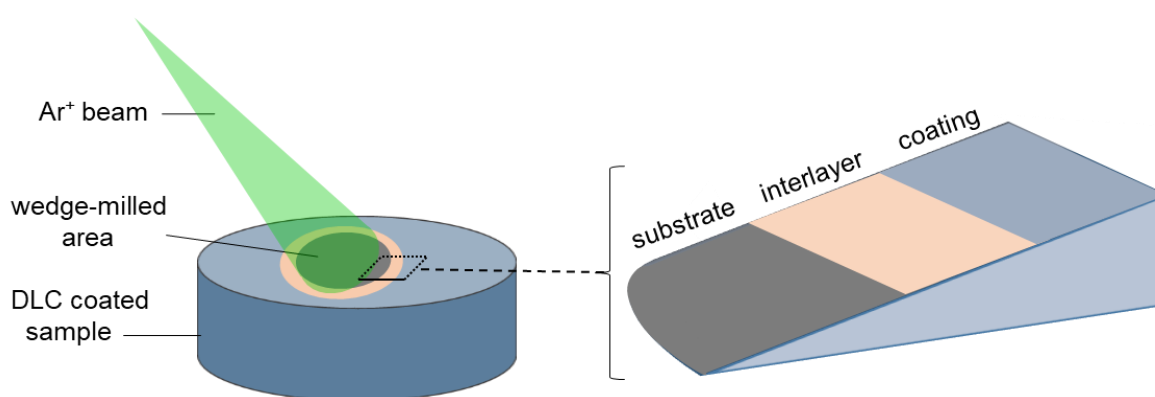


Fig. 2.2: Schematic of  $\text{Ar}^+$  beam polishing at an angle of a DLC coated substrate with an interlayer. A wedge-like profile is milled into the sample exposing the underlying materials.

### 2.2.3 Auger electron spectroscopy (AES) analysis of the interlayer/interfaces

Local surface characterization (chemical composition) was carried out with a Physical Electronics PHI 4300 scanning Auger microscopy (SAM) system operating at electron beam parameters of 5 kV (30 nA) and with a cylindrical mirror electron energy analyzer at 0.6% energy resolution. AES measurements were performed with a lateral resolution in the micrometer range and a typical depth sensitivity of 2-4 nm. The chemical composition of the wedge-milled interlayer/interfaces was determined by aligning 30 consecutive measurement points (with recording of all relevant element specific peaks) across the wedge-milled sample, from the Ti substrate, across the interlayer and into the DLC. As opposed to performing one conventional linescan with this equipment (which only acquires 3 energies; one of the peak, two of the background), the multi-point approach allows for the collection of the full relevant spectra at each specific point, providing more chemical binding information. The term *multipoint-linescan* will be used to refer to this approach. The area of analysis was pre-sputtered with a 2 kV Ar beam (2 x 2 mm) before measuring in order to remove any native oxide layer formed after the wedge-milling of the sample. After collection of the raw spectra, the data was analyzed using MultiPak 8.2 software (provided by Physical Electronics). The atomic concentration (at%) at each point was determined from its derivative spectrum, based on software built in sensitivity factors.

In AES an electron beam is used to strike the sample of interest, causing a core level electron (from the K shell for example) to be ejected from an atom in the sample's upper most surface (less than 100 Å in depth). An electron from a higher shell can drop down to fill the vacancy of the ejected electron. Following this transition, the atom may emit a third electron in order to release the excess energy from the excited state ion. The emitted electron is referred to as the *Auger electron* [86]. When transitions involving core levels close to the valence band or even valence band electrons are considered, useful information about the chemical environment can be obtained in addition to the simple composition analysis. Well-known examples of chemical binding analysis can be found for the C(KLL) and O(KLL) transitions where the valence band electrons are involved [87]. These transitions are referred to as KVV transitions and the final state relaxation effects and induced kinetic energy peak shape changes can be linked to different oxides or carbides present on the surface. Therefore, for each element (Ti, C, O, and the interlayer element), linear least square fitting (LLSF) was carried out on the at% composition curves in order to separate the different chemical states (such as carbidic forms) contributing to the spectra. Absolute identification of the formed compound based on Auger transitions is however difficult so that assigning peak shapes to reference spectra from known components is performed in this paper and this procedure allows, at least in a semi-quantitative way, identification of the compound or element. In this study the peak shape structures were compared with previously published raw reference spectra, an example of an AES element spectra fitting is presented in section 2.3.2.

#### 2.2.4 Macro and local microcapillary electrochemical characterization

Macro-electrochemical (consisting of a characterization area in the cm<sup>2</sup> range) measurements were first conducted on two coated samples with different interlayers, Ti/Co/DLC and Ti/Cr/DLC, using a Metrohm-Autolab PGSTAT30 potentiostat. A three-electrode electrochemical cell, shown in Fig. 2.3, was used with an exposed working electrode (WE) diameter of 0.5 cm (area of 0.2 cm<sup>2</sup>) and an electrolyte volume of 100 mL. A 3M silver/silver chloride (Ag/AgCl) reference electrode (RE, from Metrohm) was used with a glass Luggin capillary as an electrolyte bridge and a platinum (Pt) rod as the counter electrode (CE). A potential scan rate of 1mV/s was applied for potentiodynamic polarization experiments. The macroscale measurements on the coated samples (before ion beam polishing) were compared to local-electrochemical (consisting of a characterization area in the μm<sup>2</sup> range) measurements in order to demonstrate the influence of the characterization area size on the electrochemical behavior of a coated sample.

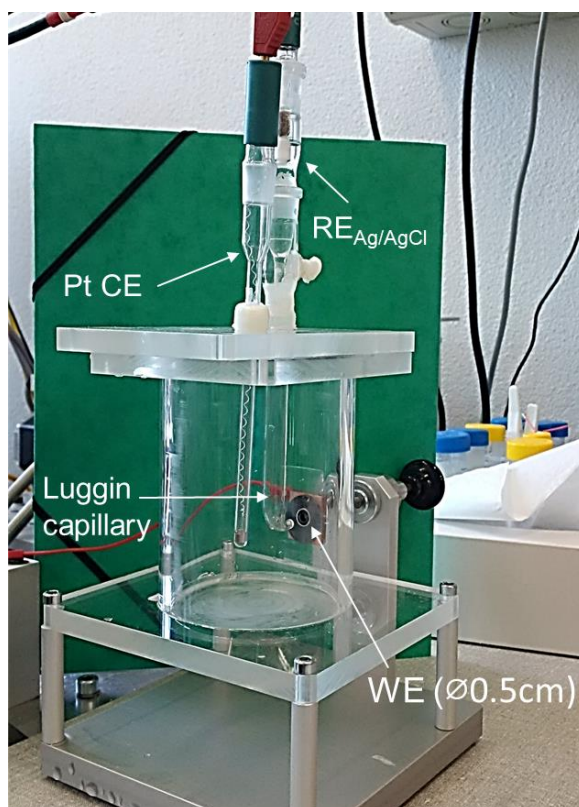


Fig. 2.3: Three-electrode macro-electrochemical cell consisting of: a platinum counter electrode (Pt CE), a 3 M silver/silver chloride reference electrode ( $RE_{Ag/AgCl}$ ) with a Luggin capillary, and an exposed working electrode (WE) area of diameter 0.5 cm.

Local-electrochemical measurements were performed with the microcapillary technique (an overview of the technique is presented by Suter and Böhni [88]). The technique utilizes a glass capillary filled with electrolyte whose tip diameter can be adjusted from ca. 1-1000  $\mu\text{m}$  by heating and pulling. In these experiments, a tip diameter of 70  $\mu\text{m}$  (area of  $3.85\text{E-}5\text{ cm}^2$ ) was used. The tip of the capillary is coated with silicone sealant, in order to confine the electrolyte within the characterization area upon contact with the WE surface. A 3M Ag/AgCl RE, was connected to the capillary through an electrolyte bridge tube, and a Pt wire CE was inserted into the capillary holder, as depicted in Fig. 2.4. A high-resolution potentiostat (Jaissle 1002T-NC-3) with a current resolution of ca. 10 fA was used. The microcapillary setup is mounted into a modified lens socket of an optical microscope and the WE is fixed onto the microscope stage. This arrangement allows for precise positioning of the microcapillary by optically locating the desired characterization area through an objective lens and then switching to the microcapillary cell with the revolving nosepiece. An external telescopic sight is utilized in order to approach and place the capillary tip onto the sample. In all electrochemical measurements HyClone® Wear Testing Fluid (HyClone® WTF, Thermo-Scientific) of pH 7.4 was used as the electrolyte; it is bovine serum-based and designed to simulate human synovial fluid, containing all the relevant body ions (phosphate, chloride, etc.) and 30 g/L of proteins.

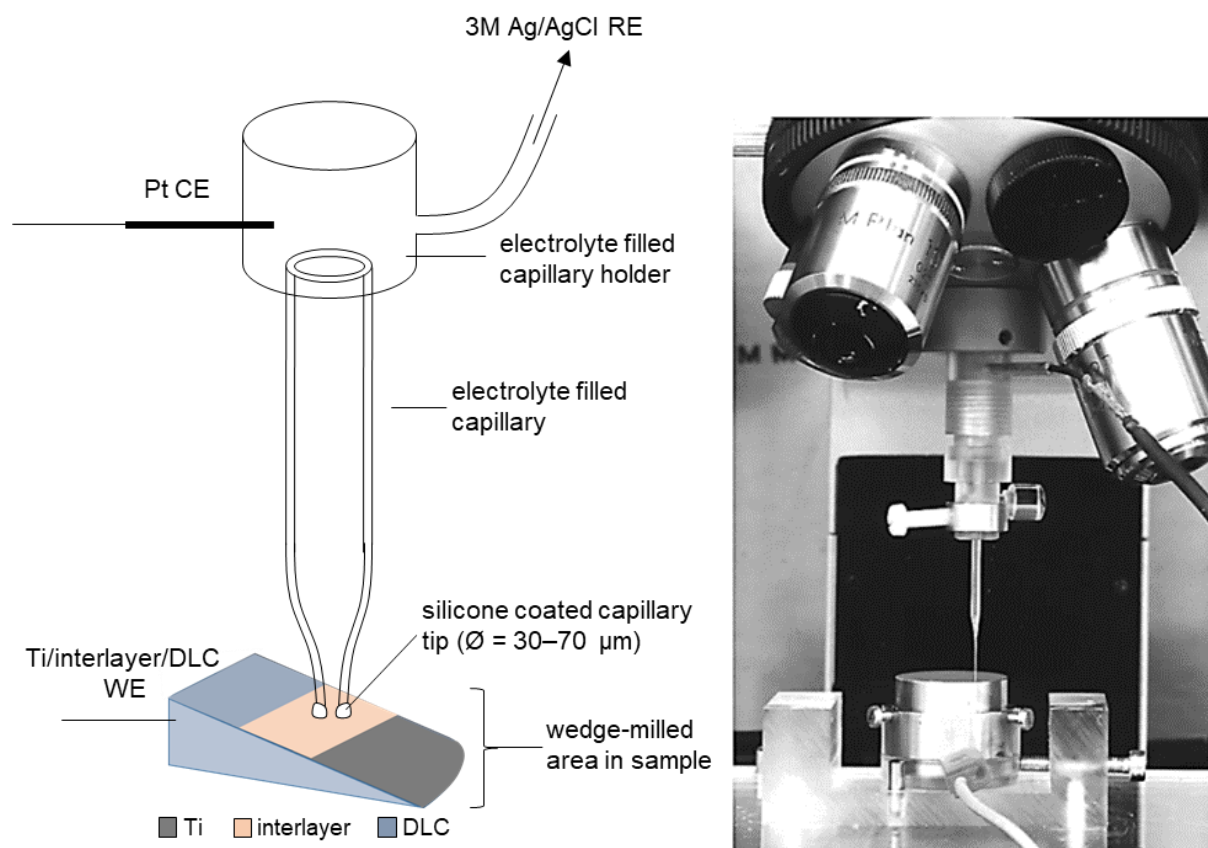


Fig. 2.4: (left) Schematic of the use of the microcapillary technique for local electrochemical characterizations. In this case, the exposed area (working electrode, WE) is a wedge-milled Ti/interlayer/DLC area. (right) photograph of the microcapillary mounted in an optical microscope.

The microcapillary electrochemical technique was then later applied for a more systematic local characterization of the wedge-milled samples, presented in sections 2.3.3 and 2.3.4. Two types of characterizations were conducted: i) 24 h OCP measurements on the substrate (Ti), interlayer and DLC area of the wedge-milled sample and, ii) Potentiodynamic polarization measurements on each component using a 1 mV/s potential scan rate, starting in the cathodic domain at  $-200 \text{ mV}_{\text{Ag/AgCl}}$  from the corrosion potential ( $E_{\text{corr}}$ ), up to  $1200 \text{ mV}_{\text{Ag/AgCl}}$ . A capillary diameter between 30-70 μm was used, depending on the lateral width of the wedge-milled interlayer.

It has to be mentioned that while Si, Cr and Si-DLC are all relevant interlayers commonly used in practice, the purpose of using Co as an interlayer was simply to create a very electrochemically active Ti/Co/DLC model sample, in order to validate the approach. However the chemical stability of the Co/DLC interface is definitely also of interest, as DLC coated CoCrMo implants are also found.



## 2.3 Results and Discussion

### 2.3.1 Electrochemical characterization of DLC surfaces on interlayers

Macro and local electrochemical characterization was performed on the DLC coated surfaces with Hyclone® WTF and compared for two coated samples with interlayers; Co and Cr. The macro-electrochemical cell consisted of a WE diameter of 0.5 cm, and the microcapillary used for these local measurements had a WE diameter of 70  $\mu\text{m}$ . This comparison was performed in order to demonstrate the dependency of the characterization area (WE area exposed to the electrolyte) on the electrochemical response of a coated surface, and how it relates to coating defects. Fig. 2.5 shows the macro-electrochemical potentiodynamic polarization measurements (represented by solid lines) of the Ti/Co/DLC and Ti/Cr/DLC surfaces along with their respective local-electrochemical measurements (dashed lines).

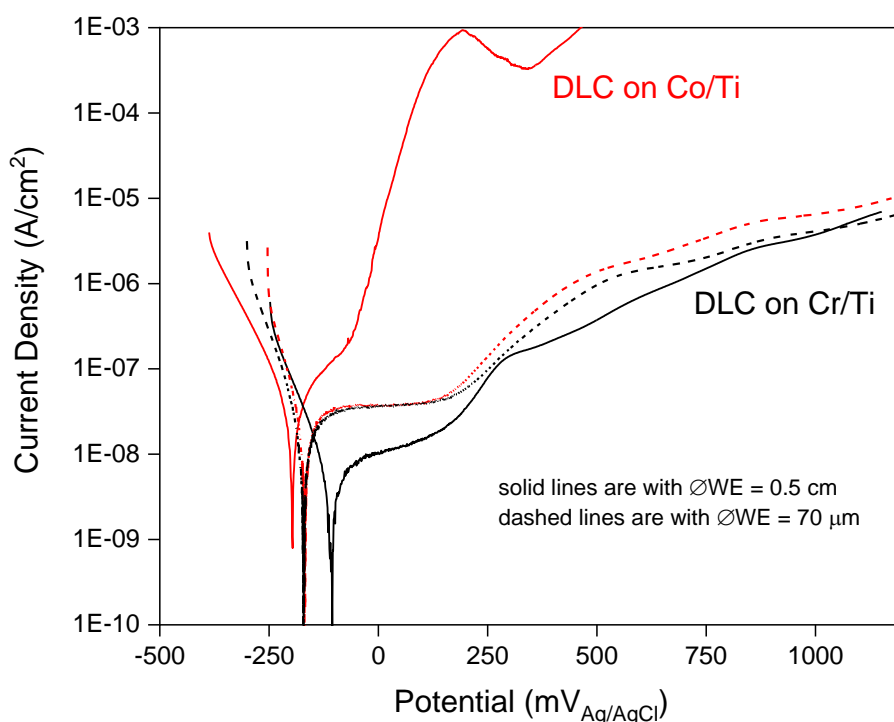


Fig. 2.5: Electrochemical potentiodynamic polarization curves of DLC coated samples performed with macroscale cell ( $0.2 \text{ cm}^2$  working area), solid lines, and microcapillary ( $3.85\text{E-}5 \text{ cm}^2$  working area) dashed lines. Electrolyte used was Hyclone® WTF at room temperature.

Firstly, considering only the polarization curves performed with the macroscopic cell; it is evident that the two solid-lined curves show very different behavior from one another and are highly dependent on the underlying interlayer material. Considering the macro-measurement on the Ti/Co/DLC (red solid curve) sample, it exhibits a relatively low corrosion current density ( $i_{\text{corr}}$ ) of ca.  $3.5\text{E-}8 \text{ A/cm}^2$  due to the protection of most of the surface by the DLC coating and an  $E_{\text{corr}}$  of ca.  $-200$

$\text{mV}_{\text{Ag}/\text{AgCl}}$ . However, after small anodic polarization, a rapid increase in current occurs above ca.  $-70 \text{ mV}_{\text{Ag}/\text{AgCl}}$  from  $2.0\text{E}-7 \text{ A/cm}^2$  to very active values of  $1.0\text{E}-3 \text{ A/cm}^2$  where the measurement was eventually terminated. At pH 7.4, Co is oxidized to  $\text{Co}^{2+}$  above a potential of ca.  $-700 \text{ mV}_{\text{Ag}/\text{AgCl}}$  (as indicated by the Co- $\text{H}_2\text{O}$  Pourbaix diagram [89]). Considering the electrochemical behavior of the coated sample in Fig. 2.5, it can be seen that the observed "breakdown" potential lies well above  $-700 \text{ mV}_{\text{Ag}/\text{AgCl}}$ , where Co becomes unstable. It then becomes obvious that the major current contribution is coming from the underlying activated Co interlayer, due to the presence of a substantial defect in the DLC coating somewhere within the characterization area, hence inducing rapid destabilization of the coated system. However if the deposited interlayer is a passive material, or is reacting with the coating or substrate to form a new material (such as a carbide), the electrochemical behavior and corrosion susceptibility of this underlying material is then not as predictable anymore. Observing for example the macro-electrochemical measurement of the Ti/Cr/DLC sample (solid black curve), there are many undefined features in the current evolution which cannot be directly correlated with either the coating, interlayer or substrate reactivity, and hence correlating the electrochemical response to coating defects becomes complicated. Initially, the curve exhibits a low  $i_{\text{corr}}$  of ca.  $7\text{E}-9 \text{ A/cm}^2$  at an  $E_{\text{corr}}$  of  $-100 \text{ mV}_{\text{Ag}/\text{AgCl}}$ , followed by a short stable region (evidenced by slight plateau) until ca.  $150 \text{ mV}_{\text{Ag}/\text{AgCl}}$ . This can again be attributed to the overall protection provided from the DLC coating, but is also consistent with the good intrinsic passivation behavior of Cr. In the neutral pH range, Cr is protected by a very stable Cr-oxide ( $\text{Cr}_2\text{O}_3$ ) film above a potential of ca.  $-1210 \text{ mV}_{\text{Ag}/\text{AgCl}}$  (as indicated by the Cr- $\text{H}_2\text{O}$  Pourbaix diagram [90]). However, above ca.  $200 \text{ mV}_{\text{Ag}/\text{AgCl}}$ , transpassive dissolution of  $\text{Cr}_2\text{O}_3$  to  $\text{CrO}_4^{2-}$  is thermodynamically possible [90]. Observing Fig. 2.5, it is around this potential ( $150 - 200 \text{ mV}_{\text{Ag}/\text{AgCl}}$ ) that the current starts to gradually increase during anodic polarization. Hence, this feature in the curve could be attributed to Cr electrochemical oxidation at coating defects. However, oxidation of C to  $\text{HCO}_3^-$  species is also postulated at this potential and pH, considering the C (in the form of graphite) Pourbaix diagram [91]. Although DLC itself is a mix of hydrogen and carbon and is considered to be inert [92], it can become destabilized with anodic polarization and contribute to the current response in the curve of Fig. 2.5. Therefore, it is difficult to decipher whether this oxidation current is a contribution of the DLC instability itself, or of the underlying Cr-based interlayer at local DLC coating defects. Without this knowledge, the chemical stability and efficiency of the interlayer cannot be determined. By significantly decreasing the characterization area on a coated sample, larger and corrosion critical defects in the coating can be excluded. The current response of the electrochemical measurement therefore becomes more representative of the intrinsic behavior of the coating itself. The distribution of defects and their influence on the current signal can then be better assessed by comparing electrochemical measurements performed with different characterization areas.

Observing the very different current evolution of the local microcapillary measurements in Fig. 2.5 (dotted lines), the role of defects on the electrochemical behavior becomes obvious. Firstly, it can be seen that unlike the macroscale measurements, the local potentiodynamic polarization curves on DLC are nearly identical to one another, showing the same current evolution regardless of the underlying interlayer material. Therefore, it can be postulated that the prominent potential domain

established at a current density of ca.  $3.5 \times 10^{-8}$  A/cm<sup>2</sup> between ca. -100 mV<sub>Ag/AgCl</sub> to 150 mV<sub>Ag/AgCl</sub>, (evidenced by a plateau) can be attributed to the chemical stability of the DLC itself. After which, the gradual increase in current may indeed be attributed to the oxidation/dissolution of graphite micro-particles within the DLC matrix. The main difference between the macroscale and local polarization curves is found for the Ti/Co/DLC coated sample. Comparison between these two current evolution curves evidently demonstrates how the electrochemical measurements on a coated sample are highly dependent on the size of the characterized area. The measured current can show completely different behavior in the event that a substantial coating defect is either included or excluded in the exposed working area. Therefore, care must be taken when interpreting the macroscopic electrochemical behavior of a coated surface. Since a potentiodynamic polarization curve displays a sum of the currents generated by all the reactions occurring at the coating surface, interlayer/interfaces, as well as the substrate, distinguishing the origin of each contribution is not always straightforward.

To become even more predictive and formulate corrosion mechanisms of complex multi-material interfaces, a methodology for separating the current contributions and related corrosion susceptibility of the coating, interlayer, and substrate is proposed. The experimental characterization combines: i) angled ion beam polishing generating a wedge to expose the buried interlayer, ii) characterization of the chemical composition of the actual deposited interlayer/interfaces by AES, and iii) specific local electrochemical characterization of each new interlayer material.

### 2.3.2 Composition characterization of the interlayer and interfaces by AES

After ion beam polishing of the samples, the chemical composition of the wedge-milled interlayers could be determined with the multipoint-linescan AES approach described in section 2.2.3. For visualization purposes, Fig. 2.6 shows a SEM image of the wedge-milled Ti/Si/DLC sample used for AES and microcapillary electrochemical characterization. The AES data of this sample will be used as an example to demonstrate the analysis performed to separate the AES spectra into their respective compounds and elements.

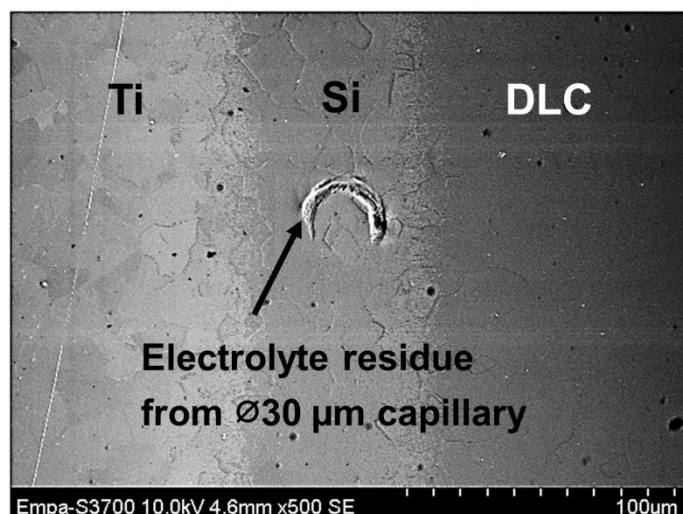


Fig. 2.6: SEM image of wedge-milled Ti/Si/DLC sample after local electrochemical characterization with the microcapillary. Si interlayer has been laterally exposed and its corresponding interfaces with Ti and DLC.

Fig. 2.7a shows the stacked C(KLL) spectra, plotted as function of the kinetic energy (KE), relating to a sequence of the measurement points across the Ti/Si/DLC wedged interlayer.

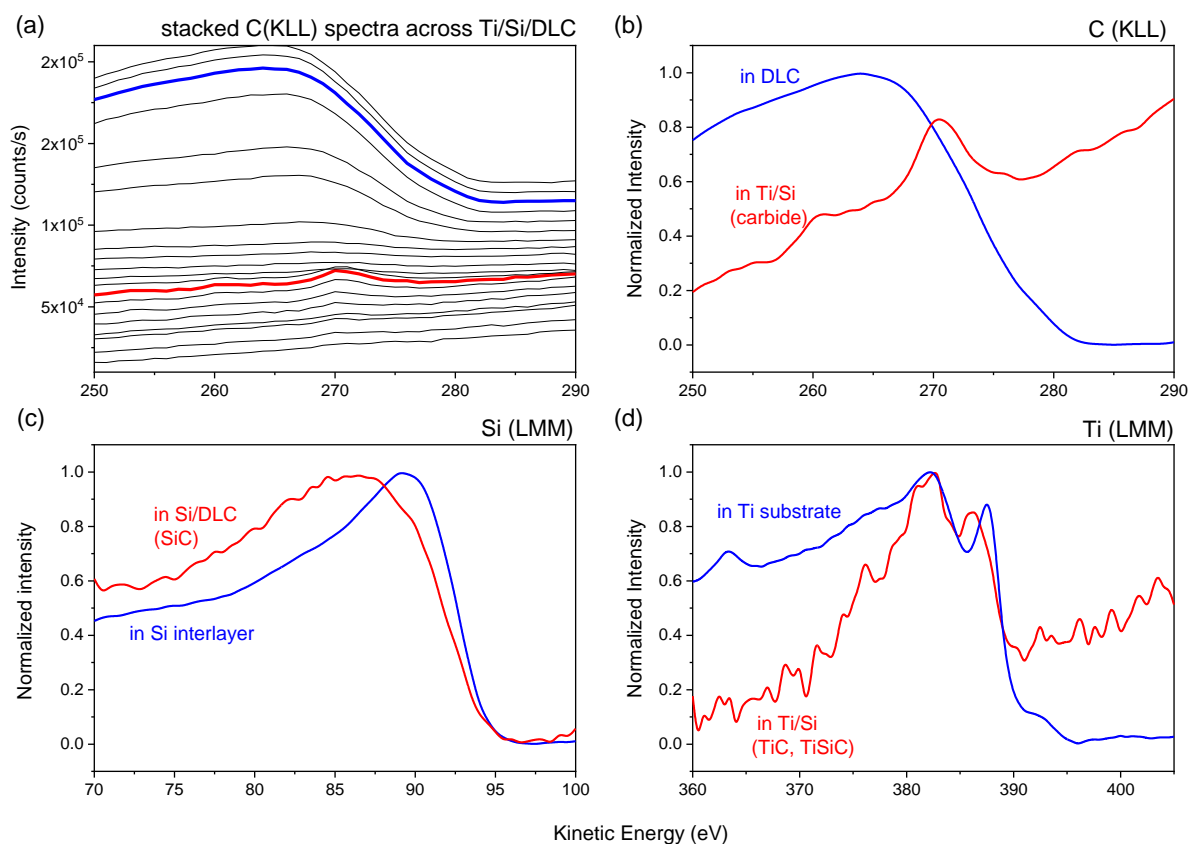


Fig. 2.7: AES spectra used to fit the at% composition curves for the wedge milled Ti/Si/DLC sample of Fig. 7a. a) Stack plot of C(KLL) spectra, b) C(KLL) spectra measured in DLC and Ti/Si interface, c) Si(LMM) spectra measured in Si interlayer and Si/DLC interface, d) Ti(LMM) measured in Ti substrate and Ti/Si interface.

It can be seen that the C(KLL) spectrum of the carbon detected at the Ti/Si interface (at and around the 8<sup>th</sup> spectrum from the bottom, in bold red) has a different shape than the spectrum obtained in the DLC (at and around 18<sup>th</sup> spectrum, in bold blue). These two types of specific C(KLL) spectra are presented separately in Fig. 2.7b for clarification. The spectrum obtained on the DLC has the typical appearance of C-C bonds found in DLC; with a peak maximum at 265 eV, and to the left a linear decreasing tail to 254 eV and then a further signal intensity decrease to ca. 248 eV. This spectra shape is analogous to a reference AES spectrum published by Hauert et al. [93]. The spectrum obtained at the Ti/Si interface location displays a main sharper peak at 270 eV and a much smaller peak at 260 eV, analogously to a reference measurement on SiC [93]. Carbides generally have very similar C(KLL) peak shapes, a maximum around 270 eV and quickly decreasing tails, with the non-carbon component sometimes only slightly influencing the spectrum. At this point, the different peak shape can therefore be assigned to carbon in carbidic form (the type of carbide becomes obvious once the Ti and Si spectra are analyzed). All the C(KLL) spectra have then been separated into these two reference contributions (C as DLC, and C as carbide at the Ti/Si interface) by linear least square fitting (LLSF), in order to produce the at% composition curve of C, as can be seen in Fig. 2.8a. This AES data analysis also revealed a certain contribution of C in carbidic form at the Si/DLC interface as well.

Similarly to the C(KLL) spectra, the Si(LMM) spectra were analyzed in a stack plot and separated into different compounds by LLSF. The spectra obtained from the measurement points at the Si interlayer and at the Si/DLC interface were used for fitting and are displayed in Fig. 2.7c. The peak shape of the spectrum from the interlayer can be assigned to pure Si, with its pronounced peak at 89 eV. The spectrum from the Si/DLC interface (in red) can be assigned to Si as SiC, with its broad peak at a lower KE of 86 eV, analogously to the Si(LMM) reference spectra published by Hauert et al. [93] and Kosiba et al. [94]. Therefore with agreement between both C(KLL) and Si(LMM) spectral fittings, this interface can indeed be assigned to SiC. This is also expected since it was previously measured that when depositing DLC onto Si, a SiC is formed at this interface [93].

Whereas the presence of SiC at the Si/DLC interface could unambiguously be resolved, the presence of SiC at the Ti/Si interface could not be detected, nor any other altered Si peak shape (such as the presence of TiSi). Since the LLSF analysis did not reveal a SiC at the Ti/Si interface, this indicates that the C at that interface can rather be assigned to TiC or TiSiC based on the analysis of the C(KLL) peak. This experimental observation makes sense, as TiC is the more energetically favorable carbide, having a standard Gibbs energy of formation ( $\Delta G_f^\circ$ ) of -43.2 kcal/mol at 25°C, as opposed to -15.0 kcal/mol for SiC [95]. The favored TiC formation would hence produce a much higher intensity in the AES spectrum at the Ti/Si interface. Although the presence of TiSi at the Ti/Si interface is also expected, kinetic energy separation of a TiSi peak from the pure Si signal may be below the resolution of the performed AES measurements.

Ti(LMM) spectra were separated in peaks of pure Ti in the substrate, and Ti at the Ti/Si interface (in red), as shown in Fig. 2.7d. A different chemical state of Ti at the interface compared to the one of pure Ti in the substrate could be resolved, as seen in Fig. 2.8a. However assigning the energy shifts

and altered peak shapes to a specific chemical component is difficult, as it may be TiC, TiSi, or TiSiC and only few AES reference data exist for this system. The main difference between the spectra of Fig. 2.7d is in the tail intensities at kinetic energies below the highest peak at 382 eV (note the peak intensity is normalized, resulting in some noise), as well as a slight offset between the right shoulder peaks at ca. 386 eV. Comparing these measurements to reference spectra of Ti, TiC and TiSi found in Maline et al. [96], both TiC and TiSi show a reduced intensities at kinetic energies below the 382 eV peak, compared to pure Ti, whereas only TiC shows a slight shift of the right shoulder peak to 386 eV. Therefore, it is suggested that a larger part of the interface state of the Ti Auger signal originates from the presence of TiC at this interface. This conclusion is also supported by the fact that the presence of TiSi could not be resolved on the Si(LMM) peak.

The TiC at the Ti/Si interface likely originated during the deposition process. As the PACVD chamber and sample holder contains DLC remnants from prior deposition processes, carbon can be sputtered from the sample holder and interact with the substrate during the Ar sputter cleaning step. The small amount of oxygen detected (as seen in Fig. 2.8a) can on the other hand mainly be assigned to oxygen recontamination during the long AES measurement, since oxygen is also detected on the pure Ti substrate. However, a slight enrichment toward the Ti/Si interface may indicate that a smaller amount of oxygen, below 5 at%, may already be present at this interface from the deposition process. Metallic Ti is extremely reactive and this detailed AES analysis shows that oxygen as well as carbon contamination can be expected in any industrial deposition processes involving such reactive surfaces.

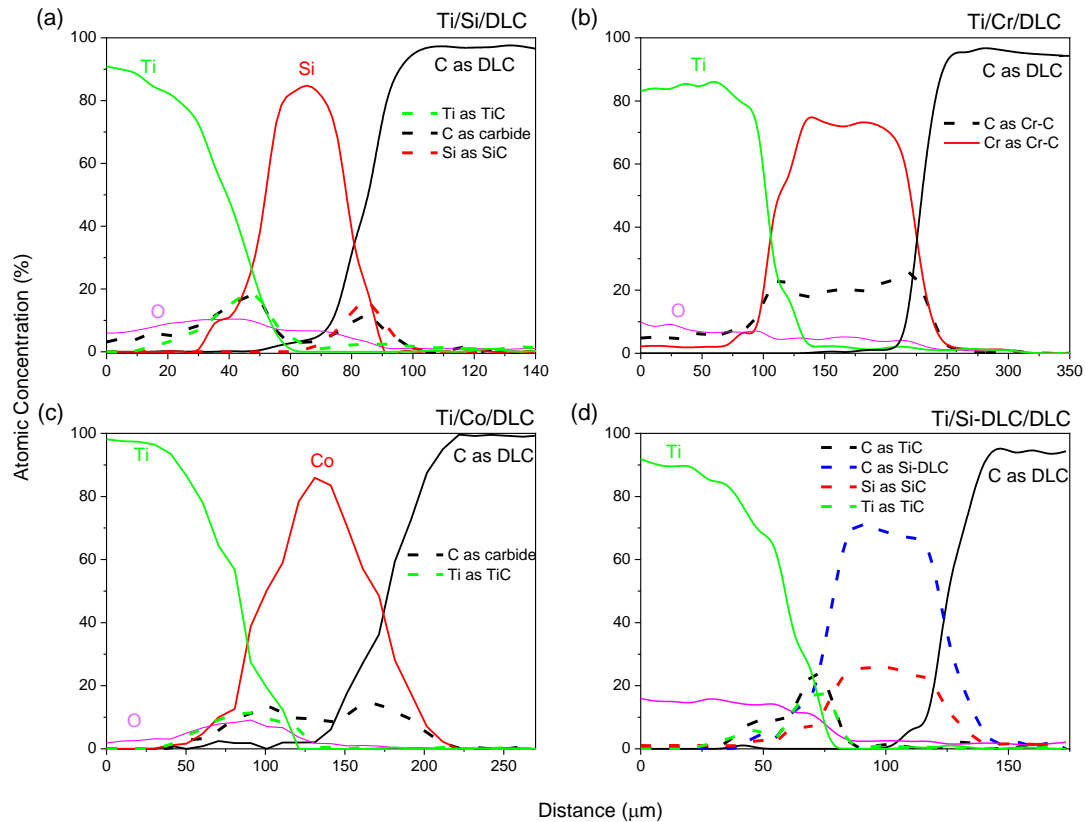


Fig. 2.8: AES at% composition curves of wedge-milled samples: a) Ti/Si/DLC, b) Ti/Cr/DLC, c) Ti/Co/DLC and d) Ti/Si-DLC/DLC. Carbide forms have been assigned by comparison to published reference spectra.

The AES spectra of the other wedge-milled samples were analyzed in a similar manner to that of the Ti/Si/DLC example, and their at% composition curves are presented in Fig. 2.8b-d. Observing the at% curves of the Ti/Cr/DLC sample in Fig. 2.8b, it can be seen that the Cr interlayer is in fact not pure Cr, but also contains ca. 20 at% C as carbide throughout the interlayer with a slight increase at the interfaces. Although C(KLL) carbide peaks are very similar, there is a feature in the C(KLL) chromium carbide (Cr-C) peak which makes it identifiable from TiC, a slight shoulder to the right of the main peak at 275 eV [87], as seen in Fig. 2.9.

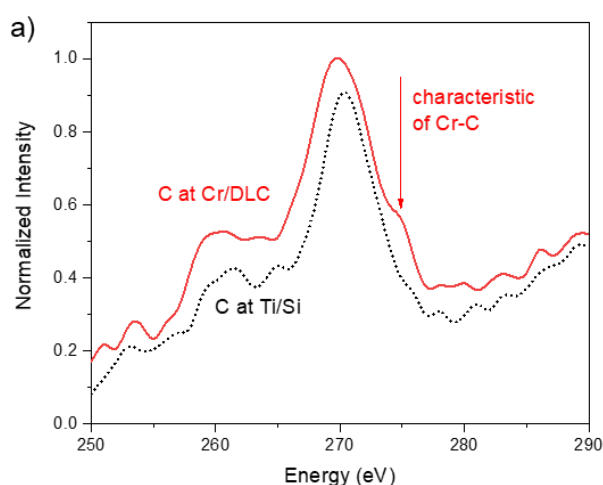


Fig. 2.9: AES of normalized C(KLL) spectra at a Cr/DLC interface compared to the spectra at a Ti/Si interface (peak assigned to TiC), the shoulder at 275 eV is characteristic of Cr-C. The peaks have been slightly offset for comparison purposes.

Therefore, this carbide could be assigned to Cr-C chemical bonds. Cr-C is one of the most energetically favored carbides, and can form spontaneously even at room temperature; at 25°C, the  $\Delta G^\circ$  is -22.7 kcal/mol for  $\text{Cr}_3\text{C}_2$ , -44.6 kcal/mol for  $\text{Cr}_7\text{Cr}_3$ , and -96.9 kcal/mol for  $\text{Cr}_{23}\text{C}_6$  [95]. As Cr has a very high tendency to bond with carbon, it may be that the Cr in the thin interlayer reacted with residual C in the chamber during deposition. The Ti/Cr interface likely contains a mixture of both favorable TiC and Cr-C so that their contributions are not easily separated. The at% composition curves of the wedge-milled Ti/Co/DLC model sample (active corroding interlayer) is shown in Fig. 2.8c. The deposited interlayer is mainly pure Co with a slight carbide contribution towards the interfaces, obtained by splitting of the C(KLL) spectra. At the Ti/Co interface, the Ti(LMM) spectra could be split and assigned to TiC. At the Co/DLC interface, while splitting of the C(KLL) spectra revealed a carbide contribution at this interface, the Co(LMM) spectra could not be further split nor assigned to a Co carbide (Co-C). This is likely due to the fact that Co has a high atomic number (many electrons shells) and the Co(LMM) transition does not involve the valence band, which contains bonding and chemical environment information. Further Co-C formation is

rather unfavorable, having a  $\Delta G^\circ$  of +9.0 kcal/mol for  $\text{Co}_3\text{C}$  at 25°C [97], so the bonds between Co and C are rather weak and do not strongly alter the electron configuration of the Co. Some literature has also reported that when depositing DLC on Co, catalytic formation of a graphite layer during initial stages of growth can occur [98,99], resulting in poor chemical stability of this interface. The carbide peak at the Co/DLC interface may therefore also contain a graphitic contribution, however this will be further investigated in future work.

The AES analysis of the Si-DLC interlayer is shown in Fig. 2.8d and it is composed of ca. 30% Si as SiC, and 70% C as carbide, consistent with previously published XPS depth profiling data on the same interlayer [100].

The AES chemical binding and surface composition characterization of the different wedged interfaces revealed numerous new materials with unknown reactivity in aggressive environments. These deposited interlayers including various carbide phases may show different electrochemical reactivity and corrosion resistance compared to that of, for example, pure metals or bulk carbide analogs that are anyway difficult to synthesize. Hence, direct local electrochemical characterization of the interlayer with its new interfaces with the microcapillary technique is of great interest and is presented in the next section as a third part of the characterization methodology.

### 2.3.3 Interlayer electrochemical reactivity investigated by potentiodynamic polarization

Since the local-electrochemical measurements allow for more representative characterization of the intrinsic electrochemical response of DLC in absence of coating defects, the coating specific anodic polarization curves recorded for the DLC in Fig. 2.10a-d demonstrate that a "defect free" DLC coating does not behave like an electrical insulator, but is somewhat conductive. This is evidenced by a measurable local current of ca.  $3.5\text{E-}8 \text{ A/cm}^2$ . For all the coated samples with different interlayers considered, the local electrochemical potentiodynamic polarization measurements on the DLC showed reproducible, nearly identical, and relatively high current densities. The  $E_{\text{corr}}$  of the DLC is consistently ca.  $-170 \text{ mV}_{\text{Ag/AgCl}}$ , followed by a stable current density plateau at  $3.5\text{E-}8 \text{ A/cm}^2$  regardless of the underlying interlayer, indicating that the electrochemical properties are controlled by the DLC.

The different local-electrochemical potentiodynamic polarization investigation of the wedge-milled interlayers are also presented in Fig. 2.10, along with the electrochemical response of the Ti substrate and DLC measured on each coated sample (already discussed above). The target material used for the magnetron sputtering process of the corresponding interlayer was also characterized by means of the microcapillary technique (specific current evolution represented by dotted lines), so that the electrochemical behavior of the bulk material could be compared to the one of the deposited interlayer.



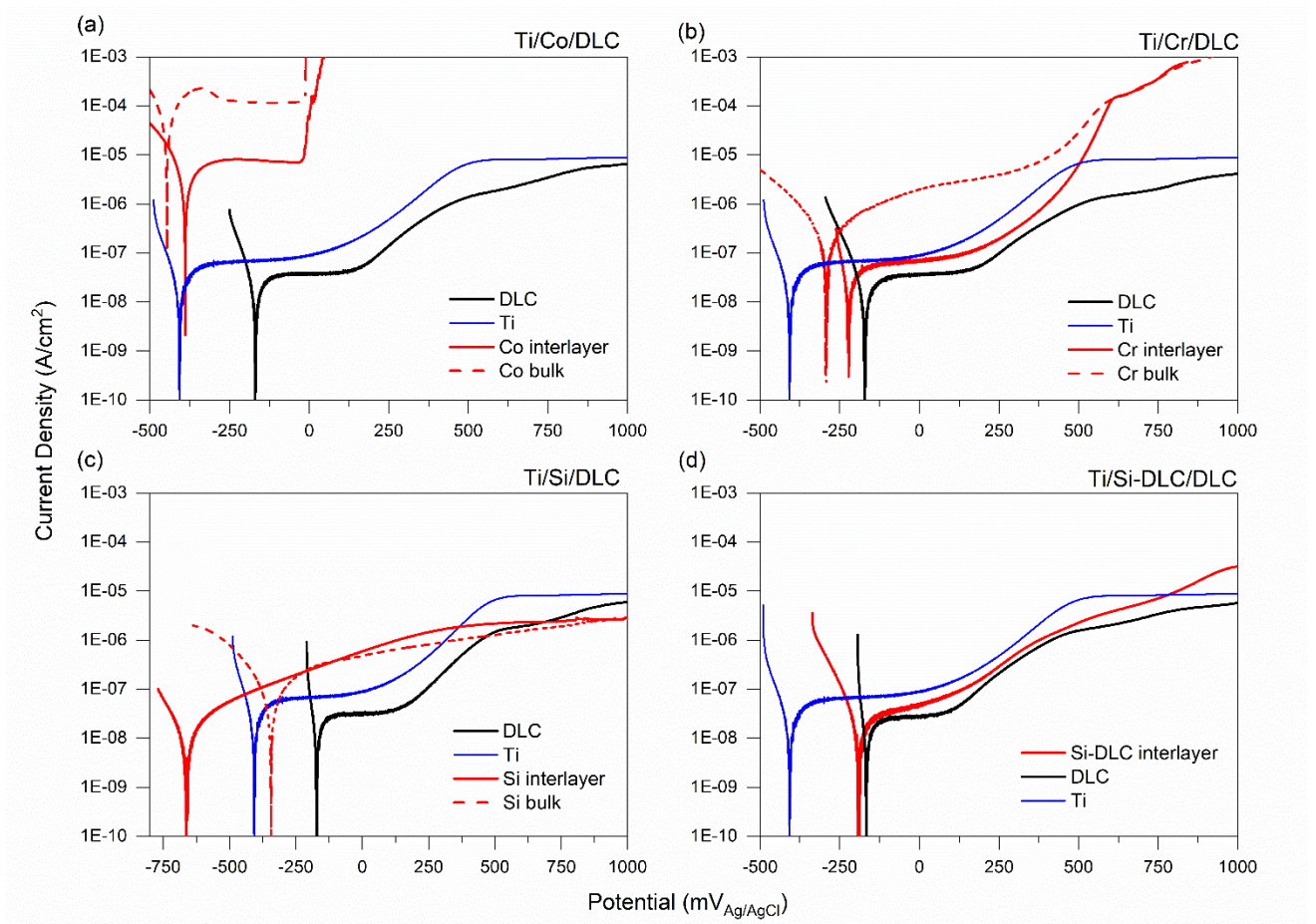


Fig. 2.10: Local electrochemical potentiodynamic polarization measurements conducted with microcapillary filled with HyClone WTF as electrolyte, on wedge-milled samples: a) Ti/Co/DLC, b) Ti/Cr/DLC, c) Ti/Si/DLC, d) Ti/Si-DLC/DLC. Corresponding interlayer magnetron sputter targets were also characterized to show differences in behavior of bulk material.

Wedge-milling of the coated samples makes the interlayers and their new interface materials easily accessible to the microcapillary for electrochemical characterization, due to the lateral widening. For example, a residual ring left after microcapillary characterization performed with a 30  $\mu\text{m}$  diameter capillary is shown on the Si area of the Ti/Si/DLC wedge-milled sample, validating the correct positioning of the capillary (Fig. 2.6). The ring is composed of residual HyClone® WTF and Si corrosion products (as characterized by SEM/EDX).

The first case presented is the local polarization behavior of the model Ti/Co/DLC wedge-milled sample, Fig. 2.10a. The substrate shows typical electrochemical behavior for Ti with a low  $E_{\text{corr}}$  at -400  $\text{mV}_{\text{Ag/AgCl}}$  (characteristic of reactive metals), followed by a passive domain (in the  $1\text{E}-7 \text{ A/cm}^2$  range) with a further increase of the passivation current starting at 100  $\text{mV}_{\text{Ag/AgCl}}$ , related to polarization induced oxide growth. As already mentioned, Co is known to be very active within the neutral pH domain so that a stark contrast between the Ti and Co polarization curves is expected, and indeed is observed. It can be seen that the current density evolution of the Co interlayer exhibits similar features compared to that of the bulk Co curve; a brief "pseudo" passivation (high measured

current density) domain from ca.  $-380 \text{ mV}_{\text{Ag/AgCl}}$ , until a pitting potential of ca.  $-10 \text{ mV}_{\text{Ag/AgCl}}$  is reached, where the current rapidly increases to very high values due to active dissolution. One difference is however that the bulk Co exhibits even higher current densities of ca.  $1\text{E-}4 \text{ A/cm}^2$ , approximately one order of magnitude higher than the Co interlayer does. Hence, even when a pure and active interlayer is present, its electrochemical reactivity in complex electrolytes such as Hyclone® WTF can still vary slightly from the bulk material. Nevertheless, comparison with the bulk behavior shows that the microcapillary technique was able to measure the active dissolution behavior of a 60 nm thick deposited Co interlayer separately from the substrate and coating response, and the method could now be applied to the more practice-relevant interlayer materials (Si, Cr-C, and Si-DLC).

The local electrochemical polarization measurement of the Cr-C interlayer (as characterized by AES in Fig. 2.9a) is shown in Fig. 2.10b, together with reference measurements on DLC and the bulk Cr target. It can be seen from the current density evolution that the Cr-C interlayer behaves neither as pure Cr, nor as DLC, but rather somewhere in between. Initially, the measured currents resemble the behavior of the DLC, having a similar low  $i_{\text{corr}}$  followed by a prominent passive plateau domain. This can likely be attributed to oxidation hindering induced by the C in the interlayer, resulting in analogous behavior as the C in the DLC. The current then increases exponentially between ca. 170 to 600  $\text{mV}_{\text{Ag/AgCl}}$  to ca.  $1\text{E-}4 \text{ A/cm}^2$ , after which the curve overlaps the pure Cr curve above 600  $\text{mV}_{\text{Ag/AgCl}}$ . The current increase in the intermediate potential domain (170 – 600  $\text{mV}_{\text{Ag/AgCl}}$ ) can be attributed to transpassive dissolution of Cr-oxide, analogously to the mechanism for a pure Cr surface. Some destabilization of the Cr-C bound within the interlayer may simultaneously be occurring and adding a contribution to the anodic current signal, similar to the C oxidation also seen in the DLC curve from a potential of 150  $\text{mV}_{\text{Ag/AgCl}}$ . The latter portion of the Cr-C interlayer curve (above 600  $\text{mV}_{\text{Ag/AgCl}}$ ) is then fully dominated by Cr-oxide transpassive dissolution. This example demonstrates how the local-electrochemical measurements can be utilized to more accurately assign the contributions of the current response to different surface reactions. The influence of the incorporation of C within the interlayer (in this case ca. 20 at%) could be identified as an improvement in the chemical stability, compared to the higher oxidation currents observed for pure chromium. Hence the Cr-C interlayer shows good chemical stability, given the potential is maintained at the  $E_{\text{corr}}$ , as demonstrated in the OCP measurement of the next section, or below the onset of active currents (between ca.  $-200 \text{ mV}_{\text{Ag/AgCl}}$  to 400  $\text{mV}_{\text{Ag/AgCl}}$ ). However if higher potentials are expected to be applied, such as in some sensor applications, the electrochemical stability of this particular Cr-C interlayer may not be suitable.

Regarding the Si-based interlayer, the local electrochemical characterization of the wedge-milled Ti/Si/DLC sample is presented in Fig. 2.10c, along with the one of the Si target used for the magnetron sputtering deposition. It can be seen that the  $E_{\text{corr}}$  of the sputtered Si interlayer, and the bulk Si differ. The polarization curve of the Si interlayer material shows a relatively active (low)  $E_{\text{corr}}$  of ca.  $-660 \text{ mV}_{\text{Ag/AgCl}}$  compared to the ones of bulk Si and titanium substrate, indicating it has the viability to corrode if coupled to the Ti. Although with increasing anodic potential the current density remains low, not exceeding ca.  $2\text{E-}6 \text{ A/cm}^2$ . The local electrochemical polarization curve of the bulk

Si demonstrates similar current densities, but with a much higher (nobler)  $E_{\text{corr}}$  of ca.  $-340 \text{ mV}_{\text{Ag}/\text{AgCl}}$ . The low currents in the potentiodynamic polarization curve may indicate a stable oxide on the interlayer and bulk Si, however from previous work [101], it was demonstrated that Si oxide is easily stabilized by anodic polarization. For this reason, OCP evolution monitoring presented in the next section combined with the potentiodynamic polarization information serves as a better diagnostic for assessing the surface oxide stability and corrosion susceptibility of Si.

Concerning the Ti/Si-DLC/DLC sample, since the Si-DLC is deposited from TMS gas, a bulk reference could not be characterized. The Si-DLC deposited interlayer exhibits somewhat similar behavior to that of DLC, as seen in Fig. 2.10d. This electrochemical current response is expected, as the material is essentially DLC doped with some Si. However, the chemical stability (plateaued current density up to ca.  $100 \text{ mV}_{\text{Ag}/\text{AgCl}}$ ) is not as good as the DLC, and stronger oxidation currents are measured at higher applied potentials. The reason why this interlayer seems to oxidize more readily than DLC is not completely understood, it may have to do with the presence of Si and destabilization of Si-C bonds. Specific oxidation mechanisms are not in the focus of this work, however this must be further investigated in the future.

In comparison to the  $E_{\text{corr}}$ 's of the interlayer materials presented in Fig. 2.10a-d, DLC always displays the noblest (most positive)  $E_{\text{corr}}$ . This means that in reference to the underlying materials, DLC could theoretically act as a cathode given its not fully insulating nature. Hence, if electrolyte penetrates the coating through a defect and reaches the interface material, galvanic coupling may occur at the interface of the noble coating and less noble underlying material. This phenomenon can accelerate the degradation process of the underlying material. Such a mechanism has also been used to describe the delamination in NaCl solution of conducting TiN coatings deposited on stainless steel, due to local galvanic coupling of the steel with the more noble coating [44].

### 2.3.4 Long-term interlayer stability assessment at OCP

Complimentary to the local-electrochemical potentiodynamic polarization measurements presented in the above section, the OCP evolution of the wedge-milled interlayers was also characterized by means of the microcapillary technique over 24 hours. This characterization avoids any anodic polarization oxidation effects and assesses the corrosive susceptibility at longer, freely corroding conditions. Fig. 2.11a shows a compilation of the OCP evolution measurements obtained for the Si-DLC, Cr-C and Si based interlayers, along with the OCP evolution of the Ti substrate for reference.

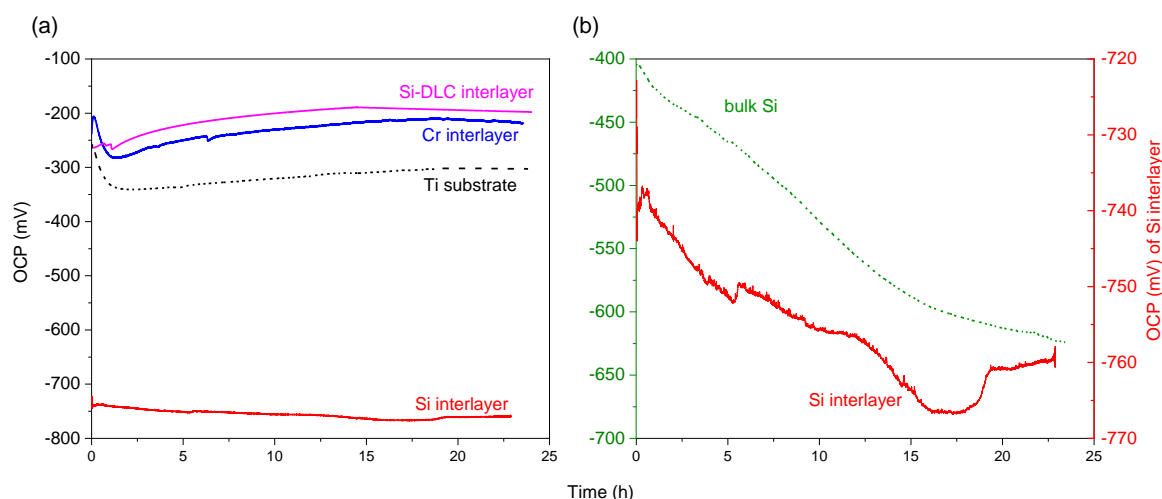


Fig. 2.11: Local open circuit potential (OCP) evolution measurements conducted with microcapillary filled with HyClone® WTF as electrolyte, on: a) Si-DLC, Cr-C and Si interlayers, and Ti substrate. b) Comparison of the OCP evolution of bulk Si (on left y-axis) and Si interlayer (on right y-axis).

It can be seen that the OCP evolution of the Cr-C interlayer stays at a consistently high and constant value of ca.  $-250 \text{ mV}_{\text{Ag}/\text{AgCl}}$ . From the C-H<sub>2</sub>O and Cr-H<sub>2</sub>O thermodynamic considerations (Pourbaix) at pH 7.4, Cr<sub>2</sub>O<sub>3</sub> and C are stable in this potential domain, indicating passivity of the interlayer. The Si-DLC interlayer also presents a consistently high OCP evolution around ca.  $-200 \text{ mV}_{\text{Ag}/\text{AgCl}}$ . The long-term OCP evolution of the Si interlayer, and bulk Si, however indicates very different stability behavior. The 24 h OCP measurement shows decreasing potentials, indicating progressive destabilization of the surface. It can be seen that the Si interlayer exhibits a continuous drop in potential, with transients, from ca.  $-720 \text{ mV}_{\text{Ag}/\text{AgCl}}$  to ca.  $-770 \text{ mV}_{\text{Ag}/\text{AgCl}}$ , better evidenced on an enlarged axis in Fig. 2.11b (on the right y-axis). It is important to consider that in the presence of only H<sub>2</sub>O, SiO<sub>2</sub> is stable above an equilibrium potential of ca.  $-1000 \text{ mV}_{\text{Ag}/\text{AgCl}}$  at ca. pH 7.4 (from the Si-H<sub>2</sub>O thermodynamic system [102]), so that the measured OCP values cannot yet be interpreted as representing a completely active corroding surface. The influence of proteins and additional species (phosphate, chloride, etc) in HyClone® WTF can however narrow the Si-oxide stability domain, so that a potential evolution from ca.  $-720 \text{ mV}_{\text{Ag}/\text{AgCl}}$  down to  $-770 \text{ mV}_{\text{Ag}/\text{AgCl}}$  can be indicative of SiO<sub>2</sub> dissolution. Further, the small amount of electrolyte from the micro-capillary tip in contact with surface can act as a confinement/crevice. It was demonstrated that Si can be vulnerable to corrosion in a confined amount of stagnant liquid (0.5 mm in electrolyte thickness), due to alkalization and particularly in the presence of phosphates (E. Ilic et al. [101]). This is discussed further in Chapter 3. Within a confined geometry, in this case the electrolyte droplet from the micro-capillary tip in contact with the interlayer, there is restricted ion mobility and diffusion of aggressive species from the WE surface. Oxygen reduction in this small amount of stagnate liquid results in the generation of OH<sup>-</sup>, and with restricted ion diffusion, the OH<sup>-</sup> species accumulate at the Si surface. This can result in local alkalization, and since Si is unstable at high pH, this would result in its dissociation (or corrosion). In addition, phosphorous species within Hyclone® WTF can complex to form soluble phosphorous-silicon complexes, as proposed by W. van Gelder [103] and by E. Ilic et al.

[101], resulting in further corrosion of the Si. To support this hypothesis of Si activation, the OCP evolution of bulk Si (from the sputter target) was characterized under the same microcapillary measurement conditions and is also shown in Fig. 2.11b (on the left y-axis). The OCP evolution of the bulk Si also experiences a continuous drop in potential, even more pronounced from ca.  $-400 \text{ mV}_{\text{Ag/AgCl}}$  to ca.  $-600 \text{ mV}_{\text{Ag/AgCl}}$ , indicating that the surface is also affected by oxide dissolution in HyClone WTF. The situation is however not as detrimental as in the case of the deposited Si interlayer because the higher initial OCP of the bulk Si indicates better passivation, and even at the final potential of  $-600 \text{ mV}_{\text{Ag/AgCl}}$  the surface is still not in active dissolution conditions. For this reason, monitoring the local OCP evolution over an extended period can serve as a good diagnostic for corrosion initiation susceptibility and growth, depending on the material of interest.

Fig. 2.12b shows the detrimental state of an initially wedge-milled Si interlayer after being immersed at freely corroding conditions (OCP) over an extended period. The initial state of a wedge-milled Ti/Si/DLC sample is shown in Fig. 2.12a (of the similar type as the one presented Fig. 4). Initially, the lateral width of the wedge-milled Si interlayer is  $60 \mu\text{m}$  (the deposited thickness is  $60 \text{ nm}$ ). After immersing the sample in HyClone® WTF at room temperature for ca. 1.5 years, the interlayer and adjacent DLC coating is degraded and. It can be seen that the Si interlayer has retracted (corroded) towards the DLC. There is no longer a smooth transition boundary at the Si/DLC interface, but rather a discontinuous delaminating DLC front can be seen. Delamination spots are also visible in the DLC coating, likely due to local defects that were initially present in this thinned region of the wedge-milled DLC. These corrosion attacks are analogous to the ones responsible for the failure case of a TiAlV/Si/DLC implant; after 4 years in the body, FIB cuts into the retrieved implant revealed that the  $60 \text{ nm}$  thick Si interlayer was missing at some locations [31,104].

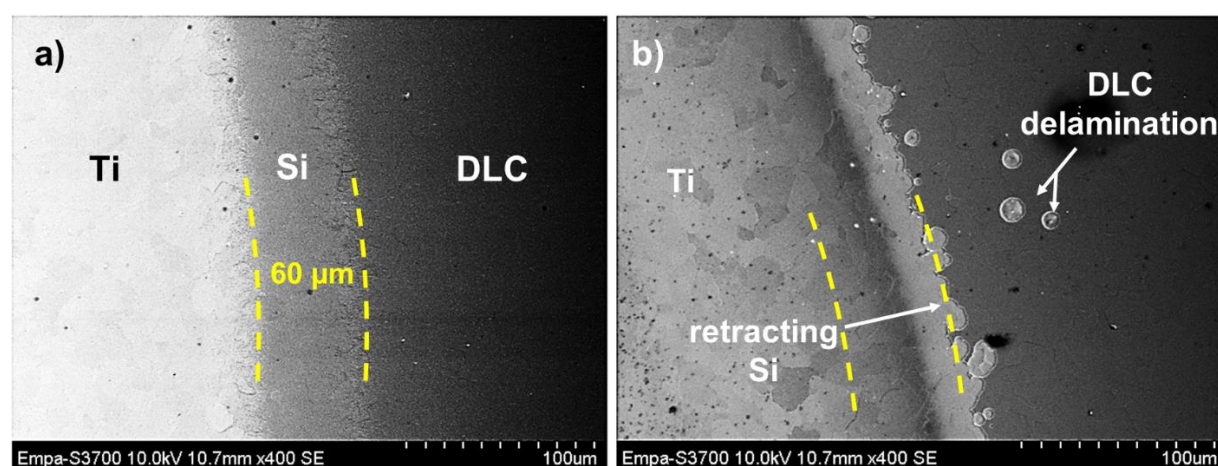


Fig. 2.12: a) SEM image of newly wedge-milled Ti/Si/DLC sample before immersion in HyClone® WTF, and, b) SEM image of the same sample after immersion in HyClone® WTF for 1.5 years, showing retracted (corroded) Si interlayer and adjacent DLC delamination front.

With the proposed methodology, the local-electrochemical measurements show that the Si interlayer corrosion susceptibility is responsible for the failure in the Ti/Si/DLC sample, as was confirmed by the long-term immersion experiment. On the other hand, Cr-C and Si-DLC are much more corrosion resistant interlayers.

In addition, the wedge-milling approach also allows for characterization of the different materials on the same-deposited sample. When solely utilizing macro-electrochemistry, the bare substrate, or the interlayer before DLC coating, is usually characterized first and used as a reference. This reference is then compared with the surface characterization of each deposited layer (substrate/interlayer and substrate/interlayer/coating). For this, different samples must be prepared in different deposition processes.

One aspect that the chapter is also highlighting is the importance of deposition parameters and conditions generating small differences in the interlayer/interfaces composition. With the carbide formation, new interface materials have to be considered. The aim of this work is not to obtain perfect interlayer materials, but to address with high laterally resolved methods the influence of small amounts of impurities on the corrosion susceptibility of these nm-thick new materials.

## 2.4 Chapter conclusions

This study presents a methodology for characterizing the chemical state composition and the corrosion susceptibility of buried interlayers/interfaces by combining; ionic wedge-milling of coated samples, compositional characterization of the interlayer/interfaces by Auger Electron Spectroscopy (AES), and utilization of a microcapillary technique for local-electrochemical assessment of the interlayer stability. The following can be concluded from the experimental observations:

- Macro-electrochemical potentiodynamic polarization measurements of DLC coated sample surfaces vary considerably depending on the underlying material and the extent/distribution of coating defects. Local-electrochemical measurements (four orders of magnitude smaller exposed areas) are more representative of the intrinsic behavior of the coating, such as DLC, showing nearly identical electrochemical reactivity regardless of the underlying material.
- Ionic wedge milling of a coated sample (substrate/interlayer/coating) allowed for exposure of the buried interlayer and its corresponding interfaces. An interlayer could be exposed laterally over 1000 times compared to its deposited thickness to make subsequent composition and electrochemical characterization much more accurate.
- The chemical composition of the interlayers and interfaces could be resolved, at least semi-quantitatively, with AES by collecting spectra from a multipoint-linescan across the wedge-milled samples. Carbides could be identified at the interfaces by performing detailed chemical binding identification with the Auger lines and by assigning peak shapes to reference spectra from known compounds. The observed susceptibility to carbide formation

is in line with the thermodynamic formation energy; Co is present as pure metal, whereas a Cr interlayer contains the most carbon.

- Local microcapillary electrochemical measurements allowed for characterization of the corrosion susceptibility of the wedge-milled interlayers, in reference to the substrate and DLC coating electrochemical response, characterized on the same deposited sample. Cr-carbide and Si-DLC (deposited from TMS) showed to be corrosion resistant interlayer materials in both OCP and potentiodynamic polarization experiments.
- Si interlayer showed electrochemical instability over extended freely corroding (at OCP) conditions, analogous to a long-term immersion experiment and failed TiAlV/Si/DLC implants.

In general, the presented methodology based on laterally resolved techniques can be used in combination with macro-electrochemistry to obtain corrosion susceptibility information of any buried interlayer with unknown electrochemical reactivity, and to determine the intrinsic degradation mechanisms of a coating and interlayer by excluding coating defects from the measured area.







## Chapter 3 Corrosion of silicon in confined and crevice environments

*The contents of this chapter are reproduced with permission from the published article [101]:*

### **Silicon Corrosion in Neutral Media: The Influence of Confined Geometries and Crevice Corrosion in Simulated Physiological Solutions**

*Emilija Ilic<sup>1,2</sup>, Ainhoa Pardo<sup>1</sup>, R. Hauert<sup>1</sup>, Patrik Schmutz<sup>1</sup> and Stefano Mischler<sup>2</sup>*

<sup>1</sup> Empa, Swiss Federal Laboratories for Materials Science and Technology, Laboratory for Joining Technologies and Corrosion, Switzerland

<sup>2</sup> EPFL, Ecole Polytechnique Fédérale de Lausanne, Tribology and Interfacial Chemistry Group, Switzerland

*Journal of the Electrochemical Society (2019)*

*Volume 166, Issue 6, pages C125-C133*

*doi:10.1149/2.0241906jes*

*© The Authors 2019. Published by ECS.*

**Contributions of E.Ilic:** *Performed sample preparation, experimental work, characterization, and data analysis. Formulated key ideas and discussion points, and wrote the manuscript.*

### 3.1 Chapter overview

In this chapter, a thorough investigation of the corrosion behavior of Si in crevices and confined geometrical environments is presented, using a model geometry and electrochemical cells to analyze the different key parameters (temperature, ionic species, pH evolution, applied potential, material conductivity/doping) controlling the degradation mechanisms. Initiation and dissolution kinetics have been assessed by a combination of long-term and temperature accelerated immersion tests in physiological simulating solutions, along with complementary electrochemical and pH measurements. The findings presented can provide insight into the degradation mechanisms responsible for the failure of Si in the body, whether as it relates to coating adhesion interlayers or electronic sensors. With this, better predictions of the lifetime and durability of implantable components and Si-based interlayers can be made, and the presented methodologies can as well be applied to any surface degradation process of interest.

### 3.2 Chapter specific introduction

#### 3.2.1 Si stability in physiological environments

Si is normally considered as bioinert and has very good adhesive properties, therefore it has been used as an interlayer material in coated orthopedic implants [46,105]. However it has a much broader application in neuroprosthetics, where Si based micro-electronic devices are providing new opportunities for the fabrication cochlear, retina and spinal implants, for treating neurological deficits [106,107]. As with most implantable devices however, problems arise when trying to simulate the long-term in-vivo environment during in-vitro testing. There are hence reported instances of Si-based implants corroding in the body or in animal hosts, despite successful in-vitro testing [108]. For example, DLC coated Ti6Al4V femoral heads, containing a Si adhesion promoting interlayer, were expected to increase the lifetime of hip implants. In reality, many failed after only a few years of implantation [29]. Focused ion beam (FIB) cuts into the failed hip explant from Fig. 1.1, revealed that the Si interlayer (original thickness of ca. 70–100 nm) had almost completely dissolved at some areas, as shown in Fig. 3.1.

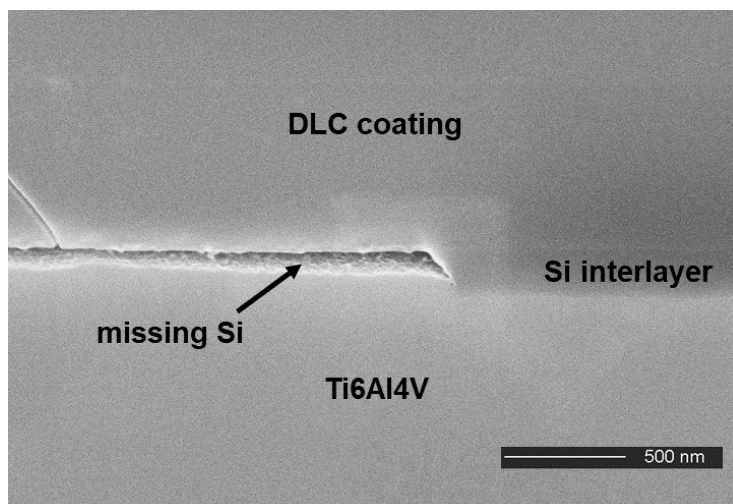


*Fig. 3.1: FIB cross-section of explanted DLC coated Ti6Al4V femoral head. Si interlayer has dissolved away.*

Platinum (Pt) coated Si microelectrode arrays, for neuroprosthetic applications, showed delamination of the Pt and signs of pitting corrosion on the underlying Si after 994 days in-vivo [109]. Severe corrosion of Si retinal chips was observed after 6 months of implantation in a rabbit, even though no significant damage occurred during in-vitro testing with immersion in phosphate buffered saline (PBS) solution for up to 21 months [110]. Similarly, large dissolution rates of up to  $18 \mu\text{m}/\text{year}$  (ca.  $2 \text{ nm}/\text{h}$ ) were recorded on polished Si pieces after one year of implantation in an animal host [111]. In some instances, protective coatings were used on Si substrates to suppress corrosion, but they turned out to be ineffective. For example, Si carbide (SiC) and DLC coatings showed poor protection of the underlying Si in saline solutions [112]. The in-vivo environment further promoted dissolution of Si oxide and Si nitride/oxy-nitride films, leaving the substrate exposed [113,114].

From a thermodynamic perspective (Pourbaix diagram [102]), Si is stable in the acidic to weakly alkaline domain, as seen in Fig. 3.2, due to the formation of a protective Si dioxide ( $\text{SiO}_2$ ) film ca.  $1 \text{ nm}$  in thickness on its surface. Si is mainly known to be unstable in very alkaline solutions (ca.  $\text{pH} > 10$ ) due to complexation with hydroxides ( $\text{OH}^-$ ), and in the presence of fluoride ( $\text{F}^-$ ). For these reasons, in micromachining application, Si is mostly etched in strongly alkaline media or hydrofluoric acid-based solutions. In physiological solutions (ca.  $\text{pH} 7.4$ ), Si is expected to passivate (formation of a nm-thick oxide layer), given the electrolyte/surface potential is kept in the stability regime of  $\text{SiO}_2$ , approximately above  $-0.8 \text{ V}_{\text{SHE}}$ . These stability conditions are extrapolated from the standard Si- $\text{H}_2\text{O}$

system at 25°C and do not account for the presence of specific body ions, proteins, and body temperature (37°C).

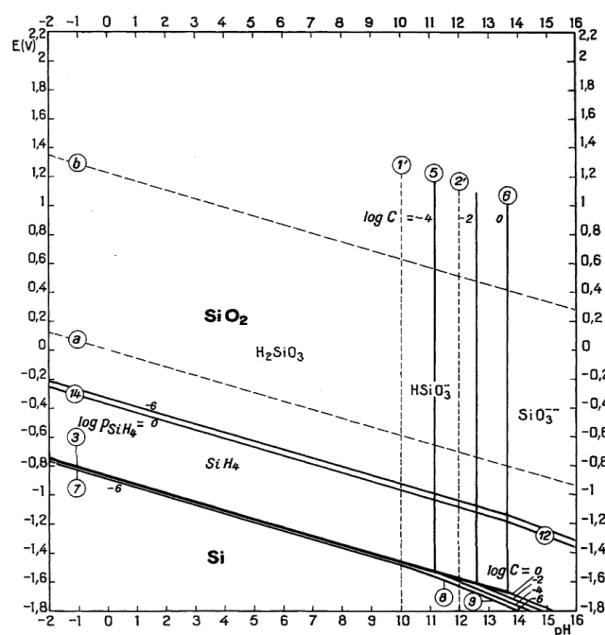


Fig. 3.2: Pourbaix diagram for the silicon-water system at 25 °C [102].

A key parameter often overlooked when assessing Si stability in-vitro, is the added geometrical constraints generated through in-vivo implantation. A Si component wedged between body tissues will behave differently than a wafer piece immersed in bulk physiological simulating solution, hence the two conditions cannot accurately be compared. In-vivo, a degradation induced local pH change may occur in areas confined by surrounding body tissue, resulting in pitting and crevice corrosion attack of the implanted material. A similar statement can be made for Si as an interlayer; the thin interlayer is confined between the coating and substrate, and miniature defects in the coating can allow surrounding body fluid to contact the interlayer, forming an electrochemical crevice cell. In addition, electrochemical galvanic coupling can occur between the substrate and interlayer. Hence, it is important to assess the susceptibility of Si to pitting and aggravated crevice corrosion, before real implantable devices are used in-vivo.

### 3.2.2 Electrochemistry of semiconductors

The electrochemical properties at a semiconductor/electrolyte interface differ from that of a metal/electrolyte interface. In order for a material to be conductive, electrons must move through it and occupy partially filled orbitals (i.e. the conduction band) [115]. The difference in energies between the conduction band ( $E_c$ ) and the valence band ( $E_v$ ) of a material is termed the band gap. For metals, the conduction band and the valence band overlap, so electrons can flow freely and are easily taken up by reduction reactions at the electrode/electrolyte interface. Insulators have large band gaps, and electrons cannot cross into the conduction band, therefore these materials have very good corrosion resistance, due to the unavailability of electrons for reduction reactions. In a

semiconductor, the band gap is not as big, and electrons have the possibility to move into the conduction band. For a semiconductor, the promotion of electrons into the conduction band can be achieved by thermal excitation, photochemically, or by doping [115]. Doping involves introducing additional elements into the semiconductor, usually elements from groups IV (e.g. phosphorus) and III (e.g. boron) in the periodic table. For example, when Si (consists of four valence electrons) is doped with phosphorus (consists of five valence electrons) the additional unbounded electron can move, increasing the conductivity of the semiconductor (referred to as n-type doping). This introduces electron occupied energy levels in the band gap close to the conduction band; electrons can hence be promoted easier into the conduction band [115,116]. Introducing boron (consists of three valence electrons) into a Si wafer results in the generation of mobile holes, which also increase the conductivity (referred to as p-type doping). This introduces vacant energy levels within the band gap close to the valence band, allowing promotion of electrons from the valence band. When a semiconductor is placed in contact with an electrolyte, the fermi level of the semiconductor and the redox potential of the solution want to lie at the same energy, and hence there is a movement of charge in order for these two phases to equilibrate [115,116]. For a p-type semiconductor at OCP, the fermi level is normally lower than the redox potential, and therefore electrons move from solution to the semiconductor to attain equilibrium, resulting in a negative charge in the space charge region of the semiconductor, causing downward bending of the band edges. The direction and extent of band bending depends on the applied potential placed on the electrode [115]. Considering a p-type semi-conductor, the following situations can occur: i) at a certain potential where the fermi level and solution redox potential align, there is no band bending, and this potential is hence referred to as the *flatband potential* ( $E_{fb}$ ), as shown in Fig. 3.3a, ii) if the applied potential is more negative than  $E_{fb}$ , downward band bending occurs, resulting in a carrier depletion region (Fig. 3.3b), iii) if the applied potential is more positive than the  $E_{fb}$ , a carrier accumulation region occurs (Fig. 3.3c)[115]. If there is an accumulation region, or if the depletion layer is very thin, the semiconductor behaves similarly to a metal electrode at an electrolyte interface [116].

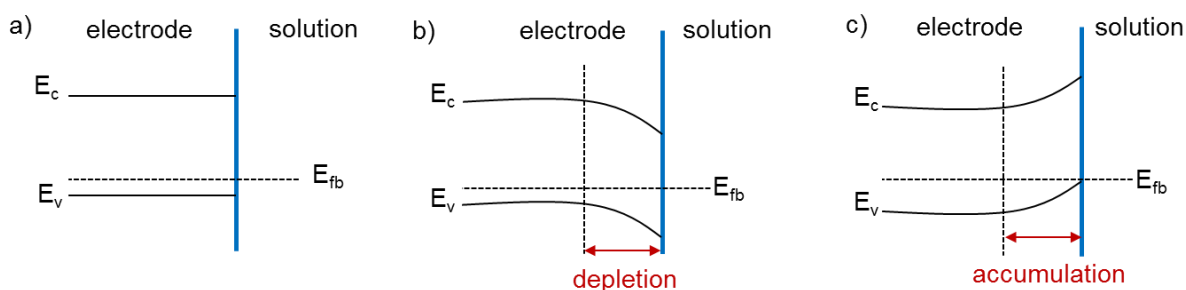


Fig. 3.3: Influence of an applied potential ( $E$ ) on the band bending behavior of a p-type semiconductor at an electrolyte interface: a)  $E = E_{fb}$ , b)  $E < E_{fb}$ , c)  $E > E_{fb}$  [115].

In the following study, highly doped, very conductive Si (p-type, 1-30  $\Omega\cdot\text{cm}$ ) is used, so that the charge transfer mechanism at the electrolyte interface is assumed to be similar to a passive metal. However, more detailed investigations on the semiconductor properties of the Si (eg. generation of Mott–Schottky plots) should be conducted in future work.

### 3.3 Experimental

#### 3.3.1 Samples and solutions

Boron (B) doped polished Si (p-type, 1-30  $\Omega\cdot\text{cm}$ ) wafer pieces with a thickness of ca. 0.5 mm and with a (100) crystal orientation, were cleaned by ultrasonic bath in ethanol and dried under argon flow. Corrosion experiments were performed in two different physiological simulating solutions: 0.01 M phosphate buffered saline (PBS, Sigma Aldrich) of pH 7.4, and HyClone® Wear Testing Fluid (HyClone® WTF, Thermo-Scientific) of pH 7.4–7.7. PBS has a relatively simple formulation, containing 0.137 M NaCl, 0.0027 M KCl, 0.01 M  $\text{Na}_2\text{HPO}_4$  and 0.0018 M  $\text{KH}_2\text{PO}_4$ . HyClone® WTF is bovine serum-based and is designed to simulate human synovial fluid by containing all the relevant body ions (phosphate, chloride, etc.) and 30 g/L of proteins.

#### 3.3.2 Immersion experiments

Long-term crevice and bulk solution immersion experiments were performed in 0.01 M PBS and HyClone® WTF. Using a polyoxymethylene (POM) clamping device, two Si wafer pieces (10 × 10 mm and 20 × 20 mm dimensions) were clamped together (as sketched in Fig. 3.6a in the initial situation) to form a simple *confined/crevice* cell (denoted Si|Si) and immersed in 100 mL of 0.01 M PBS or HyClone® WTF. Throughout the chapter, the term *crevice* will be used to describe the tight space between two clamped counterparts (maximum a few microns in thickness), while the term *confinement* will be used to describe a slightly larger separation (ca. 0.5 mm), directly outside of the crevice or set by a spacer, as described in Fig. 3.6a. A droplet of the respective solution was placed between the wafer pieces before clamping to ensure the presence of electrolyte inside the crevice area. In order to compare the degradation mechanisms with the situation in bulk solution, single Si wafer pieces were also immersed in 100 mL of each solution. After 35 days of immersion at room temperature (20°C) or 37°C, the samples were unclamped, ultrasonically cleaned in ultrapure water, and dried under argon for further ex-situ surface characterization. The influence of galvanic coupling as an aggravating factor was also assessed by performing the experiments with Si pieces (20 × 20 mm) clamped against Ti pieces (20 × 20 mm), denoted Si|Ti.

Accelerated immersion experiments were also performed by elevating the temperature and reducing the immersion time accordingly. In 0.01 M PBS, this was done at 50°C, 70°C and 90°C, for 240 h, 24 h, and 5 h, respectively. In HyClone® WTF, the experiments were only performed until 50°C in order to avoid substantial protein denaturation.

#### 3.3.3 Electrochemical Experiments

To obtain more detailed information about the Si destabilization mechanisms (initiation, active dissolution), in-situ characterization was implemented. Open circuit potential (OCP), electrochemical impedance spectroscopy (EIS), and electrochemical polarization measurements (potentiodynamic and potentiostatic) were conducted on Si in bulk electrolytes (0.01 M PBS, HyClone® WTF, 0.01 M NaCl, and NaOH pH 13 solution) with a PGSTAT30 potentiostat (Metrohm-

Autolab). A three electrode macro-electrochemical cell setup (Fig. 2.3) was used with an exposed Si working electrode (WE) area of 78 mm<sup>2</sup> and an electrolyte volume of 100 mL. A glass Luggin capillary was used as an electrolyte bridge with a 3 M Ag/AgCl reference electrode (RE, Metrohm), and the counter electrode was a platinum rod (CE, Metrohm). For the electrochemical polarization experiments, a scan rate of 1 mV/s was applied. For the EIS experiments, a perturbation voltage of 10 mV was applied over a frequency range of 10<sup>5</sup> Hz to 0.01 Hz.

For electrochemical characterization in small electrolyte volumes, a modification of the confined/crevice cell was designed to monitor the OCP of the Si surface at different locations in the confined area, as described in Fig. 3.4a. Two epoxy blocks with 4 POM screws were used as a clamping device and a 20 × 20 mm Si piece, acting as a WE, was contacted with a copper wire and imbedded into the bottom epoxy block. A 0.5 mm thick polypropylene (PP) spacer with a 10 × 15 mm central cut-out area was placed between the epoxy blocks before clamping, so that a small amount of electrolyte could access the confined area. A 3 M Ag/AgCl RE with an attached salt bridge (a plastic pipette tip filled with agar infused with 1 M NaCl) was inserted through a small hole ( $\varnothing$  = 1 mm) in the top block. A second RE-salt bridge assembly was placed outside of the cell at the confinement opening. With this RE configuration, the OCP could be monitored simultaneously inside and outside of the confined cell, using a multichannel zero-resistance ammeter (ZRA GalvoGill 12, ACM Instruments). The cell with electrodes was immersed in 100 mL of 0.01 M PBS or HyClone® WTF, contained within a double-walled glass vessel so that the temperature could be controlled.

Separate measurements were performed at 50°C, followed by 70°C in 0.01 M PBS, and at 37°C, followed by 50°C in HyClone® WTF, for 48 h at each temperature. The Si working electrodes were ground with 1000 Grit CarbiMet paper prior to cleaning in order to establish good electrical contact.

However before it could be applied to the unknown Si system, it first had to be demonstrated that the custom-made confined/crevice cell in Fig. 3.4a functioned properly with a known reference material. For this, a reference test was first made in which a Cr13-steel WE was used in 1 M NaCl electrolyte (pH 5) at room temperature. Cr13-steel is known to be susceptible to pitting and crevice corrosion in chloride-containing environments [117]. If a critical environment in the crevice cell is achieved, as was described via the mechanism in Fig. 1.3, local breakdown of the protective surface oxide on the steel would occur and result in corrosion of the steel. This would correspond to a drop in the OCP. This is indeed observed in the OCP evolution measurement in Fig. 3.5a. There was little difference between the OCP measured with the inner RE and outer RE, so only the OCP at the inner position is plotted. After ca. 3 h, a severe drop in potential occurs from ca. 150 mV<sub>AgAgCl</sub> to ca. -385 mV<sub>AgAgCl</sub>, after which the potential stays between -360 mV<sub>AgAgCl</sub> to -425 mV<sub>AgAgCl</sub>. At the initial potential of 150 mV<sub>AgAgCl</sub>, Fe-oxide (Fe<sub>2</sub>O<sub>3</sub>) and Cr-oxide (Cr<sub>2</sub>O<sub>3</sub>) is stable at pH 5 (as seen in the Fe-H<sub>2</sub>O and Cr-H<sub>2</sub>O Pourbaix diagrams [90,118]). In the -385 mV<sub>AgAgCl</sub> to -425 mV<sub>AgAgCl</sub> potential domain, dissolution of Fe<sub>2</sub>O<sub>3</sub> to Fe<sup>2+</sup> and Cr<sub>2</sub>O<sub>3</sub> to Cr<sup>2+</sup> predominates, resulting in corrosion of the steel surface. The corrosion could be visually seen when the crevice cell was opened after the experiment, as seen in Fig. 3.5b. Therefore, with confirmation of the reference test, the cell could now be applied to the case of Si.



In order to determine the pH inside of the confined/crevice cell configuration, the clamping device was slightly modified; a hole was drilled in the opposing epoxy clamp and filled with agar gel infiltrated with a pH indicator, as seen in Fig. 3.4b. Duplicate immersion experiments were performed with different pH indicators; one with phenolphthalein which turns pink above pH 8.5, and the other with thymolphthalein which turns blue above pH 10.

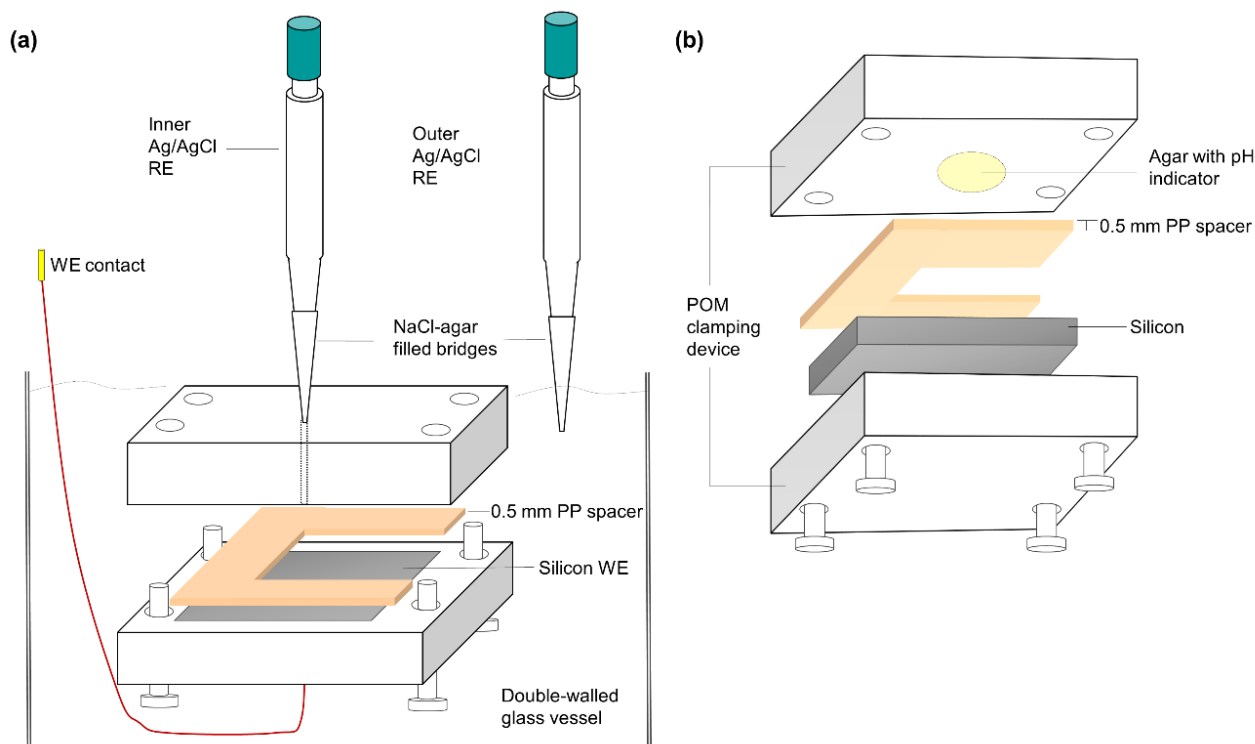


*Fig. 3.4: Schematic description of the confinement cell setup (referred as confined/crevice setup in the paper): (a) used for conducting electrochemical measurements, (b) modified cell used to determine pH evolution inside a confinement: agar is infiltrated with phenolphthalein (turns pink at pH 8.5-10), or thymolphthalein (turns blue above pH 10) pH indicator, and imbedded in the top clamp.*

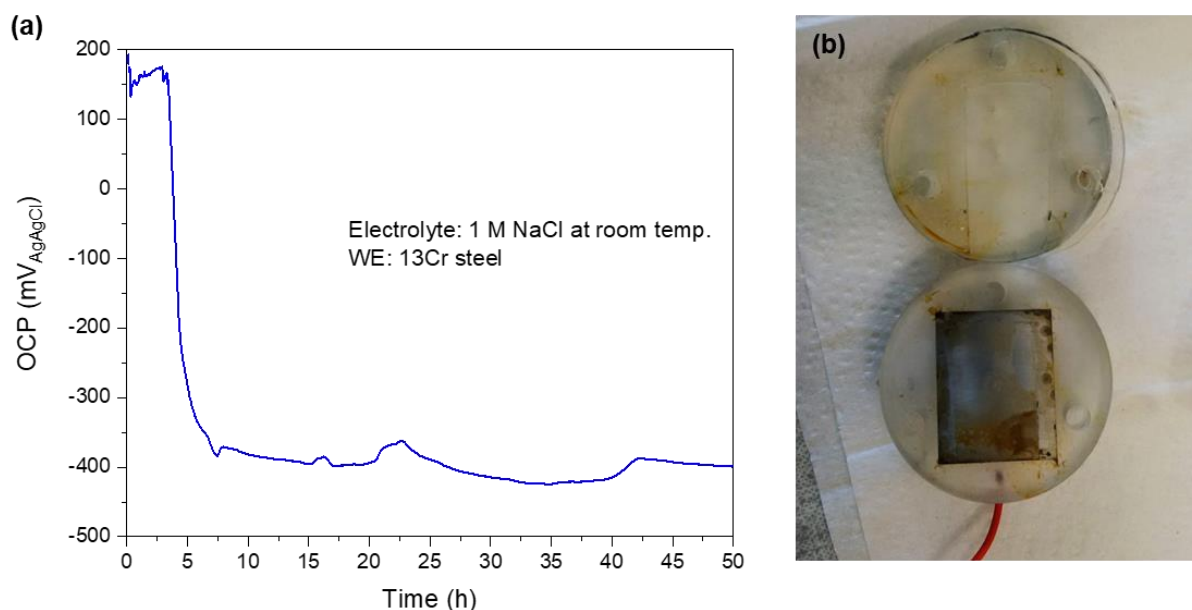


Fig. 3.5: Reference test of the confined/crevice cell from Fig. 3.4a; using 13Cr-steel as the WE and 1 M NaCl solution at room temperature as the electrolyte, the OCP evolution is recorded. b) Severe corrosion of the 13Cr-steel WE can be seen after the experiment.

### 3.3.4 Post immersion characterization

After immersion and cleaning treatment, the surfaces of the Si samples were inspected with a scanning electron microscope (SEM, Hitachi S-3700N). In order to quantify the magnitude of corrosive attack, surface profiles were taken over the wafer pieces with a DektakXT<sup>®</sup> stylus profiler (Bruker). The corroded vertical depth was determined by performing several line scans over each sample's surface, measuring the height of the step ( $\Delta h$ ) at the crevice/confinement boundary and taking an average value, denoted  $\Delta h_{\text{corr}}$ . The corrosion rate could be determined by dividing  $\Delta h_{\text{corr}}$  by the immersion time.

## 3.4 Results and Discussion

### 3.4.1 Long-term immersion experiments in physiological simulating conditions

The results of the long-term confined/crevice and bulk solution immersion experiments at 37°C exposure in physiological simulating solution are presented before different stress parameters (temperature, ionic concentration) are varied to establish a model for the active corrosion mechanism.

A schematic description of the initial (upon immersion) and resulting (after 35 days) situation of a Si|Si confined/crevice cell immersed in HyClone<sup>®</sup> WTF at 37°C is shown in Fig. 3.6a. After opening the crevice and cleaning the clamped counterparts, a SEM image was taken of the 20 × 20 mm Si wafer piece over the area containing the crevice mouth (indicated by "0"), as shown in Fig. 3.6b. Two distinct regions can be seen in the SEM image; one with severe pitting in the crevice area on

the left (indicated by "-" arrow), and another uniformly corroded area in the confinement on the right (indicated by "+" arrow). The two regions are separated by a prominent vertical step at the crevice mouth (at location "0"), better evidenced in Fig. 3.7. The distinct pyramidal shape of the pits is characteristic of anisotropic (crystallographic orientation-dependent) attack of the faster dissolving (100) and (110) planes, leaving the more stable (111) planes intact. This orientation-dependent dissolution behavior is known to occur in alkaline solutions, such as in KOH and NaOH [119], it is however usually not observed in media of pH 7.4–7.7. The topography after prolonged immersion has been characterized by 1 mm profilometer linescans across these two regions, one representative example is shown in Fig. 3.7. Indeed a very prominent vertical step can be seen at the crevice mouth where a maximum depth of ca. 3  $\mu\text{m}$  (corresponding to a dissolution rate of 3.6 nm/h) of Si has almost uniformly corroded away along the whole confined area. Throughout the paper, the corrosion rates in the confined area are calculated based on this maximum uniform dissolution height,  $\Delta h_{\text{corr}}$ , measured at the prominent step. Considering the shape of the profile in Fig. 3.7, and that the most severe damage occurs directly at the crevice mouth (0 mm), suggests that a galvanic coupling mechanism may be occurring between the electrochemical reactions directly outside in the confined space, balancing the localized corrosion attacks observed inside the crevice. The experiments of the next sections are designed to give more insight into this mechanism. In contrast to the confined/crevice cell immersion conditions, single wafer pieces immersed in bulk HyClone® WTF for an equal duration did not show any detectable damage.

Considering 0.01 M PBS, the immersion experiment at 37°C for 35 days showed neither visual nor quantifiably detectable damage, both in the case of the confined/crevice and single wafer samples. Some corrosion was detected however after a much longer immersion time of 157 days in the confined/crevice setup, after which  $\Delta h_{\text{corr}}$  was measured to be 170 nm.

HyClone® WTF is much more complex in composition than 0.01 M PBS and it is therefore difficult to identify exactly which components are contributing to its harsher influence on Si corrosion. One first hypothesis could be that the protein-containing solution is much more viscous and hence slows down ionic exchange and diffusion throughout the electrochemical cell.

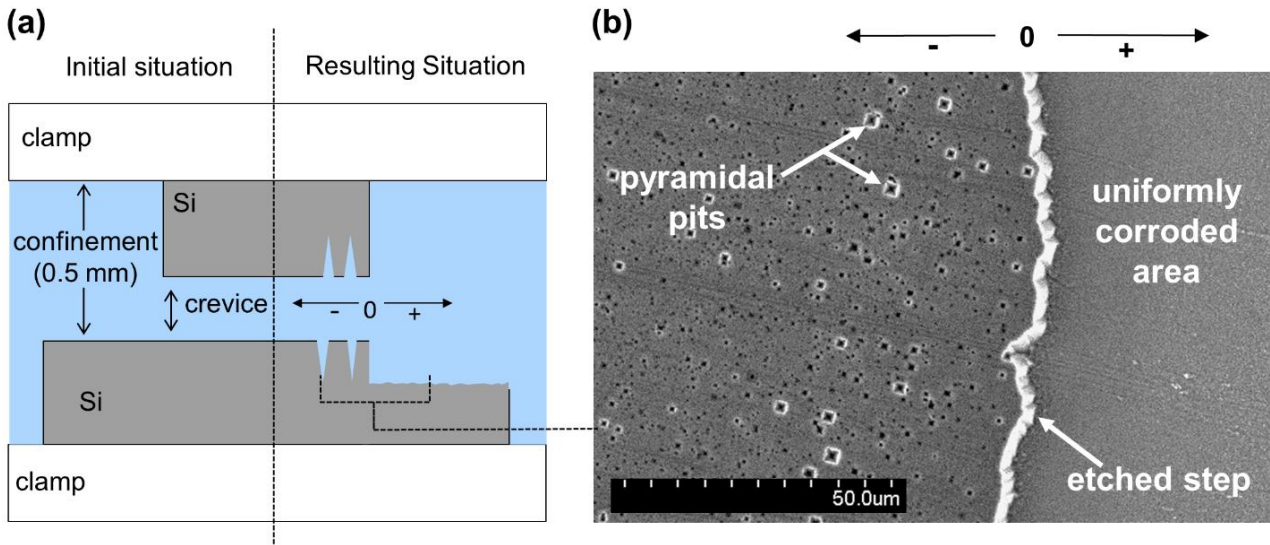


Fig. 3.6: (a) Schematic description (exaggerated for clarification) of the corrosion processes occurring in a Si|Si confined/crevice configuration showing the initial immersion situation, and the resulting situation after 35 days; at the crevice mouth (indicated by "0") a uniformly corroded area occurs to the right in the confinement ("+" arrow), while pits are found to the left inside the crevice ("-" arrow). (b) Resulting SEM image of the bottom Si wafer close to the vicinity of the crevice mouth; unclamped after 35 days in a HyClone® WTF containing crevice at 37°C. Pyramidal pits are present in the crevice area, and a distinct step occurs at the crevice mouth where the smaller opposing Si was clamped.

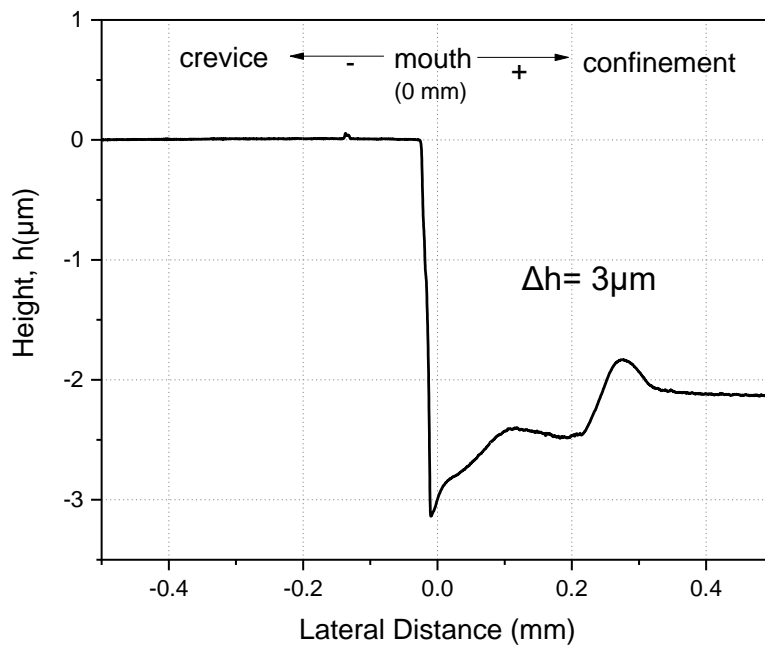


Fig. 3.7: A profilometer topography scan corresponding to Fig. 3.2b shows a significant corroded depth with a maximum of ca.  $3\mu\text{m}$  at the mouth (indicated at 0 mm) of the Si|Si confined/crevice area, after 35 days immersion in HyClone® at 37°C.

### 3.4.2 Accelerated immersion experiments in confined/crevice conditions

Following the corrosion investigation and processes observed at 37°C, temperature was used as a kinetic acceleration factor to investigate the passive oxide stability threshold and corrosion rates. The resulting corrosion rates of the accelerated Si|Si confined/crevice immersion experiments at elevated temperatures of 50 – 90°C are presented in an Arrhenius plot ( $\ln[\text{corrosion rate}]$  vs.  $1/T$ ) in Fig. 3.8 (represented by squares), along with the corrosion rates obtained at 20°C and 37°C. In 0.01 M PBS, the corrosion rates range from 5.4 – 416.7 nm/h for temperatures between 50 – 90°C, while in HyClone® WTF, measurable corrosion is already initiated at 20°C with corrosion rates of 0.4–13.8 nm/h. The dissolution mechanisms in both solutions yield a linear trend in the Arrhenius plot, suggesting that a single rate-limiting process is occurring, and that temperature does not alter the dissolution mechanism but only its rate. It has to be mentioned that the corrosion rates are determined assuming immediate corrosion initiation upon immersion and a constant dissolution rate throughout the whole immersion time. This approximation is certainly valid for higher temperature, whereas in the transition temperature range where passivation is still effective, initiation time and mechanisms need to be investigated with methods that are more sensitive. The immersion experiment performed in 0.01 M PBS at 37°C is a good example supporting the previous statement; the corrosion rate at 37°C was calculated considering a very long immersion duration of 157 days, but active corrosion was likely initiated later, long after the start of immersion. The delayed corrosion initiation explains why the measurement point falls off the Arrhenius trendline. It is a good example of how an in-vitro test performed for a shorter duration may provide misleading predictions of an implant's lifetime, given that the immersion experiment performed for 35 days showed no damage. Therefore, it would be incorrect to guarantee product stability at 37°C, since crevice corrosion can sometimes take many months, or even years, to initiate. When considering the corrosion process for a passivating material like Si, the initiation mechanism is key to understanding its corrosive failure. In the active corrosion domain, the obtained trendlines in Fig. 3.8 present nearly identical activation energies ( $E_a$ ), 106 KJ/mol in 0.01 M PBS and 109 KJ/mol in HyClone® WTF. The  $E_a$  for the dissolution of (100) oriented Si and SiO<sub>2</sub> varies greatly depending on the ionic species present in the solution. In alkaline solutions, the  $E_a$  for Si etching can vary between 38 – 63 KJ/mol and 77 – 87 KJ/mol for SiO<sub>2</sub>, depending on the solution concentration [120]. Van Gelder found activation energies of 110 KJ/mol and 115 KJ/mol, for Si and SiO<sub>2</sub>, respectively, etched in phosphorous acid (H<sub>3</sub>PO<sub>4</sub>) [103]. It was suggested that a soluble phosphorous-silicon complex may form, resulting in dissolution of the Si oxide and the substrate. Considering the similar activation energies obtained in this study, the phosphorous species present in PBS and HyClone® WTF may contribute to similar phosphorous-silicon complex formation when confined in a small amount of stagnant liquid. To validate this hypothesis, additional experiments were performed to assess the influence that phosphates have on the degradation of Si, and these are presented in the next section.

The influence of galvanic coupling was also assessed by clamping Si against Ti counterparts (Si|Ti). The corrosion rates of these experiments are also plotted in Fig. 3.8 (represented by circles). It can be seen that in both electrolytes slightly higher Si corrosion rates are attained when Ti is used as the

clamped counterpart, however the effect is more prominent in PBS. The OCPs of Si and Ti were measured to be  $-750 \text{ mV}_{\text{Ag}/\text{AgCl}}$  and  $-350 \text{ mV}_{\text{Ag}/\text{AgCl}}$ , respectively, in Hyclone® WTF, as measured by the 24 h microcapillary experiments from section 2.3.4. The small amount of electrolyte from the microcapillary tip in contact with the Si surface can also act as a confinement. Given the difference in potentials, with the passive Ti being the nobler component, a galvanic couple is indeed expected when the two materials are placed in contact. Therefore, galvanic coupling between the substrate and the interlayer is an additional aggravating factor that can increase the Si dissolution rate when the substrate is exposed to the aggressive media at defects, such as in the TiAlV/Si/DLC implant case.

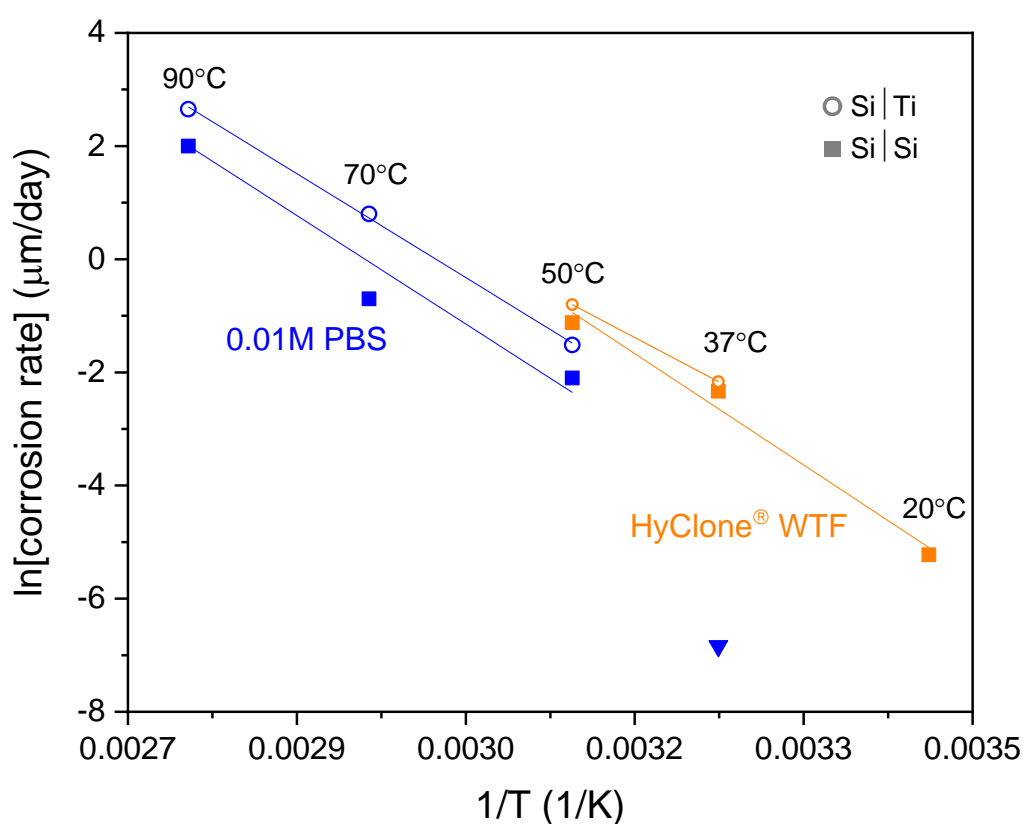


Fig. 3.8: Arrhenius plot demonstrating a linear active Si dissolution mechanism in 0.01 M PBS and HyClone® WTF measured in the confined area.

### 3.4.3 Influence of phosphorous species

While HyClone® WTF contains proteins and phosphates but is complex in composition, 0.01 M PBS is a relatively simple solution as it contains only potassium, sodium, chloride, and phosphate compounds. The influence each of these ionic species has on the dissolution of Si and its oxide could be investigated by performing accelerated Si|Si confined/crevice immersion experiments in solutions of various salts (Solutions 1–2, and 4–6, in Table 3.1). The experiments were performed with two different solution concentrations (0.01 M and 0.1 M) for 2 h of immersion at 90°C. The measured corrosion rates, determined by means of profilometer linescans ( $\Delta h_{\text{corr}}$ ) are presented in

Table 3.1. Increasing the concentrations of the dibasic phosphate compounds ( $\text{K}_2\text{HPO}_4$  and  $\text{Na}_2\text{HPO}_4$ ) in Solutions 4 and 5 drastically increased the Si corrosion rates. On the other hand, with the monobasic phosphate compounds ( $\text{KH}_2\text{PO}_4$  and  $\text{NaH}_2\text{PO}_4$ ) of Solutions 1 and 2, no corrosion was detected (–) regardless of concentration. The difference lies in the type of phosphate ion that predominates in each solution, which can be determined by a speciation diagram (% of species vs. pH) [121]. The dihydrogen phosphate ion ( $\text{H}_2\text{PO}_4^-$ ) is weakly acidic and predominates in Solutions 1 and 2, while the hydrogen phosphate ion ( $\text{HPO}_4^{2-}$ ) is weakly alkaline and predominates in Solutions 4 and 5 (see Table 3.1). In 0.01 M PBS, at pH 7.4, the amount of phosphate species are 39%  $\text{H}_2\text{PO}_4^-$  and 61%  $\text{HPO}_4^{2-}$ . Hence, it appears that the corrosion rate of Si is ultimately enhanced by increasing the alkaline  $\text{HPO}_4^{2-}$  species in solution. In chloride-containing solution, corrosion was not detected or was much less drastic. Even when chloride-containing solutions were made alkaline by the addition of NaOH, the Si corrosion rates were still much lower than in the phosphate-containing solutions of equal pH, as seen in Fig. 3.9. These observations indicate that phosphorous-silicon complex formation is a key accelerating factor in the destabilization and corrosion initiation of passivated Si in neutral to slightly alkaline solutions. Si-hydroxide complex formation is then known to be responsible for the dissolution of Si in the more alkaline solutions. Little research has been published on the interaction between phosphate species and Si but given the results presented in this study, a soluble phosphorous-silicon complex as proposed by W. van Gelder [103], may indeed be the factor controlling oxide film destabilization and active Si dissolution.

Table 3.1: Corrosion rates of Si|Si confined/crevices in different solutions at 90°C. (–) refers to no corrosion detected.

| Solution<br>Nr. | Content                   | Concentration<br>(M) | % $\text{H}_2\text{PO}_4^-$ /<br>% $\text{HPO}_4^{2-}$ | pH  | Corrosion rate<br>(nm/h) |
|-----------------|---------------------------|----------------------|--|-----|--------------------------|
| 1               | $\text{KH}_2\text{PO}_4$  | 0.01<br>0.1          | 99 / 1   | 5   | –                        |
| 2               | $\text{NaH}_2\text{PO}_4$ | 0.01<br>0.1          | 99 / 1   | 5   | –                        |
| 3               | PBS                       | 0.01                 | 39 / 61  | 7.4 | 19                       |
| 4               | $\text{K}_2\text{HPO}_4$  | 0.01<br>0.1          | 5 / 95   | 8.5 | 358<br>1182              |
| 5               | $\text{Na}_2\text{HPO}_4$ | 0.01<br>0.1          | 5 / 95   | 8.5 | 105<br>830               |
| 6               | $\text{NaCl}$             | 0.01<br>0.1          | 0/0  | 5.5 | –                        |

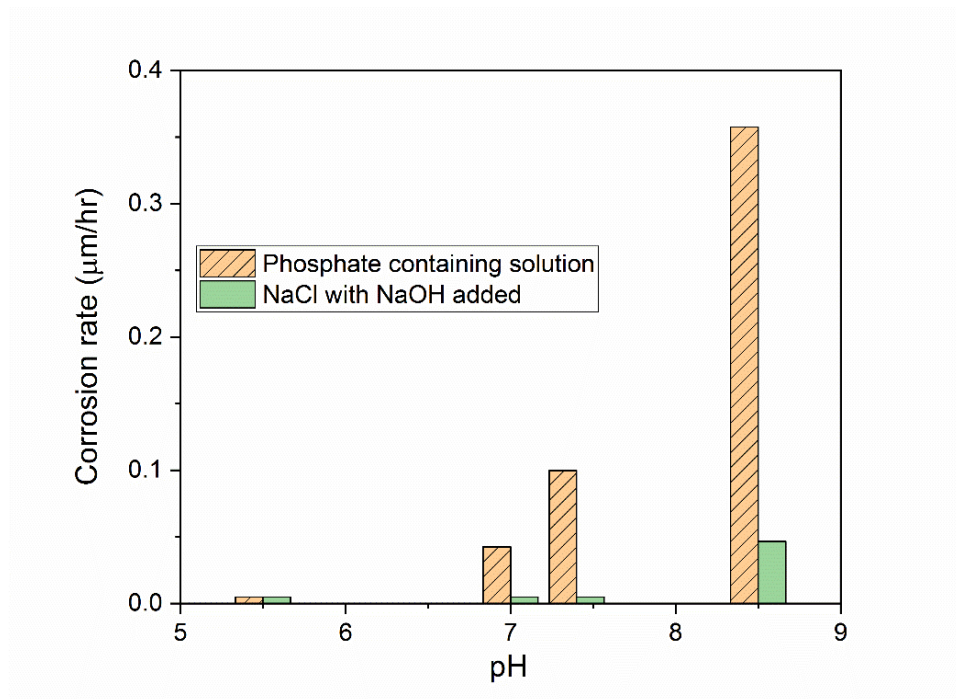


Fig. 3.9: Corrosion rates of Si at the confined area when immersed in NaCl and phosphate-containing crevices ( $K_2HPO_4$ ,  $Na_2HPO_4$ , PBS) at 90°C for 2 h. For NaCl solutions, pH was initially adjusted by NaOH addition.

#### 3.4.4 Electrochemical characterization of Si passive film stability

To investigate the stability of Si oxide, and how it relates to corrosion initiation, macro-electrochemical characterization of the potential and current evolution as a function of the immersion conditions (solution, time, and temperature) was performed. Fig. 3.10 presents the potentiodynamic polarization measurement for Si immersed in bulk 0.01 M PBS and HyClone® WTF at 37°C and selected higher temperatures. The polarization measurements obtained for Si immersed in 0.01 M NaCl (pH 5) and NaOH (pH 13) at 37°C are included to demonstrate the passive oxide stability boundary domain; from very protective at pH 5 to active dissolution at pH 13. It can be seen that a kinetic reaction equilibria between oxygen reduction and Si oxidation in the very stable passive surface condition induces nobler (more positive) corrosion potentials ( $E_{corr}$ ) and lower corrosion current densities ( $i_{corr}$ ), for Si immersed in NaCl solution and 0.01 M PBS at 37°C. With increasing pH or temperature, the passive Si-oxides in contact with HyClone® WTF and 0.01 M PBS progressively become unstable, as evidenced by a negatively shifting  $E_{corr}$  and increasing  $i_{corr}$ . Small active-passive transitions in the current curves also start to be observed upon polarization. In NaOH, a very active  $E_{corr}$  of ca.  $-1.2 V_{Ag/AgCl}$  indicates complete destabilization of Si-oxide in this media with active dissolution, as expected from the absence of thermodynamically stable phases (Pourbaix diagram [102]). Anodic potentiodynamic polarization however evidences that Si, even in very alkaline pH 13 solution, does not show very high active dissolution current densities. The maximum current density of ca.  $10^{-4} A/cm^2$  can be explained by hindered active dissolution related to the formation of poorly soluble Si-complexes (oxi-hydroxides) on the Si surface. Formation of these intermediate products can explain why the Si surface does not remain active and re-passivates when



polarizing away from the  $E_{\text{corr}}$ . This very subtle difference in the surface oxide film stability is demonstrated by the presence of a plateau in the curve upon anodic polarization in pH 13 but with a quite high current density ( $> 10^{-5} \text{ A/cm}^2$ ), indicating the defective nature of the formed film (referred to as pseudo-passivation).

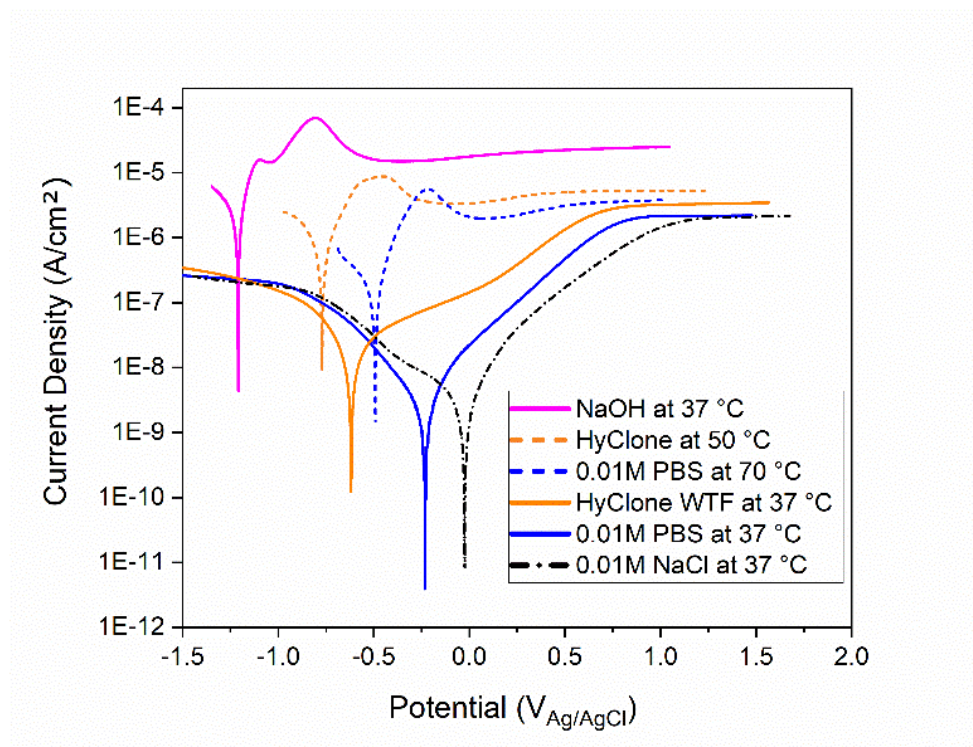


Fig. 3.10: Anodic polarization measurements of Si at different temperatures in bulk solutions: 0.01 M NaCl (pH 5), 0.01 M PBS (pH 7.4), HyClone® WTF (pH 7.4-7.7), and NaOH (pH 13).

To better evidence this critical transition from soluble Si-complex formation inducing a decrease in active dissolution, to pseudo-passive oxide formation on the Si surface upon small anodic polarization, potentiostatic polarization experiments were performed in the pH 13 solution around the polarization potentials where the active-passive current transition domain is observed. Indeed, very different current evolution behaviors are recorded when varying the applied potential between  $-1 \text{ V}_{\text{Ag/AgCl}}$  and  $-0.8 \text{ V}_{\text{Ag/AgCl}}$ , as seen by the measurements presented in Fig. 3.11. The oxide stabilizes with a steady current decrease when the potential is held at  $-0.8 \text{ V}_{\text{Ag/AgCl}}$ , whereas it stays activated (constant higher current) at lower potentials closer to the free corrosion potential,  $E_{\text{corr}}$ . These observations point to a surface oxide that is very sensitive to its chemical environment and is easily stabilized by anodic polarization.

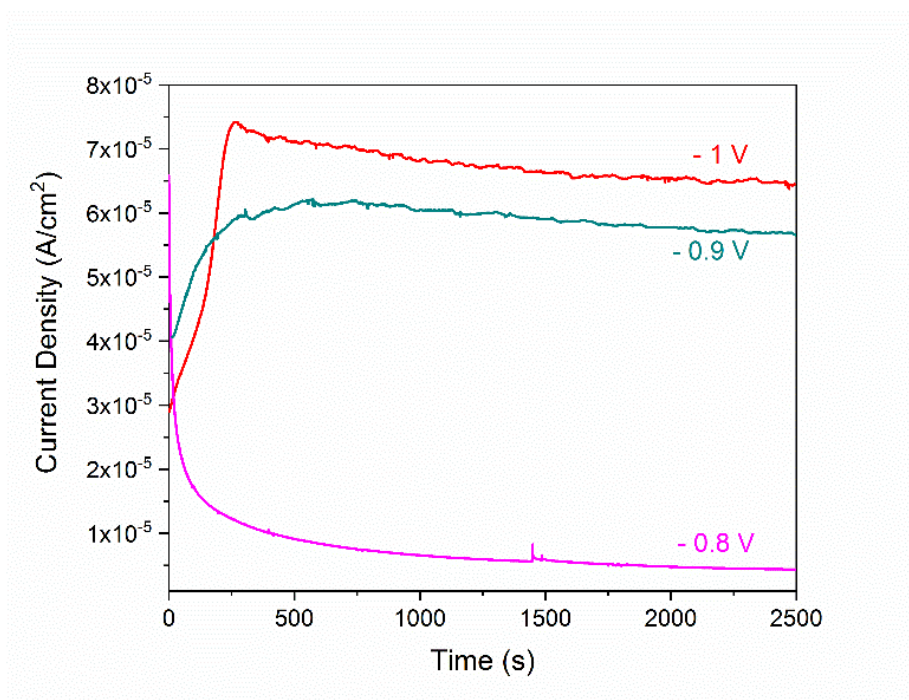


Fig. 3.11: Potentiostatic polarization measurements of Si in bulk NaOH, pH 13. Influence of applied potential on the passivation behavior.

Electrochemical impedance spectroscopy (EIS) was also performed to investigate the reaction phenomena occurring at the Si/electrolyte interface during the active-pseudo passive transition domain. The corrosion process can involve several reactions from purely active dissolution to passivation, or pseudo-passivation due to the formation of intermediate corrosion products associated with adsorbed species on the electrode's surface. Since anodic potentiodynamic polarization drives the corroding interface far from equilibrium (usually the condition of interest), this method does not give much mechanistic information about the different phenomena occurring at the electrode/electrolyte interface. Whereas the EIS technique applies a very small voltage perturbation (ca. 10 mV) around the OCP, or a set potential, and the current response as a function of frequency is recorded. Multiple reactions occurring in parallel can then be distinguished.

The Nyquist plot (imaginary,  $Z''$ , vs. real,  $Z'$ , impedance) of the Si immersed in NaOH (pH 13) system is presented in Fig. 3.12. An actively corroding electrode (a charge transfer reaction) yields a semi-circle in the complex plane. Intermediate reactions occurring during the dissolution process however modify the semi-circle. For example, inductive behavior arising from adsorbed intermediate species on the electrode's surface results in a positive  $Z''$  value, falling below the real axis in the Nyquist plot. Hindered dissolution through poorly soluble corrosion products can induce a negative impedance (due to a decreasing current response with increasing applied voltage). In the Nyquist plot, this *negative resistance* effect is evidenced by a semi-circle that reverts to negative values on the real axis. In the EIS measurements of Fig. 3.12, a 10 mV perturbation was applied around each of the potentials indicated in the potentiostatic measurements of Fig. 3.11 (-1V, -0.9V, -0.8V) and around the OCP. Therefore, at each potential one Nyquist curve is obtained. At OCP, a

depressed semi-circle with relatively low impedance values is characteristic of slow active dissolution of Si. With slight anodic polarization to  $-1 \text{ V}_{\text{Ag}/\text{AgCl}}$  and  $-0.9 \text{ V}_{\text{Ag}/\text{AgCl}}$ , the impedance exhibits very different behavior. The semi-circles are depressed to even lower impedance values, indicating an acceleration of the dissolution compared to the OCP behavior. However, a reverting of the semi-circle to negative impedance (more pronounced at  $-0.9 \text{ V}$ ) also occurs, and is associated with the adsorption of intermediates, likely  $\text{OH}^-$  ions, on the Si surface. Therefore, Si dissolution and formation of intermediate products are both occurring at  $-1 \text{ V}_{\text{Ag}/\text{AgCl}}$  and  $-0.9 \text{ V}_{\text{Ag}/\text{AgCl}}$ . At  $-0.8 \text{ V}_{\text{Ag}/\text{AgCl}}$ , analogously to the potentiostatic curve from Fig. 3.11, a pseudo-passivation state is achieved due to the hindrance of direct active Si dissolution by the stabilization of the surface product layer, evidenced by increasing impedance values (a larger semi-circle). This behavior can be compared to the passivation of iron in sulfuric acid, which is not thermodynamically driven (as seen in Fe Pourbaix diagram at low pH), but relies on the stabilization of corrosion products.

The measurement sequence further shows how electrochemical polarization can bias the corrosion mechanism of the Si system by stabilizing adsorbed corrosion products and inducing pseudo-passivation, even in highly corrosive NaOH media. The Si dissolution is strongly influenced by the formation of intermediates (corrosion products) and for this reason no real active and fast dissolution kinetics are obtained, even in very alkaline media. In order to avoid biasing through polarization, monitoring the evolution of the free corrosion potential (OCP) provides a better diagnostic for the surface oxide stability and corrosion susceptibility. Large variations in the measured OCP can be expected depending on the degree of surface stability, from low values (ca.  $-1.2 \text{ V}_{\text{Ag}/\text{AgCl}}$  in the active state) to high potentials related to the presence of a stable Si-oxide, as identified by the electrochemical polarizations in physiological solutions.

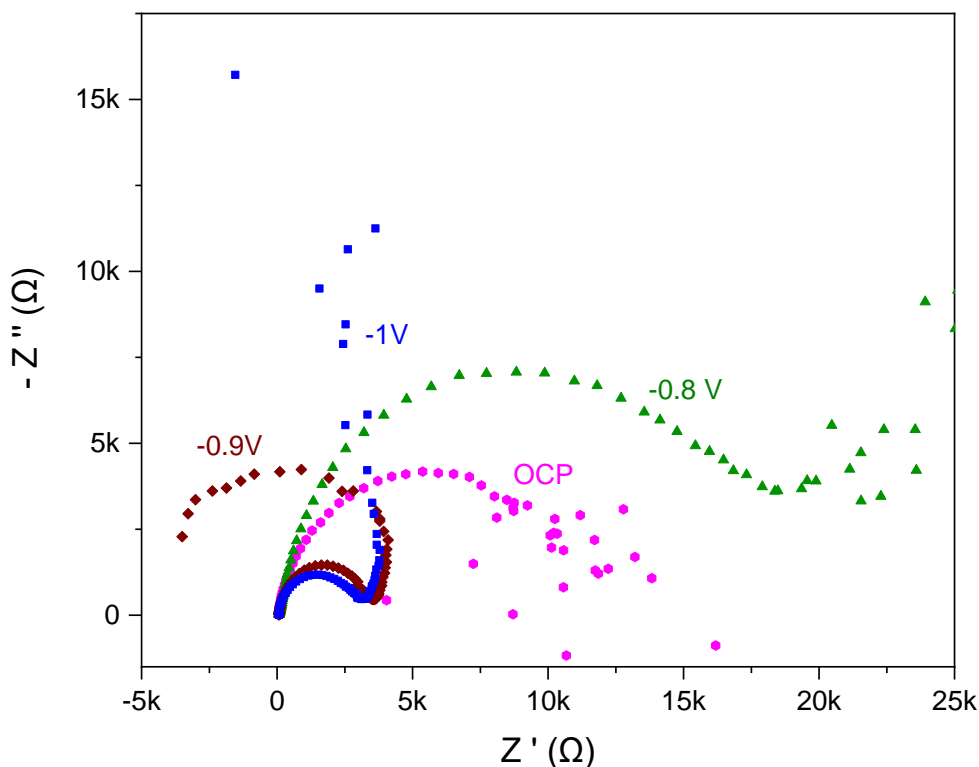


Fig. 3.12: Nyquist plots of EIS measurements performed around the active-pseudo passive potential domain on a Si surface (exposed area  $78 \text{ mm}^2$ ) immersed in NaOH (pH 13).

### 3.4.5 Open circuit potential (OCP) measurements

OCP measurements were conducted over 48 h on Si working electrodes immersed in bulk solution and in the confined/crevice cell (as described in Fig. 3.4a). The results are presented in Fig. 3.13. In the confined/crevice cell, the OCPs measured by the inner and outer RE were nearly identical in the absence of an external cathode, and related to the very small currents flowing without significant ohmic drops in the system. Hence, only the OCP evolution at the inner position in the confined area is shown. In Fig. 3.13 it can be seen that the OCPs established in the confined area are much more active than the ones measured in bulk solution. This is most evident for samples immersed in 0.01 M PBS at  $70^\circ\text{C}$  (Fig. 3.13b), where the bulk OCP is at a constant noble value for Si of ca.  $-430 \text{ mV}_{\text{Ag/AgCl}}$ , but the OCP in the confined/crevice cell varies largely between  $-500 \text{ mV}_{\text{Ag/AgCl}}$  and  $-900 \text{ mV}_{\text{Ag/AgCl}}$ . It is important to recall that the Si/SiO<sub>2</sub> equilibrium potential is ca.  $-1000 \text{ mV}_{\text{Ag/AgCl}}$  at pH 7.4 (in the Si-H<sub>2</sub>O thermodynamic system). The large potential variation indicates an unstable surface oxide with active corrosion driving the OCP to low values ( $-900 \text{ mV}_{\text{Ag/AgCl}}$ ), and resulting corrosion products (as seen in Fig. 3.14a) providing some temporary protection of the Si surface, shortly bringing the OCP back up. This OCP fluctuation also shows that the potential decrease cannot be interpreted in terms of oxygen concentration decrease within the confinement, as this would induce a progressive OCP decay for all the experiments. The OCPs measured in HyClone® WTF were more active than the ones

measured in 0.01 M PBS. Even in bulk HyClone® WTF solution, the OCP was fairly active with ca. -600 to -750 mV<sub>Ag/AgCl</sub> values at 37°C and ca. -800 mV<sub>Ag/AgCl</sub> at 50°C. The most active OCPs were observed for Si exposed to HyClone® WTF in confined/crevice conditions, with values as low as ca. -950 mV<sub>Ag/AgCl</sub> at 50°C. Such low potential values point to a very corrosive system generated by the HyClone® WTF, and indeed severe damages were observed when the cell was opened at the end of the experiment, as seen in Fig. 3.14b.

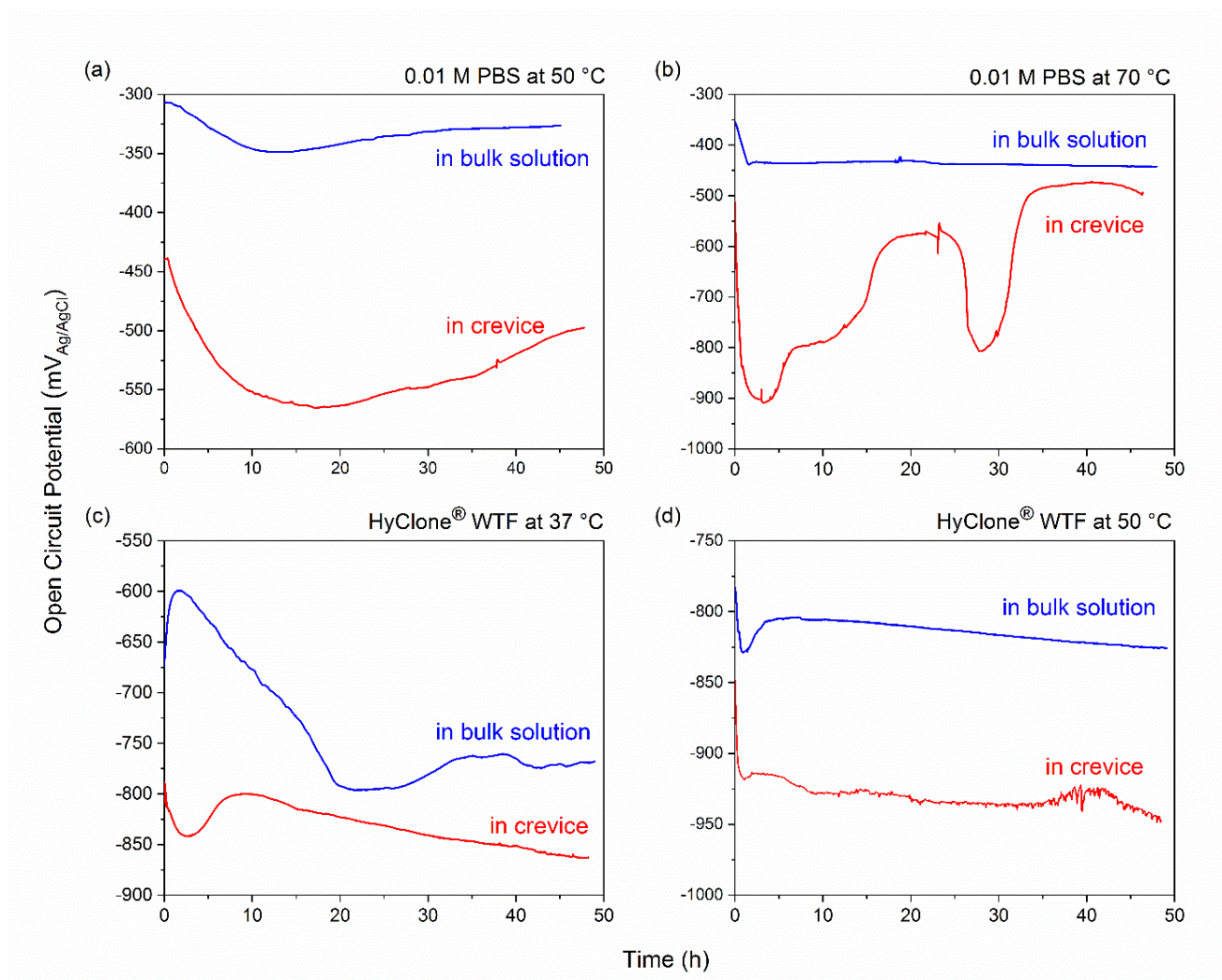


Fig. 3.13: Open circuit potential (OCP) measurements of Si over 48 h in bulk solution and in the confined/crevice cell configuration: (a) 0.01 M PBS at 50°C, (b) 0.01 M PBS at 70°C, (c) HyClone® WTF at 37°C and (d) HyClone WTF at 50°C.



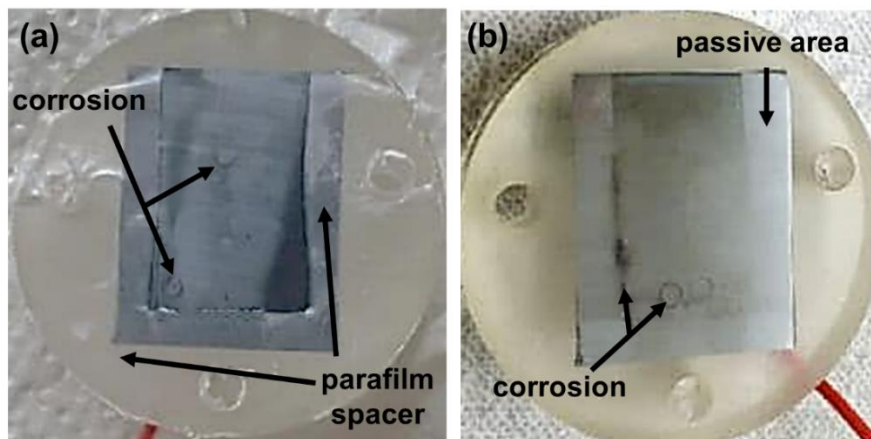


Fig. 3.14: Optical images of Si surfaces after immersion in confined/crevice cells at  $E_{corr}$  in: (a) 0.01 M PBS at 50°C for 48 h, then at 70°C for 48 h, and (b) HyClone® WTF at 37°C for 48 h, then at 50°C for 48 h.

### 3.4.6 Influence of Si wafer doping and resistivity on corrosion

When performing the Si|Si confined/crevice immersion experiments, it was observed that the Si wafer resistivity (dependent on B-doping concentration [122]) directly influenced its corrosion rate. All the experiments presented before were performed with Si wafers having intermediate resistance (Batch 4 in Table 3.2). In order to investigate this dependency, the uniform corrosion rates in the confined/crevice setup geometry were compared for several wafer batches of varying resistivity. The experiments were performed with Si|Si confined/crevices immersed in 0.01 M PBS at 50°C for 20 days. As seen in Table 3.2, the wafers with the lowest resistivity (wafer Batches 1–3), i.e. highest B-doping, showed much lower corrosion rates than those of moderate resistivity (wafer Batches 4–7) with a maximum corrosion rate obtained for Batch 4. This may seem surprising, as an increase in Si conductivity would be expected to increase the corrosion rate, due to the greater availability of electrons for oxidation reactions. A direct correlation between increasing Si conductivity and increasing corrosion rate is indeed obtained when hydrofluoric-based isotropic (very active and uniform dissolution in all orientations) etchants are used; the etching rate increasing at a B concentration above  $10^{18}$  atoms/cm<sup>3</sup> [123]. However, the opposite phenomenon, as in our case, has been documented in alkaline anisotropic etchants such as NaOH and KOH. When etching in anisotropic etchants, the Si etching rate greatly reduces in heavily B-doped wafers, commonly referred to as a p+ etch stop [120,123]. Some authors found this etch stop B concentration to be on the order of  $10^{19}$  atoms/cm<sup>3</sup> (ca. 0.01  $\Omega\cdot\text{cm}$ ) [120,124], while others reported it to be on the order of  $10^{18}$  atoms/cm<sup>3</sup> (ca. 0.04  $\Omega\cdot\text{cm}$ ) in dilute KOH solutions [125]. Hence, the findings presented in Table 3.2 can be considered consistent with literature. In the confined/crevice geometry, the situation is however slightly different. The higher Si wafer resistivity might explain the trenching (see Fig. 3.7) observed and the larger corrosion rate measured directly at the border between the crevice and confined area, due to localization of the cathodic reaction (controlling the anodic pitting in the crevice) at the crevice mouth.

Table 3.2: Influence of Si wafer resistivity on uniform corrosion rate measured at the confined/crevice border.

| Si wafer batch | Resistivity (Ω-cm) | B concentration order (atoms/cm <sup>3</sup> ) | Corrosion rate (nm/h) |
|----------------|--------------------|--|-----------------------|
| 1              | 0.01               | 10 <sup>19</sup>                               | 0.04                  |
| 2              | < 0.1              | > 3 x 10 <sup>17</sup>                         | 0.05                  |
| 3              | 0.2                | 10 <sup>17</sup>                               | 0.09                  |
| 4              | 3-4.2              | 10 <sup>15</sup>                               | 5.60                  |
| 5              | 3-5                | 10 <sup>15</sup>                               | 2.41                  |
| 6              | 5-10               | 10 <sup>15</sup>                               | 2.71                  |
| 7              | 6-7                | 10 <sup>15</sup>                               | 0.41                  |

### 3.4.7 pH determination in the confined cell and surface characterization

In order to confirm that a cathodic-reaction-induced alkaline-type corrosion mechanism could be occurring inside the confined Si area, immersion experiments were performed using the pH-determining device described in Fig. 3.4b. The device was opened after immersion in HyClone® WTF for 10 days at 50°C; the Si surface showed severe anisotropic attack within the area set by the spacer, as seen in Fig. 3.15a, and the agar infiltrated with phenolphthalein was light pink in color, as seen in Fig. 3.15b. When thymolphthalein was used as the pH indicator, severe attack of the Si surface was also seen, but no color change of the agar was observed. This means that the pH increased and established between 8.5 and 10 within the confined space set by the spacer. The experiments performed in 0.01 M PBS at the same temperature and duration also showed substantial anisotropic attack of the Si, but no color change was observed in the agar. While a surface pH increase on the corroding surface can also occur in PBS, its buffering ability might prevent a measurable pH gradient in the agar.

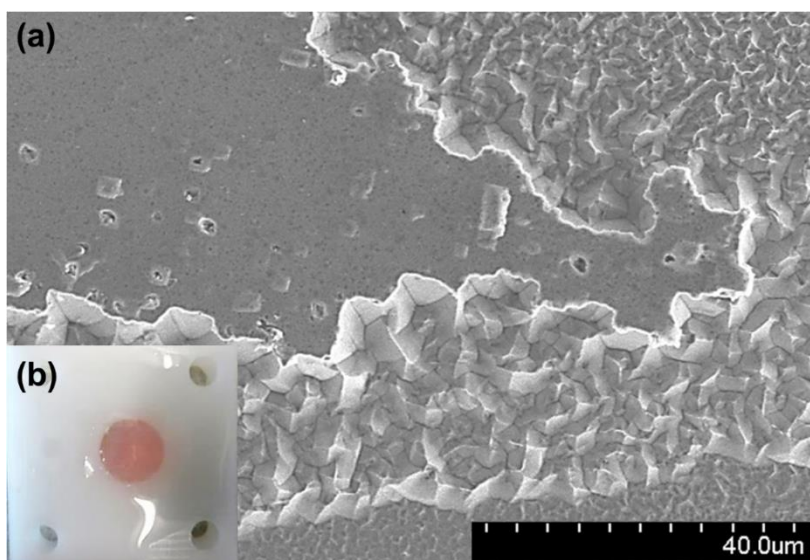


Fig. 3.15: Si after immersion in HyClone® WTF (pH 7.4-7.7) for 10 days at 50°C, using the confined configuration from Fig. 3.1b. Area close to the confinement mouth is shown. (b) Agar infiltrated with phenolphthalein turned pink, indicating a pH above 8.5 occurred.

The corroded Si surface in the confinement and inside the tight crevice (Si|PP spacer) was characterized by X-ray photoelectron spectroscopy (XPS) in order to determine the surface oxide composition/thickness before and after immersion in the HyClone® WTF. The thickness of the SiO<sub>2</sub> (d) film could be determined by utilizing the following well-known relation:

$$d = L \cos \theta \ln \left( 1 + \frac{I_{\text{SiO}_2}}{I_{\text{Si}} R_o} \right) \quad \text{Equation 3-1}$$

Where  $L$  is the attenuation length of the electrons in SiO<sub>2</sub>. The electron can travel this length before its intensity depletes to  $1/e$  of its original value.  $\theta$  is the angle between the sample's surface normal and the electron analyzer,  $I_{\text{SiO}_2}$  and  $I_{\text{Si}}$  are the measured intensities of SiO<sub>2</sub> and Si, respectively, from the sample, and  $R_o$  is the ratio of the intensities from bulk SiO<sub>2</sub> and Si.

$L$  is taken to be 3.448 nm for Al K $\alpha$  x-rays [126].  $R_o$  is 0.933 as measured by [126]. In the XPS system used,  $\theta$  is 45°.  $I_{\text{SiO}_2}$  and  $I_{\text{Si}}$  can be determined by fitting the SiO<sub>2</sub> peak at a 103.5 eV binding energy, and the Si peak at 99.3 eV, from the XPS spectrum obtained from the sample. The intensity areas are then taken under the fitted curves. An example is shown in Fig. 3.16, where a spectrum is measured from a point on a reference (*as-received*) Si wafer.

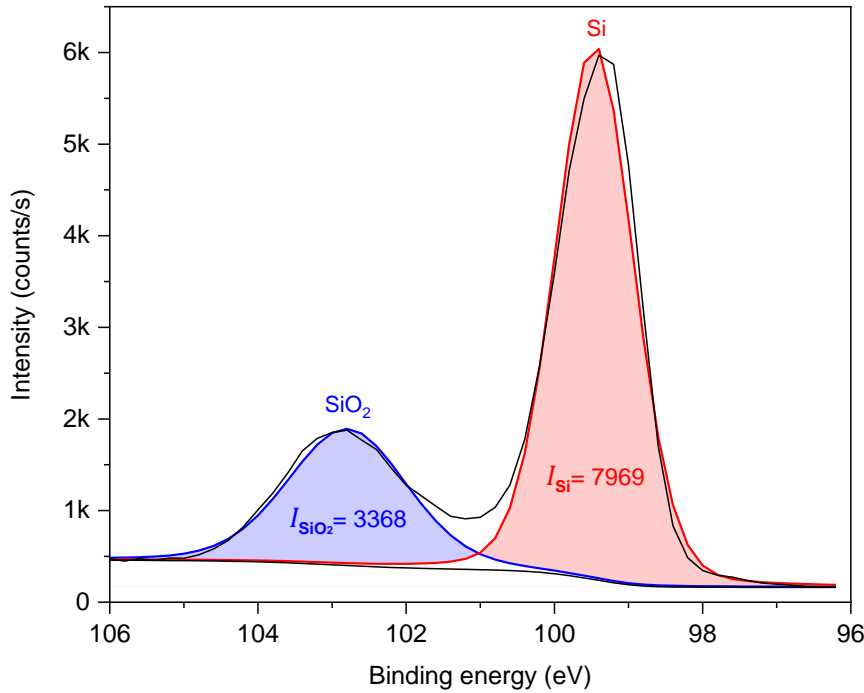


Fig. 3.16: Si2p XPS spectrum from a point measured on an *as received* Si wafer. The SiO<sub>2</sub> and Si contributions are fitted and the area of intensity ( $I$ ) beneath the fittings is determined, corresponding to a native SiO<sub>2</sub> with a thickness of ca. 1 nm.



Taking  $I_{SiO_2}=3368$  and  $I_{Si}=7969$ , the thickness of native oxide ( $d_{ref}$ ) on the *as-received* samples is calculated to be ca. 1 nm using Equation 3-1.

After the immersion in HyClone® WTF for 10 days at 50°C in the confined cell, XPS measurement points were conducted on an area that was within the tight crevice (Si|PP spacer), and within the heavily corroded area of the confinement. Within the tight crevice, an oxide of  $d_{crevice} = 8.6$  nm was determined using Equation 3-1. For comparison purposes, a similar oxide thickness of 8.2 nm was determined by depth profiling on the same measurement point. Due to the high affinity for OH adsorption on the Si surface [120], the film is likely an oxy-hydroxide as opposed to a pure SiO<sub>2</sub> film (as would be found after only air exposure). This oxide growth in the immersed crevice is a further indication of the unstable and defective nature of the passive film in this condition, which makes it susceptible to anion integration and development of pits. In the heavily corroded area of the confinement, the XPS spectrum only showed a Si-oxide peak at 103.5 eV on the surface. Without the presence of an elemental Si signal, Equation 3-1 could not be applied. Depth profiling was therefore conducted on the measurement point on the confined surface, and is shown in Fig. 3.17.

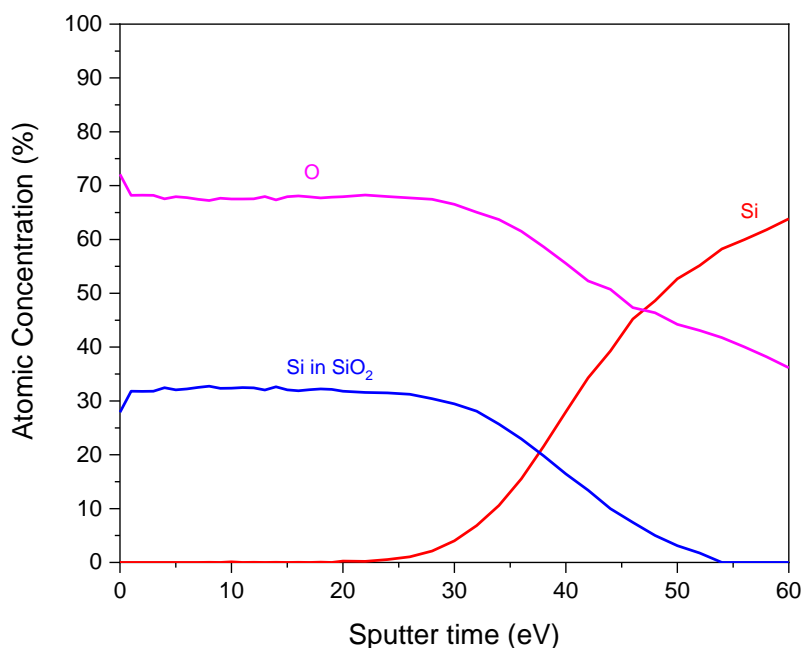


Fig. 3.17: XPS depth profile through a heavily corroded area on Si, after immersion in a confined cell containing HyClone® WTF at 50 °C for 10 days. At a sputter rate of 6.9 nm/min, an oxy-hydroxide layer over 400 nm in thickness is present.

It can be seen that even after 60 min of sputtering at a rate of 6.9 nm/min, the oxygen (O) profile still does not go to zero and there is a poor depth resolution, indicating an inhomogeneous oxide over 400 nm in thickness. This is rather a corrosion product layer (likely an oxy-hydroxide) as opposed to a protective passive SiO<sub>2</sub> film, especially when comparing to the native oxide of ca. 1 nm present on the reference sample, and the slightly thicker ca. 8 nm oxide found within the tight crevice area. This confirms the results and discussion of Fig. 3.12 related to dissolution of Si, which

is not fully active but involves the formation of an intermediate (poorly soluble) surface oxy-hydroxide layer. Phosphates are not detected in this layer indicating the higher solubility of Si-phosphate complexes, which is in line with their aggravating effect on the active dissolution rate of Si.

Since destabilization of the passive Si surface also occurred in bulk HyClone® WTF at 50 °C (Fig. 3.13b), the transformation of the Si surface state from a protective thin oxide, to a thick defective one could also be tracked with a 24 h EIS measurement at OCP (in HyClone® WTF at 50 °C), as seen in Fig. 3.18. The protective native oxide on the Si surface experiences relatively rapid degradation, as indicated by a drastic decrease in impedance (decrease in the semi-circle radius) from initial immersion (at 0 h) to 2 h. After which dissolution of the Si slowly proceeds over time through a thick defective oxide, as evidenced by the moderate impedance values. The EIS measurement clearly shows the poor passivation of Si in this media, but the impedance modulus of around 200 k $\Omega$  indicates that the active dissolution regime is not reached in absence of crevice conditions.

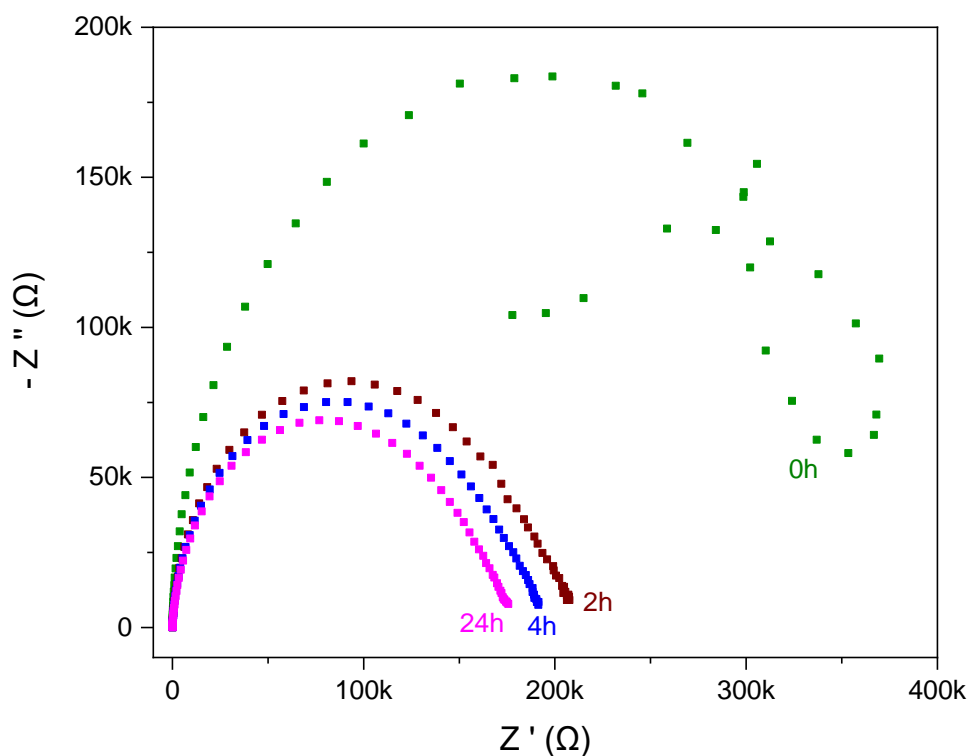


Fig. 3.18: Nyquist plot of EIS measurements performed on Si (exposed area of 78 mm<sup>2</sup>) in HyClone® WTF at 50°C over 24 h at the OCP.

### 3.4.8 Discussion of the corrosion mechanism

Based on the results presented in this study and combining the different aspects of the degradation identified, a simple mechanism explaining the influence of a confined geometry and crevices on the dissolution of Si in physiological simulating solutions is presented in Fig. 3.19 below.

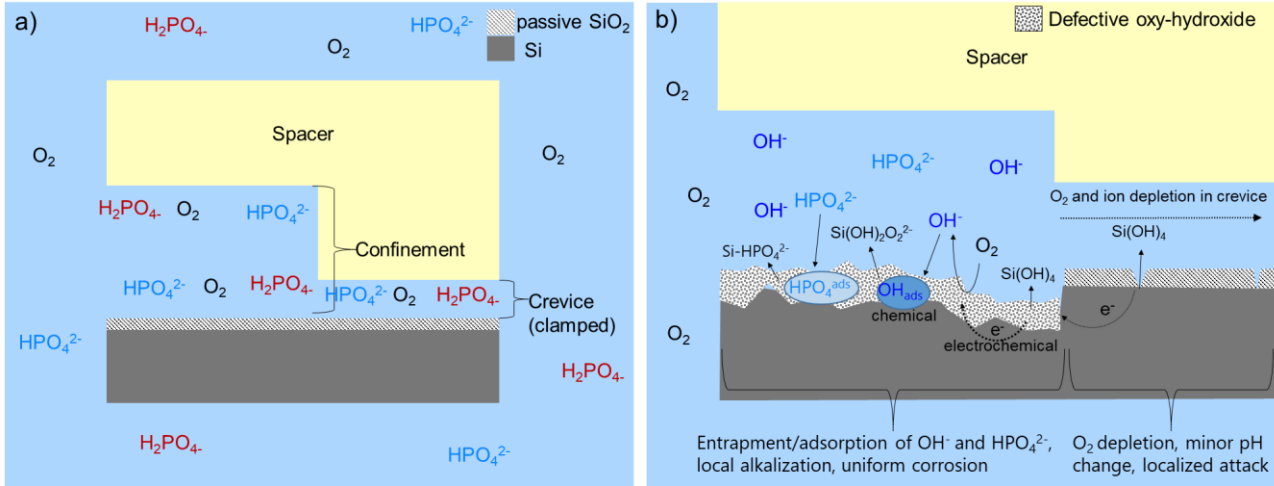
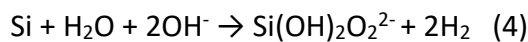
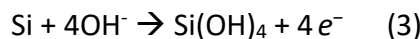
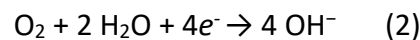


Fig. 3.19: Schematic description of reaction mechanisms showing the influence of a confined/crevice geometry on the dissolution of Si in physiological solutions: a) initial chemistry at the beginning of the immersion experiment, b) corrosion mechanisms in the confined/crevice areas at longer immersion times, the areas of interest are enlarged for clarification.

Initially, when the confined/crevice cell is immersed (or a defect in DLC coating is exposed to solution), a native and protective SiO<sub>2</sub> film is present on the Si surface. This initial protection can be evidenced by a relatively noble measured  $E_{\text{corr}}$  value of ca. -400 mV<sub>Ag/AgCl</sub> in 0.01 M PBS at 37°C (as shown in Fig. 3.10), corresponding to the kinetic equilibrium between passive Si oxidation and oxygen reduction. The native SiO<sub>2</sub> is ca. 1 nm in thickness (as identified by XPS) and in the presence of water can slowly dissociate into soluble ionic species (reaction 1). This may be the initial stage of surface oxide destabilization. In addition, even though SiO<sub>2</sub> is in principle an insulator, such a thin oxide can allow electron tunneling from the Si to the oxide surface and provide them for cathodic oxygen reduction (reaction 2), so that the following reactions are possible:



With time, the O<sub>2</sub> in the tight crevice is used up relatively rapidly, while the confined space continues to be supplied by O<sub>2</sub>. Oxygen reduction therefore predominates in the confined area, resulting in the generation of alkaline OH<sup>-</sup> species that can adsorb and destabilize the passive film, inducing a thicker oxy-hydroxide layer (as evidenced by XPS and EIS). With the use of pH indicators, a local pH

increase between pH 8.5-10 could be identified in the confined area (as shown in Fig. 3.15). Cathodic reaction induced local pH increases at a Si-oxide/electrolyte interface could also occur in bulk solution, however these surface pH gradients are short lived, due to better ionic diffusion and equilibration. In a confined geometry, ion diffusion becomes restricted, and accumulation of  $\text{OH}^-$  can eventually lead to an additional anodic electrochemical (reaction 3), or chemical (reaction 4), alkaline-type dissolution mechanism [127].

Considering purely the chemical equilibria and electrochemical thermodynamic aspects of the Si- $\text{H}_2\text{O}$  system at 25°C (Pourbaix diagram [102]), generation of soluble species and active dissolution in the confined area would be occurring starting at a pH of ca. 10. According to the pH range identified experimentally with the pH indicators, pH 10 is not reached in the confined area. The confined electrolyte chemistry might however get close to this pH 10 stability boundary and the surface pH is anyway difficult to assess. Additionally, elevating the temperature narrows the  $\text{SiO}_2$  thermodynamic stability domain inducing corrosion below pH 10, and the experiments showed clear evidences of slow active dissolution (trenching) especially in the presence of phosphates. Surface activation, identified by a measured OCP decrease down to  $-850 \text{ mV}_{\text{Ag}/\text{AgCl}}$ , occurs already at 37°C in HyClone® WTF and is clearly detectable for PBS in confined/crevice conditions from a temperature of 50°C. In addition, when the OCP in the confinement drops to active values of ca.  $-800 \text{ mV}_{\text{Ag}/\text{AgCl}}$  and  $-950 \text{ mV}_{\text{Ag}/\text{AgCl}}$  (Fig. 3.13), cathodic hydrogen reduction can also occur and progressively accelerate corrosion.

Considering the systematic study of the influence of specific anions, phosphates and chlorides (Table 3.1 and Fig. 3.9), it becomes clear that the presence of phosphate is an additional parameter to consider in surface oxide destabilization. For measurements performed at pH 8.5, no uniform corrosion is detected in the confined area in presence of chloride, supporting the fact that the predicted pH 10 oxide stability boundary is valid in absence of the additional phosphate surface interactions. On the other hand, severe corrosion is identified at pH 8.5 in the presence of phosphate species (Table 3.1). The Arrhenius plot in Fig. 3.8 pointed to an activation energy related to the formation of soluble phosphorous-silicon complexes, as proposed by W. van Gelder [103].

Lastly, considering in more detail the topography profile of Fig. 3.7 in relation with the Si resistivity discussion, some assumption can be made about galvanic coupling in the confined/crevice aeration cell geometry. For the middle resistivity domain (Batch 4 Si-wafer:  $3 - 4.2 \Omega\cdot\text{cm}$ ), a clear trench with enhanced dissolution at the confined/crevice border is continuously observed. For a semiconducting substrate, if a cathodic reaction can take place to initially support the anodic localized dissolution in the crevice, its rate will be higher at the confined/crevice border. The cathodic reaction is related to the observed pH increase, and in the presence of phosphate will increase the corrosion susceptibility in the confined area. Lowering the resistance of the Si will better distribute the cathodic reaction along the confined surface during the initial stage of localized corrosion in the crevice, and might delay the pH change and detrimental effect in the confined area. This may explain why very low corrosive attack is measured and no trenching is visible in the confined area for the highly

conductive wafers. Very high Si resistance on the other hand will hinder galvanic coupling and as a consequence decrease the trenching depth.

One aggravating factor that has not yet been identified is the exact component of the HyClone® WTF that has a negative influence on the passive film stability. HyClone® WTF already induces increased surface reactivity at 37°C (low OCP, corrosion) in the absence of a confinement/crevice geometry, meaning that its viscosity and hindered ionic diffusion might not be the only detrimental factor contributing to the corrosion mechanism.

### 3.4.9 Si corrosion in the TiAlV/Si/DLC system with static stress

The results presented in this chapter can now be correlated with previous work relating to the influence of stress on the delamination behavior of a TiAlV/Si/DLC explant [104]. Hauert et al. tracked the DLC delamination speeds around Rockwell indentations performed in the TiAlV/Si/DLC explant (the Si interlayer was 60 nm) described in Fig. 3.1. The explant did not show ongoing delamination when immersed in 0.01 M PBS at 37°C for 228 days. However when the solution was exchanged with HyClone® WTF, delamination started immediately, as seen in Fig. 3.20. The average speed of delamination was calculated to be ca. 100  $\mu\text{m}/\text{year}$ . Analogous to the results presented in the Arrhenius plot from Fig. 3.8, Si dissolution in a confinement did not initiate (or took a very long time to) in PBS at 37 °C, and therefore the point falls off the trendline. However a Si dissolution rate of 3.6 nm/h (32  $\mu\text{m}/\text{year}$ ) occurred in confined HyClone® WTF at 37°C. Therefore, crevice corrosion of the Si interlayer in the TiAl/Si/DLC explant likely played a role in the DLC delamination, and the added aggravating stress component formed by the Rockwell indent may slightly speed up the interlayer dissolution rate.

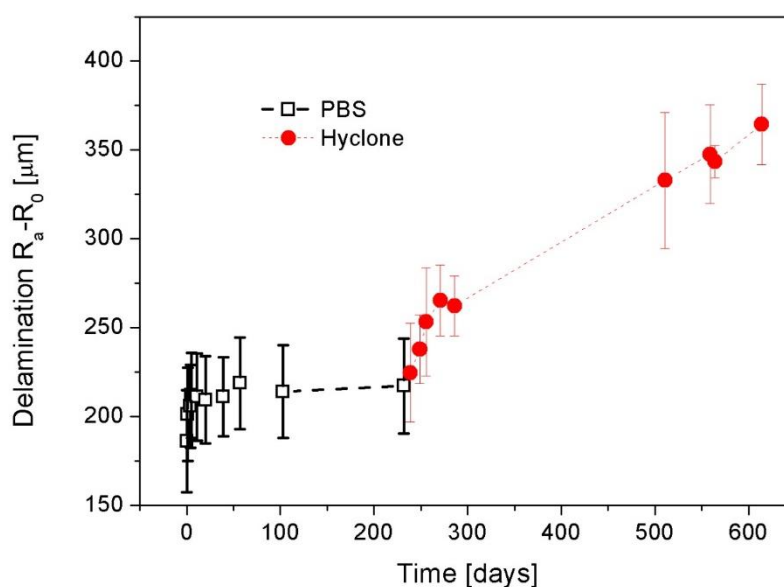


Fig. 3.20: Average delamination radius around a Rockwell indent performed in a TiAlV/Si/DLC explant and immersion in PBS, then HyClone® WTF, at 37°C. The delamination front is averaged as a circle with radius  $R_a$ , and the edge of the Rockwell indent is at radius  $R_o$  (Reprinted from *Acta Biomaterialia* [104], with permission from Elsevier).

### 3.5 Chapter conclusions

An investigation of the corrosion behavior of Si in physiological simulating solutions (0.01 M PBS and HyClone® Wear Test Fluid, pH 7.4-7.7) was presented in this study. Long-term and accelerated immersion experiments were developed to investigate the influence of crevices, confined spaces, and bulk solutions on Si stability. Complementary electrochemical measurements were conducted in bulk and confined/crevice configurations to study Si corrosion initiation and oxide stability. The following can be concluded:

- The stability of Si and its naturally grown surface oxide varies drastically between bulk, confined, and crevice immersion conditions.
- In a tight crevice (few microns in thickness), localized corrosion with the formation of pyramidal pits in 0.01 M PBS and HyClone® WTF was observed.
- When constricted to a confined (ca. 0.5 mm thick electrolyte)/crevice geometry, Si corroded uniformly up to ca. 3.6 nm/h in HyClone® WTF at 37°C, while no measurable damage was observed after exposure in bulk solution.
- Activation (surface oxide destabilization) could be evidenced by in-situ OCP evolution measurements in a confined electrochemical cell geometry; potentials were consistently more active (as low as -950 mV<sub>Ag/AgCl</sub>) compared to the values measured in bulk solution for the simulated physiological solutions considered.
- A higher pH of 8.5-10 was measured in the confined area after immersion in HyClone® WTF for several days, indicating that a detrimental alkalization process had occurred on the Si surface.
- The corrosion in the confinement was further accelerated by increasing the temperature and a linear Arrhenius trend with activation energies of 106 KJ/mol in 0.01 M PBS, and 109 KJ/mol in HyClone® WTF, was observed, corresponding to a phosphorous-silicon interaction mechanism, with soluble complex formation.
- Alkaline phosphate species contributed to accelerating the Si corrosion initiation and dissolution rates, whereas chlorides seemed to have little influence on the Si corrosion susceptibility.
- The overall corrosion mechanism is initiated by galvanic coupling, as observed by the separation of pitting in the crevice and trenching at the border with the confined area, pH increase and phosphorous-silicon complexation.
- The results presented in this study confirmed previous investigations on the delamination failure of TiAlV/Si/DLC explants, showing that the Si interlayer suffered from crevice corrosion, with stress slightly increasing the dissolution rate.

Overall, when determining the stability of biomedical implantable components, this study illustrates the importance of considering geometrical aspects for in-vitro testing procedures, aspects that can be inherent of the implant design or generated by contact with tissue in the in-vivo environment. These findings can be used to provide better predictions on the lifetime of implantable Si components and Si-based interlayers, as well the presented methodologies can be applied to any other material of interest.





## Chapter 4 Influence of stress and fatigue on interface corrosion susceptibility

*The contents of this chapter are reproduced with permission from the published article [100]:*

### **Corrosion fatigue in DLC-coated articulating implants: an accelerated methodology to predict realistic interface lifetime**

*Ainhua Pardo<sup>1</sup>, Emilija Ilic<sup>1</sup>, Kerstin Thorwarth<sup>2</sup>, Michael Stiefel<sup>3</sup> and Roland Hauert<sup>1</sup>*

<sup>1</sup> Empa, Swiss Federal Laboratories for Materials Science and Technology, Laboratory for Joining Technologies and Corrosion, Switzerland

<sup>2</sup> Empa, Swiss Federal Laboratories for Materials Science and Technology, Laboratory for Nanoscaled Materials Science

<sup>3</sup> Empa, Swiss Federal Laboratories for Materials Science and Technology, Laboratory for Transport and Nanoscale Interfaces

*Science and Technology of Advanced Materials (2019)*

*Volume 20, Issue 1, pages 173-186*

*doi:10.1080/14686996.2019.1580483.*

*© The Authors 2019. Published by Informa UK Limited, trading as Taylor and Francis Group.*

**Contributions of E.Ilic:** *Performed specific coating depositions and experiments in collaboration with A. Pardo. Contributed key ideas and discussion points.*

## 4.1 Chapter overview

Corrosion Fatigue (CF) and stress corrosion cracking (SCC) have been identified as some of the major issues associated with implant failure [128]. In regards to hard-coated implants, although the coating itself is wear resistance and considered chemically inert, the substrate/coating interface is often the point of failure. Loads applied on the coated system can cause corrosion-induced crack propagation at the interface (initiated at coating defects) resulting in delamination and ultimately implant failure. In-vitro testing of implants often requires long-term testing in body-like fluid in an articulating simulator. These tests are often performed at low articulating frequencies (1-3 Hz) in order to simulate body movements over extended periods and avoid protein denaturation, which can change the surface lubrication properties of the counterparts. However, concerning coated implants, the focus of the investigation presented in this chapter is on the failure of the substrate/coating interface as opposed to wear of the surface. Therefore, higher testing frequencies are used in order to attain faster results, which are then fitted and extrapolated to correlate with long-term data.

In this chapter, a methodology is presented to simulate and accelerate fatigue corrosion acting on a buried interface in articulating DLC coated implants. A ball-on-disk wear simulator is utilized in order to apply reciprocating loads onto DLC coated CoCrMo medical grade substrates, with an a-C:H:Si (Si-DLC) adhesion-promoting interlayer. The number of loading cycles required to induce delamination at the interface in physiological-simulating solution is determined. Small oxygen contamination at the interlayer/substrate interface was found to strongly, and adversely, influence delamination. As interface corrosion is usually initiated at defective areas in the coating, the experiments were conducted on simulated pre-scratches. The influence of static load on the interfaces, induced by a Rockwell indentation, was also compared.

## 4.2 Experimental

### 4.2.1 Materials and methods

Medical grade CoCrMo alloy ( $\text{CoCr}_{28}\text{Mo}_6$ ) substrate disks were polished to mirror finish, ultrasonically cleaned in acetone, then ethanol, for 15 min, and consecutively dried under Ar flow. Using the same procedure and PACVD chamber described in section 2.2.1, the substrates were pre-cleaned via Ar sputtering in the chamber. A 210-220 nm Si-doped hydrogenated amorphous carbon (Si-DLC), a-C:H:Si, interlayer was grown using tetramethylsilane (TMS),  $\text{Si}(\text{CH}_3)_4$ , gas, after which a 4  $\mu\text{m}$  DLC coating (a-C:H) was deposited (using the same parameters as described in section 2.2.1). Three coating systems were prepared with varying oxygen contamination levels at the CoCrMo/Si-DLC interface: CoCrMo/Si-DLC(0.0% $\text{O}_2$ )/DLC, CoCrMo/Si-DLC(0.5% $\text{O}_2$ )/DLC and CoCrMo/Si-DLC(1% $\text{O}_2$ )/DLC, where  $x\% \text{O}_2$  ( $x = 0.0, 0.5$  and  $1.0$ ) refers to the partial pressure ratio of oxygen/argon. Note that 0.0% means that the system was not intentionally contaminated. The partial  $\text{O}_2$  pressure was introduced at the beginning of the deposition process and stopped after 2 min of TMS growth, allowing for the presence of  $\text{O}_2$  at the Si-DLC/DLC interface.

Since it was previously observed that delamination always originated from a scratch or coating defect, a pre-scratch was applied on the coated samples in order to mimic a substantial defect (one that penetrated the Si-DLC/DLC interface). A 1 cm long pre-scratch was applied at a force of 3 N and speed of 1 mm/s on the coated sample using a custom-built scratching device; consisting of a pyramidal diamond tip mounted in a reciprocating-sliding device. The scratching device allowed for a reproducible scratch on each sample, avoiding human error. In order to simulate fatigue at the interface, alternating loads were carried out over a segment of the pre-scratch with an alumina sphere counterpart (6 mm diameter) using a high frequency reciprocating sliding apparatus (HFRR, PCS Instruments), shown in Fig. 4.1. The sliding load was applied perpendicularly over the pre-scratch along a stroke length of 2 mm at a frequency of 15 Hz. Due to some geometrical limitations in the sliding experimental setup, the wear track was not always completely perpendicular to the scratch. The experiments were conducted in the following various electrolytes at a temperature of 37 °C: PBS (pH 7.4), Milli-Q water (18.2 M $\Omega$ ·cm, pH 5.5), 0.14 NaCl (pH 5.5), Ringers solution (0.15 M NaCl, 5 mM KCl, 4 mM CaCl<sub>2</sub>, 2 mM NaHCO<sub>3</sub>, pH7.4) and Hyclone® WTF (contains 34 g/L protein). After the reciprocating sliding experiments, the sample's surface was inspected with an optical microscope (Axiovert 100 A, Carl Zeiss Jena GmbH).

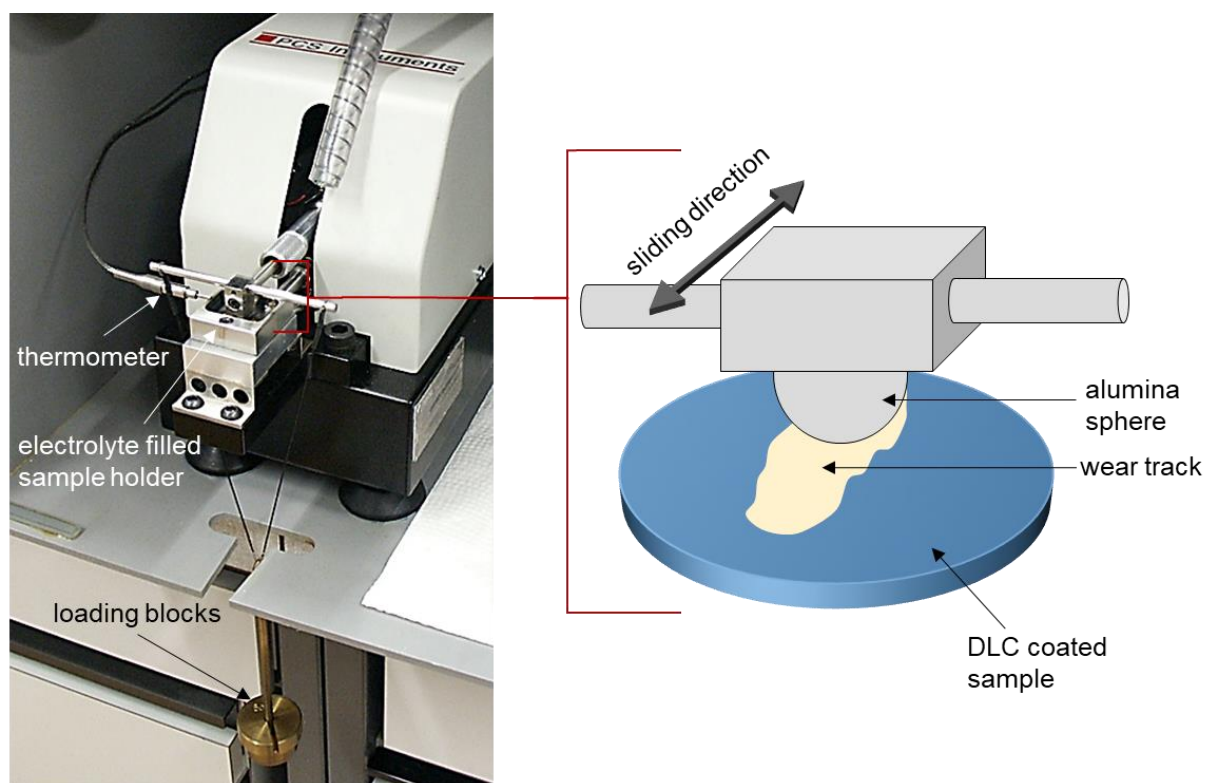


Fig. 4.1: (left) High frequency reciprocating sliding apparatus (HFRR, PCS Instruments) used for applying fatigue load over samples. (right) Enlarged schematic of the reciprocating pair; an alumina counter sphere slides over the DLC coated sample leaving a wear track.

Crack propagation at the buried interface was assessed by preparing a FIB cross-section on a delaminated area after a reciprocating sliding experiment, using as FIB/SEM system (FEI Helios 660 G3 UC). The FIB was operated at 30 keV and beam currents of 47 nA to 780 pA. A thin Pt layer was locally deposited prior to cutting in order to improve the resolution of the cut.

In order to investigate the influence of a static load on the interface, the delamination area around a Rockwell indent into the samples was monitored. The indents were initially made using an Ernst NR 3R Rockwell indenter based on the standard C-scale (1470 N load, 120° spheroconical diamond tip with 0.2 mm radius). A Rockwell indent induces plastic deformation of the sample, exerting an added static stress (in addition to the intrinsic stress caused by the DLC itself) at the coating/substrate interface, as was previously demonstrated by FEA [65,66].

## 4.3 Results and Discussion

### 4.3.1 Influence of the electrolyte

The influence of the six different media on the delamination behavior of a weakened interface, CoCrMo/Si-DLC(1.0%O<sub>2</sub>)/DLC, was compared up to 13500 sliding cycles (15 min) at a 5 N load and 15 Hz, for the purpose of selecting a representative environment which enhances CF. Optical microscope images of the resulting damage are presented Fig. 4.2. It can be seen that the degree of delamination is highly correlated to the electrolyte used. Similarly to the isolated salt solution experiments used to investigate the crevice corrosion of Si in section 3.4.3, the influence of chlorides on the CF behavior of the Si-DLC interlayer was evaluated by performing an experiment in NaCl solution with the same concentration as that in PBS (0.14 M NaCl). As can be seen the NaCl solution, along with air, Milli-Q water and Ringers solution, did not trigger delamination. Hence, chlorides and carbonates (present in Ringers solution) did not have an effect on corrosion. In contrast, the experiments performed in the phosphate-containing solutions, PBS and Hyclone® WTF, showed considerable coating delamination. This cannot simply be an increasing pH effect, as Ringers solution is of same pH as PBS and HyClone® WTF. It is also understandable that the more viscous protein-containing solution (HyClone® WTF) will have a different lubricating effect on the sliding counterparts, and this may be an additional parameter affecting delamination. However PBS is nearly the same viscosity as Milli-Q water, 0.14 M NaCl and Ringers solution, hence it cannot solely be a difference in lubrication properties affecting delamination. The species within the phosphate-containing solutions themselves must be influencing the system. It could be that the phosphate species are inducing corrosion by complexing with the Si in the Si-DLC interlayer, similarly to the mechanism that was discussed in section 3.4.8. Further experiments are needed in order to have a deeper understanding of the corrosive species influencing the Si-DLC/DLC interface (as is outlined in future work). Therefore, in order to induce CF, but avoid introducing additional lubrication-affecting properties, PBS was chosen as the corrosive test media in the following experiments.

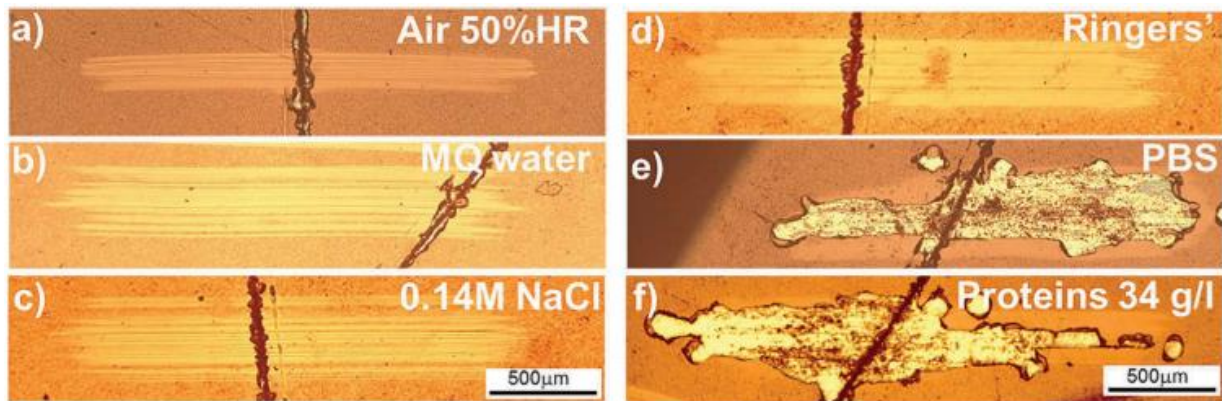


Fig. 4.2: Influence of various electrolytes on the delamination behavior of a CoCrMo/Si-DLC(1.0%O<sub>2</sub>)/DLC sample at 37 °C. Optical microscope images after 13,500 reciprocating sliding cycles over a pre-scratch under a normal load of 5 N at 15 Hz.

#### 4.3.2 Influence of fatigue

A Wöhler curve represents the number of loading cycles needed to reach a critical stress leading to crack propagation and subsequent material fracture. Corrosive media can accelerate this process, by reducing the critical stress limit required for fracture to occur. In this study the critical load,  $L_c$ , required to induce delamination at the Si-DLC/DLC interface will be considered. The justification being that when applying a sliding loading on a DLC/substrate system, the highest stresses are observed at the interface close to a defect, as was calculated by finite element analysis (FEA), presented in section 5.2. The  $L_c$  required for interface failure, and hence coating delamination, in PBS at 37 °C was determined by increasing the normal load by increments of 0.5 N (lowest allowable by the equipment), up to the load at which delamination at the vicinity of the pre-scratch could be seen with a microscope. A demonstrative example of this experimental approach on the CoCrMo/Si-DLC(1.0%O<sub>2</sub>)/DLC sample is shown in Fig. 4.3.

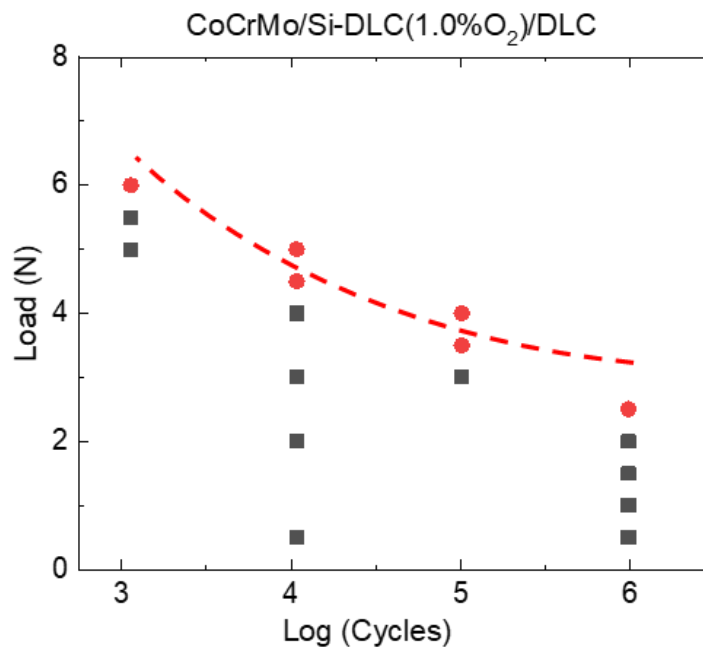


Fig. 4.3: Experimental methodology used to create the Wöhler curve. The load is increased by increments of 0.5 N, grey squares, until delamination occurs at the critical load ( $L_c$ ), red dots.

The Wöhler curves of the CoCrMo/Si-DLC( $x\%O_2$ )/DLC samples are presented in Fig. 4.4.

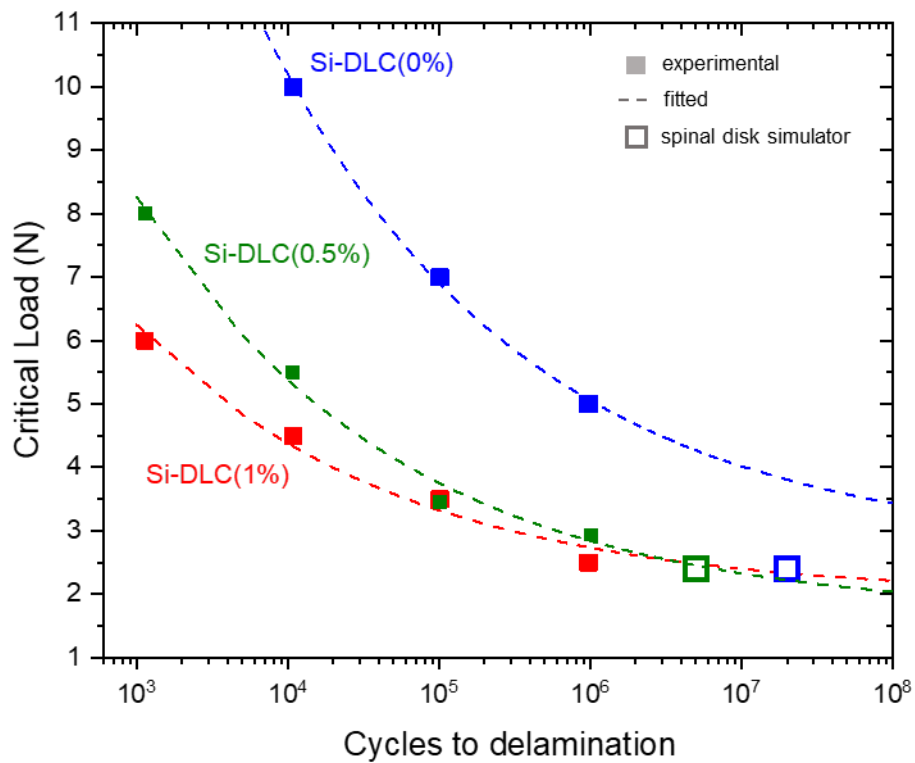


Fig. 4.4: Wöhler-like curves for CoCrMo/Si-DLC( $x\%O_2$ )/DLC system. The critical load required for coating delamination to occur is recorded vs. the cycles to delamination. Filled-squares represent experimental data and dotted lines are the fittings. Empty-squares correspond to long-term experiments from a spinal disk simulator.

Experimental data points are represented by filled square symbols, and the dashed lines represent the fitted data corresponding to the fatigue equation revealed by Stromeier [129]:

$$L_c(n) = L_e + A \left( \frac{10^6}{n} \right)^{0.25} \quad \text{Equation 4-1}$$

Where  $L_e$  is the extrapolated endurance limit,  $n$  is the number of cycles to delamination and  $A$  a coefficient changing with the endurance limit. The fitted parameters for the curves are summarized in Table 4.1 below:

Table 4.1: Fitted parameters from the Wöhler curves corresponding to Equation 4-1.

| Sample                        | $L_e$           | $A$             |
|-------------------------------|-----------------|-----------------|
| CoCrM/Si-DLC(0% $O_2$ )/DLC   | $2.68 \pm 0.20$ | $2.37 \pm 0.09$ |
| CoCrM/Si-DLC(0.5% $O_2$ )/DLC | $1.66 \pm 0.23$ | $1.17 \pm 0.06$ |
| CoCrM/Si-DLC(1% $O_2$ )/DLC   | $1.97 \pm 0.24$ | $0.75 \pm 0.07$ |

The curves show that with increasing  $O_2$  contamination at the interface, the experimentally determined critical loads required for delamination decrease (the curve moves downward). As well the extrapolated  $L_e$  is noticeably higher for the non-contaminated interface. Although the extrapolated fitting of the Si-DLC(0.5% $O_2$ ) and Si-DLC(1% $O_2$ ) curves should theoretically not cross, it occurs within the error margins of the fitting, as seen in Table 4.1. These results already evidence that the coated system seems to be influenced by a corrosion fatigue process. Further, recalling back to previous work where a ball-on-socket spinal disk simulator was used to investigate the fatigue behavior of similar samples [84]; a CoCrMo/Si-DLC(0.5% $O_2$ )/DLC disk delaminated in the simulator after ca. 5 million reciprocating cycles, at a frequency of 3 Hz. Taking 5 million as the cycles to delamination, a semi-quantitative point representing this long-term experiment (19 days) is placed on the fitted DLC/Si-DLC (0.5% $O_2$ )/DLC curve at an  $L_c$  of 2.4 N, as marked by a green-outlined square in Fig. 4.4. Given the delamination around a defect initiated at 2.4 N, this long-term experiment could be linked to the accelerated experiments; and may follow the same delamination pattern. Similarly, a DLC/Si-DLC(0% $O_2$ )/DLC disk did not delaminate after 20 million cycles (at 3Hz, 77 days) in the spinal disk simulator, this point has also been placed in Fig. 4.4 and is represented by a blue-outlined square. Since the disk did not delaminate, the  $L_c$  was not reached, and therefore this point lies below the extrapolated DLC/Si-DLC(0% $O_2$ )/DLC curve.

More experimental data points and at higher cycles would definitely improve the fitting in Fig. 4.4 and reduce errors. This is planned in future work, but as an initial trial this accelerated experimental approach was able to generate Wöhler curves of delaminating DLC coated interfaces relatively rapidly, and semi-quantitatively correlate them to long-term experiments.

In order to inspect the failed interface, a cross-sectional FIB cut was performed on the DLC/Si-DLC(1%O<sub>2</sub>)/CoCrMo sample, after delamination occurred at a  $L_c$  of 4 N. The FIB cut was performed along the sliding direction, and SEM images of the cut sample are presented in Fig. 4.5. It can be seen that a substantial crack is present along the Si-DLC(1.0%O<sub>2</sub>)/CoCrMo interface, ca. 8  $\mu$ m in length. This verifies that the contaminated interface is indeed the source of crack initiation and propagation resulting in coating delamination, likely aided by the corrosive environment (as was demonstrated by the various electrolyte investigations in Fig. 4.2). Conversely, the top uncontaminated Si-DLC/DLC interface is completely intact and does not present any cracks. Furthermore, shear bands can be seen propagating at an angle of ca. 30° from the interface, and into the DLC coating. The presence of shear bands confirms that the amorphous-C matrix and the Si-DLC interlayer underwent the plastic deformation associated with fatigue. Analogously to amorphous metals, shear bands form due to local atomic rearrangements in order to accommodate plastic deformation [130]. Discontinuous cracks can also be seen along the shear bands (Fig. 4.5c). This was also observed in previous work on similar samples after 100 million reciprocating cycles were conducted in a spinal disk simulator [83]. It may be that the repetitive stress placed on these localized plastic deformation zones causes cracks at several locations.

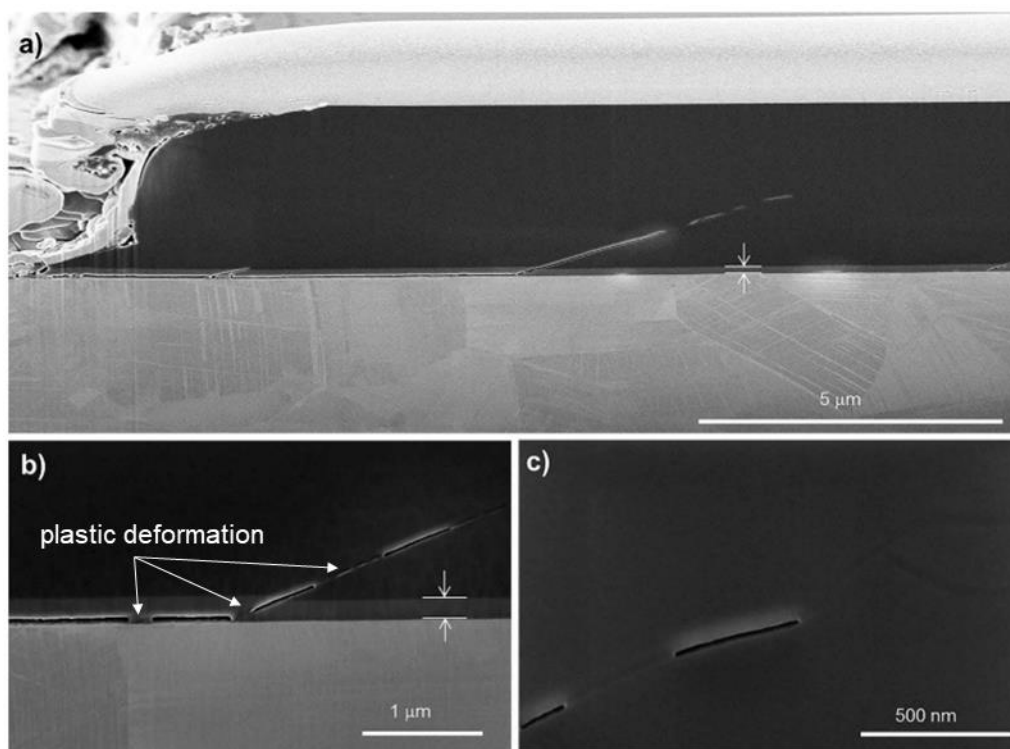


Fig. 4.5: SEM image of a CoCrMo/Si-DLC(1.0%O<sub>2</sub>)/DLC cross-section performed in the vicinity of a delamination area, after 13,500 loading cycles under 4 N load in PBS at 37 °C. a) Overview with 8  $\mu$ m long



crack at interface. b) Close up of a shear band initiating from interface through interlayer and into DLC. Plastic deformation of the Si-DLC interlayer is also seen. c) Discontinuous cracks within the shear band.

### 4.3.3 Influence of static stress

It is interesting to consider that when the interface stress is static, the CoCrMo/Si-DLC( $x\%O_2$ )/DLC samples do not present any delamination when  $x$  is equal to and below 0.5%. Fig. 4.6a shows the evolution of a Rockwell indentation placed into a CoCrMo/Si-DLC(0.5% $O_2$ )/DLC sample and immersed in PBS for 9 years. After such a long time, the coating still does not present any delamination near the Rockwell. It is only when a cyclic load is applied, via the reciprocating sliding rig, which the contaminated interface delaminates. However at higher interface oxygen contamination levels, 2% and above, delamination around a Rockwell indent occurred already after 2 years in PBS, and increased substantially up to year 8, as seen in a CoCrMo/Si-DLC(2.0% $O_2$ )/DLC sample in Fig. 4.6b. Whereas the samples did not delaminate in air. Therefore when immersed in corrosive medium (PBS or HyClone), at very small contamination levels ( $x \leq 0.5$ ) the CoCrMo/Si-DLC( $x\%O_2$ )/DLC system seems to only be influenced by the more aggressive corrosion fatigue process, whereas at higher interface contamination levels ( $x \geq 2$ ) a static stress can already induce cracking at the interface.

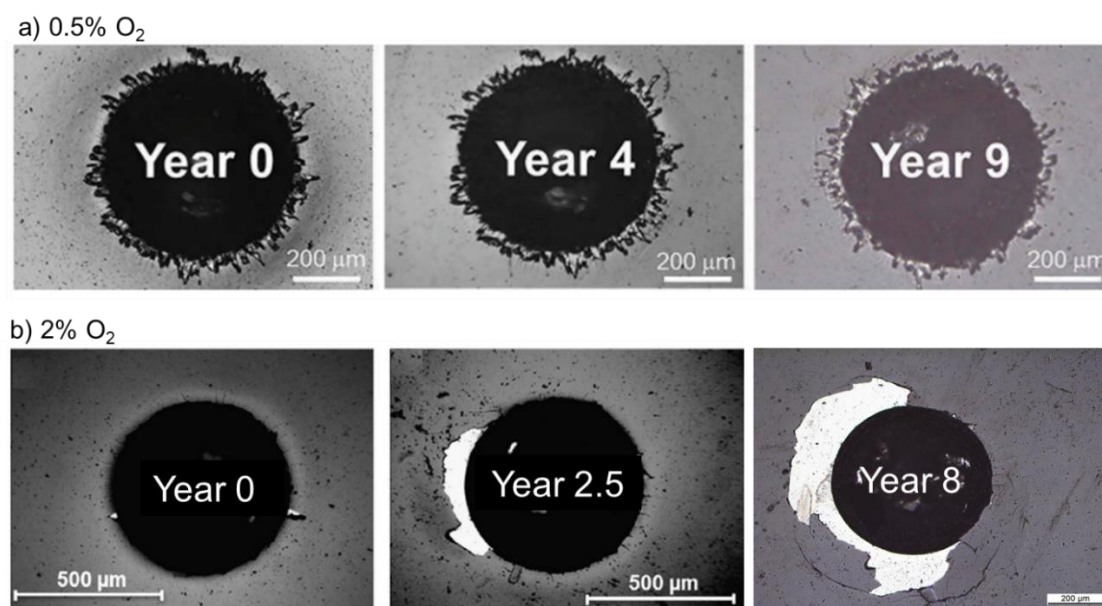
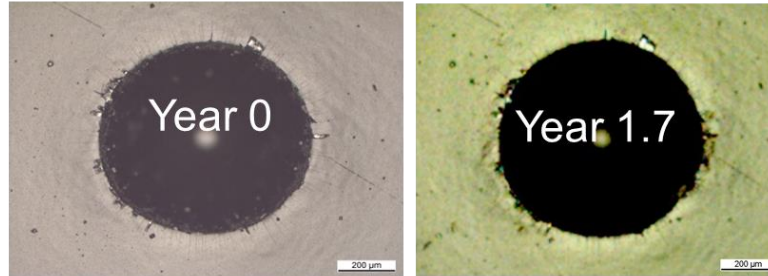


Fig. 4.6: Evolution of a Rockwell indentation placed in: a) CoCrMo/Si-DLC(0.5% $O_2$ )/DLC and b) CoCrMo/Si-DLC(2.0% $O_2$ )/DLC and immersed in 0.01 M PBS at 37°C.

If the substrate is TiAlNb, a Rockwell indent monitored around the TiAlNb/Si-DLC( $x\%O_2$ )/DLC system shows slightly better results. As seen in Fig. 4.7, even at an oxygen contamination level of 2%, the delamination area was nearly unchanged after 1.7 years immersed in PBS. These samples will continue to be monitored in future work. The better resistance to SCC in the case of the TiAlNb substrate can likely be attributed to the stronger (more energetically favorable) TiC carbide formed between titanium and the Si-DLC interlayer, so that  $O_2$  contamination is not as influential at this

interface. Whereas the unfavorable formation of CoC ( $\Delta G_f^\circ$  of +9.0 kcal/mol) between CoCrMo and Si-DLC may make the integrity of this interface more sensitive to contaminants.

a) TiAlNb/Si-DLC(0.5%O<sub>2</sub>)/DLC



b) TiAlNb/Si-DLC(2.0%O<sub>2</sub>)/DLC

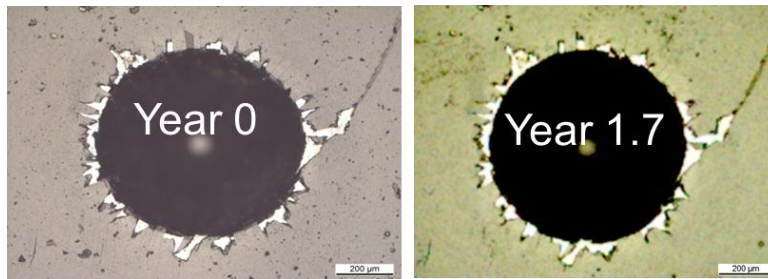


Fig. 4.7: Evolution of a Rockwell indentation placed in: a) TiAlNb/Si-DLC(0.5%O<sub>2</sub>)/DLC and b) TiAlNb/Si-DLC(2.0%O<sub>2</sub>)/DLC and immersed in 0.01 M PBS at 37°C.

#### 4.4 Chapter conclusions

The influence of cyclic mechanical loading on the behavior of CoCrMo/Si-DLC( $x\%O_2$ )/DLC in corrosive media was investigated and the following can be concluded:

- Under a reciprocating load, the type of electrolyte strongly influenced interface delamination, with PBS and HyClone® WTF causing substantial delamination, while no delamination occurred in water, Ringers, and NaCl solution.
- Wöhler curves of the delaminating interface could be generated with accelerated experiments, demonstrating the influence of fatigue on the interface integrity. The critical load ( $L_c$ ) required for delamination and the endurance limit ( $L_e$ ) decreased with increasing O<sub>2</sub> contamination at the CoCrMo/Si-DLC interface.
- Under static stress conditions (induced by a Rockwell indent), the CoCrMo/Si-DLC( $x\%O_2$ )/DLC system did not delaminate after 9 years immersion in PBS when  $x = 0.5$ . However at  $x = 2.0\%$ , substantial delamination occurred. Smaller delamination areas were observed when TiAlNb was used as the substrate.
- Accelerated reciprocating experiments could be correlated to long-term experiment, from a spinal disk simulator, via extrapolated Wöhler curves.

## Chapter 5 Discussion summary, overall conclusions and future work

## 5.1 Discussion summary and overall conclusions

This thesis work investigated the corrosion mechanisms affecting a DLC/substrate system. Corrosion initiation, propagation and failure was investigated by taking into account several aggravating factors affecting the interlayer/interface material, such as confined and crevice geometries, galvanic coupling, stress, and fatigue.

In the absence of aggravating factors (crevices, galvanic coupling, stress), corrosion initiation susceptibility of a deposited interlayer material could be successfully characterized by a three-step methodology in which the interlayer material was: i) revealed by wedge-milling a Ti/interlayer/DLC sample, ii) characterized by a multipoint-linescan with Auger electron spectroscopy (AES), and iii) electrochemically characterized with a microcapillary technique. AES surface characterization could successfully determine the compositional make-up of a wedge-milled interlayer, and metal carbides could be identified at the interlayer/DLC interface by comparison of different spectral peaks to published spectra. Local electrochemical characterization with a microcapillary ( $\mu\text{m}^2$  working area range) allowed for determination of the intrinsic reactivity of DLC, and of the wedge-milled interlayers. Further, by comparison with macro-electrochemical ( $\text{cm}^2$  working area range) polarization curves, it was found that the electrochemical response of a DLC coated surface was highly dependent on the size of the characterization area (from  $\text{cm}^2$  to  $\mu\text{m}^2$  scale), and varied substantially depending on the defect included in the area. Systematic local OCP measurements on the interlayers revealed that chromium carbide and Si-DLC were electrochemically stable interlayers (the measured OCP over 24 h was in the *stable-passive oxide* potential range) in HyClone® Wear Test Fluid (WTF), whereas Si corroded (indicative of a decreasing OCP towards the thermodynamic reversible potential domain for Si over 24 h).

The corrosion of Si was further accelerated when constricted in a confined geometry. Immersion experiments in a confined/crevice cell, at 37 °C and at elevated temperatures, showed increased corrosion rates on Si surfaces when compared to Si immersed in bulk (no confinement) solution. Corrosion enhancement in a confinement was very prominent in phosphate-containing solutions (0.01 M PBS and HyClone® WTF), and barely so in chloride-containing solution. A local pH increase, related to cathodic reaction evolution, was found to occur inside the confined cell on the corroded Si surface exposed to phosphate-containing solution, along with a decreasing OCP evolution down to the Si dissolution potential range (as evidenced in Si-H<sub>2</sub>O Pourbaix diagram). The corrosion product inside the confinement, characterized by XPS, was an inhomogeneous oxy-hydroxide layer over 400 nm in thickness (as compared to the 1 nm native oxide measured on the *as-received* Si and the 8 nm defective passive oxide in the crevice ). The Si corrosion rates of the long-term crevice immersion experiments could be correlated with temperature accelerated ones, presenting a linear Arrhenius relation in PBS and HyClone® WTF. Based on confined/crevice experiments performed with one Ti and on Si surface, galvanic coupling of Si with the Ti substrate slightly accelerated Si dissolution. However, the failure case of TiAlV/Si/DLC hip implants could be mainly attributed to crevice corrosion of the Si interlayer.

When a static load (induced by Rockwell indent) is applied on the TiAlV/Si/DLC system, DLC delamination was accelerated in phosphate-containing solution, as described in previous work [104]. In addition to the influence of the crevice generated at the interface, stress further accelerated dissolution of the Si interlayer. Considering the more stable Si-DLC interlayer (deposited from TMS gas), the presence of a static stress on the TiAlNb/Si-DLC/DLC system did not induce delamination after 1.7 years of immersion in PBS at 37°C. When the TiAlNb/Si-DLC interface was intentionally contaminated with up to 2.0 % O<sub>2</sub>, delamination still did not occur. These experiments will continue to be tracked in future work. However, in the CoCrMo/Si-DLC/DLC system, delamination of a 2.0% O<sub>2</sub> contaminated interface occurred after 2.5 years immersion in PBS at 37°C, but a 0.5% O<sub>2</sub> contaminated interface did not delaminate even after 9 years of immersion.

The influence of cyclic stress (fatigue) on the CoCrMo/Si-DLC/DLC system degradation in PBS was then investigated. Fatigue corrosion (CF) mechanisms of the interface were successfully derived by generating Wöhler curves (Critical load vs. number of cycles to delamination) from reciprocating experiments in PBS. The critical load required for delamination to occur around a pre-scratch on a coated sample was determined at a certain number of reciprocating cycles. Small oxygen contaminations (0.5 and 1.0%) at the CoCrMo/Si-DLC interface adversely affected the CF behavior by lowering the critical load and endurance limit. The accelerated wear experiments could further be correlated with long-term experiments previously performed on a CoCrMo/Si-DLC/DLC implant in a spinal disk simulator. By extrapolating the fitted Wöhler curves to a measured point representing the 0.5% O<sub>2</sub> contaminated spinal disk implant, which delaminated after ca. 5 million cycles, a correlation with the Si-DLC(0.5%) curve could be found. Conversely, the data point representing the 0.0% O<sub>2</sub> contaminated spinal disk implant, which did not show delamination after ca. 20 million cycles, therefore fell below the Si-DLC(0.0%) Wöhler curve.

As a final general conclusion, it can be stated that the investigations performed in this thesis work can be used to provide better estimations on the lifetime prediction of coated implants, helping the medical field prevent premature implant revision surgery. Moreover, the experimental methodologies developed can be applied to any hard-coated/substrate system used in aggressive environments (even mild polluted environmental conditions) and provide information to support better engineering of this interface.

## 5.2 Future work

Relating to the investigations of Chapter 2 and in order to address the question whether a reactively formed interface material of a few atomic rows (such as SiC at a Si/DLC interface) behaves the same as the material in bulk form, film analogs of the particular interface material should be deposited for further electrochemical characterization with the microcapillary. Additionally, small amounts of contaminants, such as oxygen, can be added to investigate what role these elements have on the electrochemical stability of the interface/interlayers, further developing the concepts in Chapter 4. Other interlayer materials such as Ta, Ti and TaN should also be characterized, especially in terms of the role of small amount of oxygen contaminants.

Whereas the chemical composition of an interface/interlayer was previously analyzed with AES or XPS, in combination with "wedged" or sputter depth profiling, analysis of non-sputtered interfaces by hard X-ray photoelectron spectroscopy (HAXPES) will be made available at Empa at the beginning of 2020. The X-rays used to probe the sample in HAXPES have higher energies, and can therefore penetrate deeper into the sample, allowing for the non-destructive analysis of a buried interlayer/interface. This is very beneficially, as it is still not completely understood how the chemical situation of a material is altered by sputter depth profiling with an ion beam.

Regarding the investigations of Chapter 3, the crevice cell used to monitor the corrosion propagation of Si should be further developed. Now that the cell has been successfully used to monitor crevice corrosion of bulk Si surfaces, it can be applied to deposited interface material analogs. The interlayer materials (Si, Ti, Cr, Si-DLC) can be deposited onto substrates (Ti, TiAlV, CoCrMo) and the OCP evolution of the deposited interlayer material can be monitored. As opposed to using POM clamps to secure the crevice, thin transparent plate clamps can be used so that the pH evolution across the confinement/crevice area can be visually tracked using adequate pH indicators. Another option is to track the pH evolution with micro pH probes, allowing for more precise real time monitoring of local chemistry changes across the confinement. With the implementation of thin transparent clamps, Raman and/or Ultraviolet-visible spectroscopy can also be utilized to track complex formation and chemical interactions on the surfaces in the confined liquid. This may clarify the exact role phosphate species have on the degradation of Si-based interlayers, as well as on the degradation of Si micro-electronic devices used in the body.

Another approach that was envisaged during the crevice investigations of Chapter 3 is the integration of a coated piezoelectric quartz plates coated with the interface materials within a confined electrochemical cell. The mass change evolution related to chemical reactions (dissolution, oxide formation) at the oxide/liquid interface of the coated material (an interlayer or interlayer/DLC) can be tracked in combination with the electrochemical current and potential evolution. This allows for the tracking of the early stages of passive oxide dissolution related to chemistry and pH changes. The technique allows for better resolution of corrosion initiation investigations. The confined cell incorporating a piezoelectric quartz has already been developed at Empa, and is in the calibration stages.

Continuing the investigations of Chapter 4, the reciprocating simulator experiments will be further developed to investigate the corrosion fatigue behavior of a buried interface. The fatigue influence of contaminated interfaces under alternating load was successfully investigated with the generation of Wöhler curves, now the corrosion influence must be further clarified. Although comparison of the delamination behavior of DLC in different electrolytes gave strong indication that the interface stability is highly dependent on the corrosive media, the role of the electrolyte must be further investigated by implementing more sensitive electrochemical detection concepts. This can be achieved by coupling a reciprocating wear test rig with a three-electrode electrochemical configuration. With this, the current and potential response can be monitored with each alternating load. Corrosion fatigue of a surface is characteristic of de-passivation/re-passivation transients in the current and potential response curves, due to the removal and rebuilding of the oxide layer with each wear cycle. Analogous monitoring should be possible when a coating (and therefore interface) is delaminating. Another question to clarify is to what extent the applied sliding frequency influences the corrosion fatigue behavior of the interface. In Chapter 4, the accelerated high frequency experiments were correlated to the semi-quantitative long-term (low frequency) experiments performed in a spinal disk simulator from previous work. In future work, more low frequency analog experiments should be conducted for comparison with high frequency experiments. Further, more experiments should be conducted at higher delamination cycles to achieve a more accurate fitting and extrapolation of the endurance limit. Cross-sectional analysis of the debonded interfaces should continuously be conducted after both high and low frequency experiments. Finally, to gain a better and quantitative understanding of the fatigue at the interface, a more systematic finite-element-analysis should be performed to understand the stress distribution the sliding counterpart is generating at the interface. A first attempt to simulate the stress at the interface near a defect is shown in Fig. 5.1. Compressive and tensile stresses are present around an intentionally introduced circular debonding area at the interface. The simulation must be reiterated more accurately with a finer mesh structure so that the stress distribution around the interface can be better resolved.

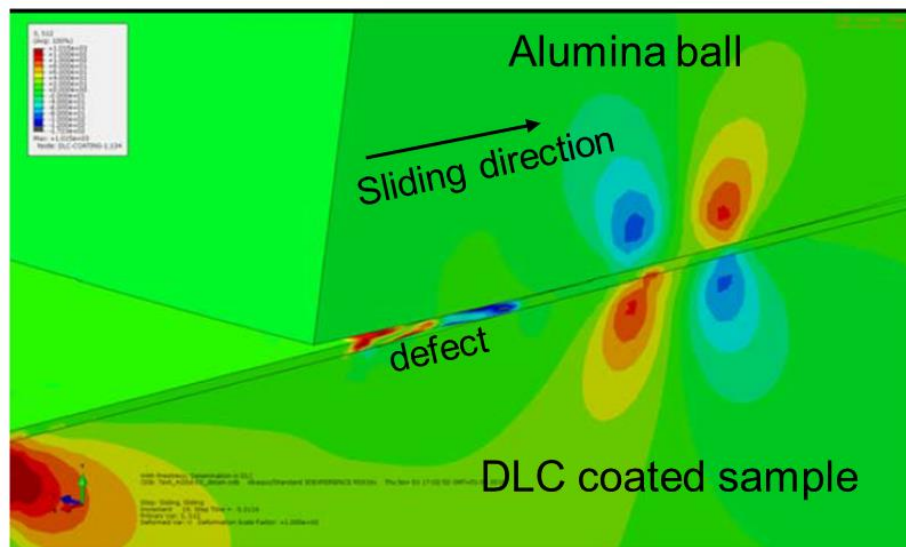


Fig. 5.1: Still frame from a video clip of a FEA on a defective interface. Compressive and tensile stresses are present around the deboning interface when a sliding load is applied on the coated surface (*Performed by Christian Affolter, Empa*).



# References

- [1] K. Holmberg, H. Ronkainen, A. Matthews, Tribology of thin coatings, *Ceram. Int.* 26 (2000) 787–795. doi:10.1016/S0272-8842(00)00015-8.
- [2] P. Hedenqvist, M. Olsson, P. Wallén, Å. Kassman, S. Hogmark, S. Jacobson, How TiN coatings improve the performance of high speed steel cutting tools, *Surf. Coatings Technol.* 41 (1990) 243–256. doi:10.1016/0257-8972(90)90172-9.
- [3] R. Hauert, K. Thorwarth, G. Thorwarth, An overview on diamond-like carbon coatings in medical applications, *Surf. Coatings Technol.* 233 (2013) 119–130. doi:10.1016/j.surfcoat.2013.04.015.
- [4] K. Bewilogua, G. Bräuer, A. Dietz, J. Gäbler, G. Goch, B. Karpuschewski, B. Szyszka, Surface technology for automotive engineering, *CIRP Ann. - Manuf. Technol.* 58 (2009) 608–627. doi:10.1016/j.cirp.2009.09.001.
- [5] C.P.O. Treutler, Industrial use of plasma-deposited coatings for components of automotive fuel injection systems, *Surf. Coatings Technol.* 200 (2005) 1969–1975. doi:10.1016/j.surfcoat.2005.08.012.
- [6] J. Robertson, Diamond-like amorphous carbon J., *Mater. Sci. Eng. R.* 216 (2010) 868–871. doi:10.1063/1.369293.
- [7] S. V. Hainsworth, N.J. Uhure, Diamond like carbon coatings for tribology: production techniques, characterisation methods and applications, *Int. Mater. Rev.* 52 (2007) 153–174. doi:10.1179/174328007x160272.
- [8] S. V. Hainsworth, N.J. Uhure, Diamond like carbon coatings for tribology: production techniques, characterisation methods and applications, *Int. Mater. Rev.* 52 (2007) 153–174. doi:10.1179/174328007X160272.
- [9] M. Sloan, A. Premkumar, N. Sheth, Projected Volume of Primary Total Joint Arthroplasty in the U.S., 2014 to 2030, *J. Bone Jt. Surg.* 100 (2018) 1455–1460.
- [10] N.I. and I. of M. National Joint Registry for England, Wales, 15th Annual Report 2018, 2017. doi:10.1038/nmat2505.
- [11] C.A. Love, R.B. Cook, T.J. Harvey, P.A. Dearnley, R.J.K. Wood, Diamond like carbon coatings for potential application in biological implants - A review, *Tribol. Int.* 63 (2013) 141–150. doi:10.1016/j.triboint.2012.09.006.
- [12] I. Milošev, CoCrMo Alloy for Biomedical Applications, in: S.S. Djokić (Ed.), *Biomed. Appl.*, Springer US, Boston, MA, 2012: pp. 1–72. doi:10.1007/978-1-4614-3125-1\_1.
- [13] Y. Abu-Amer, I. Darwech, J.C. Clohisy, Aseptic loosening of total joint replacements: Mechanisms underlying osteolysis and potential therapies, *Arthritis Res. Ther.* 9 (2007) 1–7. doi:10.1186/ar2170.
- [14] J. Drummond, P. Tran, C. Fary, Metal-on-Metal Hip Arthroplasty: A Review of Adverse Reactions and Patient Management, *J. Funct. Biomater.* 6 (2015) 486–499.

doi:10.3390/jfb6030486.

- [15] T.I.T. Okpalugo, A.A. Ogwu, DLC thin films for implantable medical devices, *Thin Film Coatings Biomater. Biomed. Appl.* (2016) 261–287. doi:10.1016/b978-1-78242-453-6.00011-0.
- [16] R. Hauert, DLC films in biomedical applications, *Tribol. Diamond-Like Carbon Film. Fundam. Appl.* (2008) 494–509. doi:10.1007/978-0-387-49891-1\_20.
- [17] G. Dearnaley, J.H. Arps, Biomedical applications of diamond-like carbon (DLC) coatings: A review, *Surf. Coatings Technol.* 200 (2005) 2518–2524. doi:10.1016/j.surfcoat.2005.07.077.
- [18] D. Sheeja, B.K. Tay, S.P. Lau, L.N. Nung, Tribological characterisation of diamond-like carbon coatings on Co-Cr-Mo alloy for orthopaedic applications, *Surf. Coatings Technol.* 146–147 (2001) 410–416. doi:10.1016/S0257-8972(01)01425-6.
- [19] R. Lappalainen, H. Heinonen, A. Anttila, S. Santavirta, Some relevant issues related to the use of amorphous diamond coatings for medical applications, *Diam. Relat. Mater.* 7 (2002) 482–485. doi:10.1016/s0925-9635(98)80003-4.
- [20] B. Shi, O.O. Ajayi, G. Fenske, A. Erdemir, H. Liang, Tribological performance of some alternative bearing materials for artificial joints, *Wear.* 255 (2003) 1015–1021. doi:10.1016/S0043-1648(03)00276-X.
- [21] T. Xu, L. Pruitt, Diamond-like carbon coatings for orthopaedic applications: An evaluation of tribological performance, *J. Mater. Sci. Mater. Med.* 10 (1999) 83–90. doi:10.1023/A:1008916903171.
- [22] H. Dong, W. Shi, T. Bell, Potential of improving tribological performance of UHMWPE by engineering the Ti6Al4V counterfaces, *Wear.* 225–229 (1999) 146–153. doi:10.1016/S0043-1648(98)00356-1.
- [23] V.M. Tiainen, Amorphous carbon as a bio-mechanical coating-mechanical properties and biological applications, *Diam. Relat. Mater.* 10 (2001) 153–160. doi:10.1016/S0925-9635(00)00462-3.
- [24] R. Lappalainen, M. Selenius, A. Anttila, Y.T. Konttinen, S.S. Santavirta, Reduction of Wear in Total Hip Replacement Prostheses by Amorphous Diamond Coatings, *J. Biomed. Mater. Res. - Part B Appl. Biomater.* 66 (2003) 410–413. doi:10.1002/jbm.b.10026.
- [25] J. Fisher, X.Q. Hu, T.D. Stewart, S. Williams, J.L. Tipper, E. Ingham, M.H. Stone, C. Davies, P. Hatto, J. Bolton, M. Riley, C. Hardaker, G.H. Isaac, G. Berry, Wear of surface engineered metal-on-metal hip prostheses, *J. Mater. Sci. Mater. Med.* 15 (2004) 225–235. doi:10.1023/B:JMSM.0000015482.24542.76.
- [26] D.P. Dowling, P.V. Kola, K. Donnelly, T.C. Kelly, K. Brumitt, L. Lloyd, R. Eloy, M. Therin, N. Weill, Evaluation of diamond-like carbon-coated orthopaedic implants, *Diam. Relat. Mater.* 6 (2002) 390–393. doi:10.1016/s0925-9635(96)00687-5.
- [27] S. Affatato, M. Frigo, A. Toni, An in vitro investigation of diamond-like carbon as a femoral head coating, *J. Biomed. Mater. Res.* 53 (2000) 221–226. doi:10.1002/(SICI)1097-4636(2000)53:3<221::AID-JBM6>3.0.CO;2-Z.

- [28] V. Saikko, T. Ahlroos, O. Caloniuss, J. Keränen, Wear simulation of total hip prostheses with polyethylene against CoCr, alumina and diamond-like carbon, *Biomaterials*. 22 (2001) 1507–1514. doi:10.1016/S0142-9612(00)00306-9.
- [29] G. Taeger, L.E. Podleska, B. Schmidt, M. Ziegler, D. Nast-Kolb, Comparison of Diamond-Like-Carbon and Alumina-Oxide articulating with Polyethylene in Total Hip Arthroplasty, *Materwiss. Werksttech*. 34 (2003) 1094–1100. doi:10.1002/mawe.200300717.
- [30] T.J. Joyce, Examination of failed ex vivo metal-on-metal metatarsophalangeal prosthesis and comparison with theoretically determined lubrication regimes, 263 (2007) 1050–1054. doi:10.1016/j.wear.2006.11.045.
- [31] R. Hauert, G. Thorwarth, U. Müller, M. Stiefel, C. V. Falub, K. Thorwarth, T.J. Joyce, Analysis of the in-vivo failure of the adhesive interlayer for a DLC coated articulating metatarsophalangeal joint, *Diam. Relat. Mater.* 25 (2012) 34–39. doi:10.1016/j.diamond.2012.02.001.
- [32] M. Yatsuzuka, J. Tateiwa, H. Uchida, Evaluation of pinhole defect in DLC film prepared by hybrid process of plasma-based ion implantation and deposition, *Vacuum*. 80 (2006) 1351–1355. doi:10.1016/j.vacuum.2006.01.069.
- [33] L. Chandra, M. Allen, R. Butter, N. Rushton, A.. Lettington, T.. Clyne, The effect of exposure to biological fluids on the spallation resistance of diamond-like carbon coatings on metallic substrates, *J. Mater. Sci.* 6 (1995) 581–589.
- [34] K.A. Pischow, L. Eriksson, E. Harju, A.S. Korhonen, E.O. Ristolainen, The influence of titanium interlayers on the adhesion of PVD TiN coatings on oxidized stainless steel substrates, *Surf. Coatings Technol.* 58 (1993) 163–172. doi:10.1016/0257-8972(93)90003-7.
- [35] W. Tillmann, A. Fehr, D. Stangier, M. Dildrop, Influences of substrate pretreatments and Ti/Cr interlayers on the adhesion and hardness of CrAlSiN and TiAlSiN films deposited on Al<sub>2</sub>O<sub>3</sub> and ZrO<sub>2</sub>-8Y<sub>2</sub>O<sub>3</sub> thermal barrier coatings, *Results Phys.* 12 (2019) 2206–2212. doi:10.1016/j.rinp.2019.02.048.
- [36] B. Rother, T. Lunow, G. Leonhardt, Interface strength of titanium nitride coatings on hardened high-speed steel, *Surf. Coatings Technol.* 71 (1995) 229–232. doi:10.1016/0257-8972(94)02317-J.
- [37] C.C. Chen, F.C.N. Hong, Interfacial studies for improving the adhesion of diamond-like carbon films on steel, *Appl. Surf. Sci.* 243 (2005) 296–303. doi:10.1016/j.apsusc.2004.09.085.
- [38] Y. Xiang, Y. Liu, W. Cheng-biao, L. Xin-chun, Y. De-yang, Investigation on preparation and properties of thick DLC film in medium-frequency dual-magnetron sputtering, *Vacuum*. 80 (2005) 324–331. doi:10.1016/j.vacuum.2005.06.002.
- [39] R. Maiti, R. Mills, Wear properties of diamond-like carbon coatings with silicon and chromium as adhesion layer using a high frequency reciprocating rig, *J. Eng. Tribol.* 231 (2017) 1605–1615. doi:10.1177/1350650117704788.
- [40] L.F. Bonetti, G. Capote, L. V Santos, E.J. Corat, V.J. Trava-Airoldi, Adhesion studies of diamond-like carbon films deposited on Ti6Al4V substrate with a silicon interlayer, *Thin Solid Films*. 515

- (2006) 375–379. doi:10.1016/j.tsf.2005.12.154.
- [41] S. V Hattangady, M.J. Mantini, G.G. Fountain, R.A. Rudder, R.J. Markunas, The role of an ultrathin silicon interlayer at the SiO<sub>2</sub>-Ge interface, *J. Appl. Phys.* 71 (1992) 3842–3852. doi:10.1063/1.350874.
- [42] A.E.J. Lim, T.Y. Liow, K.K. Chen, R.P.C. Tern, G.Q. Lo, Novel epitaxial silicon interlayer for junction engineering in aggressively-scaled germanium photodetectors, *AIP Adv.* 3 (2013) 1–6. doi:10.1063/1.4821118.
- [43] P.D. Maguire, J.A. McLaughlin, T.I.T. Okpalugo, P. Lemoine, P. Papakonstantinou, E.T. McAdams, M. Needham, A.A. Ogwu, M. Ball, G.A. Abbas, Mechanical stability, corrosion performance and bioresponse of amorphous diamond-like carbon for medical stents and guidewires, *Diam. Relat. Mater.* 14 (2005) 1277–1288. doi:10.1016/j.diamond.2004.12.023.
- [44] I. Kucuk, C. Sarioglu, Pitting corrosion of TiN-coated stainless steel in 3 % NaCl solution, *Mater. Technol.* 49 (2015) 183–192. doi:10.17222/mit.2013.176.
- [45] L. Joska, J. Fojt, O. Mestek, L. Cvrcek, V. Brezina, The effect of a DLC coating adhesion layer on the corrosion behavior of titanium and the Ti6Al4V alloy for dental implants, *Surf. Coatings Technol.* 206 (2012) 4899–4906. doi:10.1016/j.surfcoat.2012.05.089.
- [46] M. Azzi, P. Amirault, M. Paquette, J.E. Klemberg-Sapieha, L. Martinu, Corrosion performance and mechanical stability of 316L/DLC coating system: Role of interlayers, *Surf. Coatings Technol.* 204 (2010) 3986–3994. doi:10.1016/j.surfcoat.2010.05.004.
- [47] Y. Massiani, A. Medjahed, P. Gravier, J.P. Crousier, Effect of a titanium underlayer on the corrosion behaviour of physically vapour deposited titanium nitride films, *Thin Solid Films.* 217 (1992) 31–37. doi:10.1016/0040-6090(92)90602-8.
- [48] B. Matthes, E. Broszeit, J. Aromaa, H. Ronkainen, S.P. Hannula, A. Leyland, A. Matthews, Corrosion performance of some titanium-based hard coatings, *Surf. Coatings Technol.* 49 (1991) 489–495. doi:10.1016/0257-8972(91)90105-6.
- [49] H.A. Jehn, M.E. Baumgärtner, Corrosion studies with hard coating-substrate systems, *Surf. Coatings Technol.* 54/55 (1992) 108–114. doi:10.1016/S0257-8972(09)90036-6.
- [50] D.. Jones, *Principles and Prevention of Corrosion*, 2nd ed., Prentice-Hall, Inc., Upper Saddle River, NJ, 1996.
- [51] D. Landolt, *Corrosion and surface Chemistry of Metals*, 1st ed., EPFL Press, Lausanne, 2007.
- [52] D.B. Lewis, S.J. Creasey, C. Wüstefeld, A.P. Ehasarian, P.E. Hovsepian, The role of the growth defects on the corrosion resistance of CrN/NbN superlattice coatings deposited at low temperatures, *Thin Solid Films.* 503 (2006) 143–148. doi:10.1016/j.tsf.2005.08.375.
- [53] A.S. Hamdy Makhoulouf, *Intelligent Stannate-Based Coatings of Self-Healing Functionality for Magnesium Alloys*, Elsevier Inc., 2014. doi:10.1016/B978-0-12-411467-8.00015-5.
- [54] C. Vargel, Galvanic corrosion, in: C. Vargel (Ed.), *Corros. Alum.*, Elsevier, 2004: pp. 149–164.
- [55] H.A. Jehn, Improvement of the corrosion resistance of PVD hard coating-substrate systems,

- Surf. Coatings Technol. 125 (2000) 212–217. doi:10.1016/S0257-8972(99)00551-4.
- [56] H.A. Jehn, P. Schaller, Corrosion of hard coatings. part 2-results of the study and coating properties, *Galvanotechnik*. 84 (1993) 3669–3675.
- [57] R.. Jones, R.. Ricker, Mechanisms of Stress-corrosion Cracking, in: R.. Jones (Ed.), *Stress Corros. Crack. Mater. Perform. Eval.*, ASM International, 1992: pp. 1–40. doi:10.1016/B978-0-08-052351-4.50064-9.
- [58] A.C.U. RAO, V. VASU, M. GOVINDARAJU, K.V.S. SRINADH, Stress corrosion cracking behaviour of 7xxx aluminum alloys: A literature review, *Trans. Nonferrous Met. Soc. China (English Ed.* 26 (2016) 1447–1471. doi:10.1016/S1003-6326(16)64220-6.
- [59] R.H. Dauskardt, M. Lane, Q. Ma, N. Krishna, Adhesion and debonding of multi-layer thin film structures, *Eng. Fract. Mech.* 61 (1998) 141–162. doi:10.1016/S0013-7944(98)00052-6.
- [60] M.W. Lane, J.M. Snodgrass, R.H. Dauskardt, Environmental Effects on Interfacial Adhesion, *Microelectron. Reliab.* 41 (2001) 1615–1624. doi:10.1016/S0026-2714(01)00150-0.
- [61] X.L. Peng, T.W. Clyne, Residual stress and debonding of DLC films on metallic substrates, *Diam. Relat. Mater.* 7 (1998) 944–950. doi:10.1016/S0925-9635(97)00331-2.
- [62] X.L. Peng, T.W. Clyne, Mechanical stability of DLC films on metallic substrates Part II - Interfacial toughness, debonding and blistering, *Thin Solid Films*. 312 (1998) 219–227. doi:10.1016/S0040-6090(97)00703-7.
- [63] C. Weissmantel, Preparation, structure, and properties of hard coatings on the basis of i-C and i-BN, *Thin Film. from Free Atoms Part.* (n.d.).
- [64] M.. Drory, J.. Hutchinson, Measurement of the adhesion of a brittle film on a ductile substrate by indentation, *R. Soc.* 452 (1996) 2319–2341.
- [65] D. Bernoulli, A. Wyss, R. Raghavan, K. Thorwarth, R. Hauert, R. Spolenak, Contact damage of hard and brittle thin films on ductile metallic substrates: an analysis of diamond-like carbon on titanium substrates, *Acta Mater.* 83 (2015) 29–36. doi:10.1016/j.actamat.2014.09.044.
- [66] C.V. Falub, G. Thorwarth, C. Affolter, U. Müller, C. Voisard, R. Hauert, A quantitative in vitro method to predict the adhesion lifetime of diamond-like carbon thin films on biomedical implants, *Acta Biomater.* 5 (2009) 3086–3097. doi:10.1016/j.actbio.2009.05.009.
- [67] C. V. Falub, U. Müller, G. Thorwarth, M. Parlinska-Wojtan, C. Voisard, R. Hauert, In vitro studies of the adhesion of diamond-like carbon thin films on CoCrMo biomedical implant alloy, *Acta Mater.* 59 (2011) 4678–4689. doi:10.1016/j.actamat.2011.04.014.
- [68] U. Müller, C. V. Falub, G. Thorwarth, C. Voisard, R. Hauert, Diamond-like carbon coatings on a CoCrMo implant alloy: A detailed XPS analysis of the chemical states at the interface, *Acta Mater.* 59 (2011) 1150–1161. doi:10.1016/j.actamat.2010.10.048.
- [69] Y. Oka, M. Nishijima, K. Hiraga, M. Yatsuzuka, STEM observation of nano-interface between substrate and DLC film prepared by plasma-based ion implantation and deposition, *Nucl. Instruments Methods Phys. Res. Sect. B-Beam Interact. with Mater. Atoms.* 257 (2007) 702–

705. doi:DOI 10.1016/j.nimb.2007.02.083.

- [70] D. Bernoulli, A. Rico, A. Wyss, K. Thorwarth, J.P. Best, R. Hauert, R. Spolenak, Improved contact damage resistance of hydrogenated diamond-like carbon (DLC) with a ductile  $\alpha$ -Ta interlayer, *Diam. Relat. Mater.* 58 (2015) 78–83. doi:10.1016/j.diamond.2015.06.006.
- [71] K. Komai, Corrosion Fatigue, in: I. Milne, R.. Ritchie, B. Karihaloo (Eds.), *Compr. Struct. Integr.*, Elsevier, 2003: pp. 346–358.
- [72] J.W. Hutchinson, M.Y. He, A.G. Evans, Influence of imperfections on the nucleation and propagation of buckling driven delaminations, *J. Mech. Phys. Solids.* 48 (2000) 709–734. doi:10.1016/S0022-5096(99)00050-2.
- [73] H.H. Yu, M.Y. He, J.W. Hutchinson, Edge effects in thin film delamination, *Acta Mater.* 49 (2001) 93–107. doi:10.1016/S1359-6454(00)00293-7.
- [74] Z.H. Xie, R. Singh, A. Bendavid, P.J. Martin, P.R. Munroe, M. Hoffman, Contact damage evolution in a diamond-like carbon (DLC) coating on a stainless steel substrate, *Thin Solid Films.* 515 (2007) 3196–3201. doi:10.1016/j.tsf.2006.01.035.
- [75] M.H. Staia, E.S. Puchi-Cabrera, A. Iost, E. Carrasquero, Y.Y. Santana Mendez, J.G. La Barbera Sosa, D. Chicot, A. Van Gorp, Sliding wear of a-C:H coatings against alumina in corrosive media, *Diam. Relat. Mater.* 38 (2013) 139–147. doi:10.1016/j.diamond.2013.06.020.
- [76] H. Li, T. Xu, C. Wang, J. Chen, H. Zhou, H. Liu, Tribochemical effects on the friction and wear behaviors of a-C:H and a-C films in different environment, *Tribol. Int.* 40 (2007) 132–138. doi:10.1016/j.triboint.2006.03.007.
- [77] H. Ronkainen, S. Varjus, K. Holmberg, Tribological performance of different DLC coatings in water-lubricated conditions, *Wear.* 249 (2001) 267–271. doi:10.1016/S0043-1648(01)00561-0.
- [78] J.W. Yi, S.J. Park, M.W. Moon, K.R. Lee, S.S. Kim, Defect effect on tribological behavior of diamond-like carbon films deposited with hydrogen diluted benzene gas in aqueous environment, *Appl. Surf. Sci.* 255 (2009) 7005–7011. doi:10.1016/j.apsusc.2009.03.031.
- [79] J. Stallard, D. Mercks, M. Jarratt, D.G. Teer, P.H. Shipway, A study of the tribological behaviour of three carbon-based coatings, tested in air, water and oil environments at high loads, *Surf. Coatings Technol.* 177–178 (2004) 545–551. doi:10.1016/S0257-8972(03)00925-3.
- [80] T.M. Manhabosco, A.P.M. Barboza, R.J.C. Batista, B.R.A. Neves, I.L. Müller, Corrosion, wear and wear–corrosion behavior of graphite-like a-C:H films deposited on bare and nitrided titanium alloy, *Diam. Relat. Mater.* 31 (2013) 58–64. doi:10.1016/j.diamond.2012.11.005.
- [81] S.J. Park, K.R. Lee, D.H. Ko, Tribochemical reaction of hydrogenated diamond-like carbon films: A clue to understand the environmental dependence, *Tribol. Int.* 37 (2004) 913–921. doi:10.1016/j.triboint.2004.07.008.
- [82] S.J. Park, K.R. Lee, S.H. Ahn, J.G. Kim, Instability of diamond-like carbon (DLC) films during sliding in aqueous environment, *Diam. Relat. Mater.* 17 (2008) 247–251. doi:10.1016/j.diamond.2007.12.035.

- [83] K. Thorwarth, G. Thorwarth, R. Figi, B. Weisse, M. Stiefel, R. Hauert, On interlayer stability and high-cycle simulator performance of diamond-like carbon layers for articulating joint replacements, *Int. J. Mol. Sci.* 15 (2014) 10527–10540. doi:10.3390/ijms150610527.
- [84] G. Thorwarth, C. V. Falub, U. Müller, B. Weisse, C. Voisard, M. Tobler, R. Hauert, Tribological behavior of DLC-coated articulating joint implants, *Acta Biomater.* 6 (2010) 2335–2341. doi:10.1016/j.actbio.2009.12.019.
- [85] E. Ilic, A. Pardo, T. Suter, S. Mischler, P. Schmutz, R. Hauert, A methodology for characterizing the electrochemical stability of DLC coated interlayers and interfaces, *Surf. Coatings Technol.* 375 (2019) 402–413. doi:10.1016/j.surfcoat.2019.07.055.
- [86] R.P. Gunawardane, C.R. Arumainayagam, Chapter 10. Auger electron spectroscopy, in: D.R. Vij (Ed.), *Handb. Appl. Solid State Spectrosc.*, Springer, New York, 2006. doi:10.1039/pc9838000327.
- [87] M.A. Smith, L.L. Levenson, Final-state effects in carbon Auger spectra of transition-metal carbides, *Phys. Rev. B.* 16 (1977) 1365–1369.
- [88] T. Suter, H. Böhni, The Microcell Technique, in: *Anal. Methods Corros. Sci. Eng.*, 2006: pp. 649–696. doi:10.1201/9781420028331.ch17.
- [89] E. Deltombe, M. Pourbaix, Colbalt, in: M. Pourbaix (Ed.), *Atlas Electrochem. Equilibria Aqueous Solut.*, 2nd ed., NACE, Houston, 1974: pp. 322–329.
- [90] E. Deltombe, N. Zoubov, M. Pourbaix, Chromium, in: M. Pourbaix (Ed.), *Atlas Electrochem. Equilibria Aqueous Solut.*, 2nd ed., NACE, Houston, 1974: pp. 256–271.
- [91] J. V Muijder, Carbon, in: M. Pourbaix (Ed.), *Atlas Electrochem. Equilibria Aqueous Solut.*, 2nd ed., NACE, Houston, 1974: pp. 449–457.
- [92] L. Joska, J. Fojt, L. Cvrcek, V. Brezina, Properties of titanium-alloyed DLC layers for medical applications, *Biomater.* 4 (2014) 1–7. doi:10.4161/biom.29505.
- [93] R. Hauert, J. Patscheider, R. Zehringer, M. Tobler, Analysis of a-C:H superhard coatings by scanning Auger microscope and target factor analysis, *Thin Solid Films.* 206 (1991) 330–334. doi:10.1016/0040-6090(91)90445-4.
- [94] R. Kosiba, J. Liday, G. Ecke, O. Ambacher, J. Breza, P. Vogrinčič, Quantitative Auger electron spectroscopy of SiC, *Vacuum.* 80 (2006) 990–995. doi:10.1016/j.vacuum.2006.01.003.
- [95] L. Pankratz, Thermodynamic properties of carbides, nitrides, and other selected substances, *U. S. Dep. Inter. Bur. Mines. Bulletin* 6 (1994).
- [96] M. Maline, M. Ducarroir, F. Teyssandier, R. Hillel, R. Berjoan, F.J.J. Van Loo, W. Wakelkamp, Auger electron spectroscopy of compounds in the Si-Ti-C system, *Surf. Sci.* 286 (1993) 82–91. doi:10.1201/9780203741528-5.
- [97] S.R. Shatynski, The thermochemistry of transition metal carbides, *Oxid. Met.* 13 (1979) 105–118. doi:10.1007/BF00611975.
- [98] S.A. Catledge, R. Vaid, P. Diggins IV, J.J. Weimer, M. Koopman, Y.K. Vohra, Improved adhesion

- of ultra-hard carbon films on cobalt– chromium orthopaedic implant alloy, *J. Mater. Sci. Mater. Med.* 22 (2011) 307–316. doi:10.1007/s10856-010-4207-1.Improved.
- [99] X. Chen, J. Narayan, Effect of the chemical nature of transition-metal substrates on chemical-vapor deposition of diamond, *J. Appl. Phys.* 74 (1993) 4168–4173. doi:10.1063/1.354420.
- [100] A. Pardo, E. Ilic, K. Thorwarth, M. Stiefel, R. Hauert, Corrosion fatigue in DLC-coated articulating implants: an accelerated methodology to predict realistic interface lifetime, *Sci. Technol. Adv. Mater.* 20 (2019) 173–186. doi:10.1080/14686996.2019.1580483.
- [101] E. Ilic, A. Pardo, R. Hauert, P. Schmutz, S. Mischler, Silicon Corrosion in Neutral Media: The Influence of Confined Geometries and Crevice Corrosion in Simulated Physiological Solutions, *J. Electrochem. Soc.* 166 (2019) C125–C133. doi:10.1149/2.0241906jes.
- [102] J. Van Muylder, J. Besson, W. Kunz, M. Pourbaix, Silicon, in: M. Pourbaix (Ed.), *Atlas Electrochem. Equilibria Aqueous Solut.*, 2nd ed., NACE, Houston, 1974: pp. 459–463.
- [103] W. Van Gelder, V.E. Hauser, The Etching of Silicon Nitride in Phosphoric Acid with Silicon Dioxide as a Mask, *J. Electrochem. Soc.* 114 (1967) 869. doi:10.1149/1.2426757.
- [104] R. Hauert, C. V. Falub, G. Thorwarth, K. Thorwarth, C. Affolter, M. Stiefel, L.E. Podleska, G. Taeger, Retrospective lifetime estimation of failed and explanted diamond-like carbon coated hip joint balls, *Acta Biomater.* 8 (2012) 3170–3176. doi:10.1016/j.actbio.2012.04.016.
- [105] R. Butter, M. Allen, L. Chandra, A.H. Lettington, N. Rushton, In vitro studies of DLC coatings with silicon intermediate layer, *Diam. Relat. Mater.* 4 (1995) 857–861. doi:10.1016/0925-9635(94)05280-8.
- [106] D.J. Edell, *Neuroprosthetics: Theory and Practice*, 2nd ed., Utah, 2014.
- [107] E. Fernandez, R. Normann, *Introduction to Visual Prostheses*, Salt Lake City (UT), 2016. doi:NBK391004 [bookaccession].
- [108] A. Vanhoestenbergh, N. Donaldson, Corrosion of silicon integrated circuits and lifetime predictions in implantable, *J. Neural Eng.* 10 (2013) 13. doi:10.1088/1741-2560/10/3/031002.
- [109] J.C. Barrese, J. Aceros, J.P. Donoghue, R. Island, R. Island, Intracortical Microelectrode Arrays in Non-Human Primates, *J. Neural Eng.* 13 (2016) 27. doi:10.1088/1741-2560/13/2/026003.Scanning.
- [110] H. Hämmerle, K. Kobuch, K. Kohler, W. Nisch, H. Sachs, M. Stelzle, Biostability of micro-photodiode arrays for subretinal implantation, *Biomaterials.* 23 (2002) 797–804. doi:10.1016/S0142-9612(01)00185-5.
- [111] D.J. Edell, D. Drive, E. Suite, Insulating Biomaterials Research for Implantable Microelectronic Devices, in: *Mater. Res. Soc. Symp. Proc.*, 2013: p. N1.9.1-12.
- [112] J. Morales, J. Souriau, G. Simon, Corrosion Protection of Silicon Micro Systems with Ultra-Thin Barrier Films for Miniaturized Medical Devices, *ECS Trans.* 69 (2015) 9–26.
- [113] J.M. Maloney, S.A. Lipka, S.P. Baldwin, In Vivo Biostability of CVD Silicon Oxide and Silicon Nitride Films, in: *Mater. Res. Soc. Symp. Proc.*, 2005: p. J14.3.1-6.



- [114] M. Fröhlich, M. Birkholz, K.E. Ehwald, P. Kulse, O. Fursenko, J. Katzer, Biostability of an implantable glucose sensor chip, in: IOP Conf. Ser. Mater. Sci. Eng., 2012: p. 012022. doi:10.1088/1757-899X/41/1/012022.
- [115] A.W. Bott, Electrochemistry of Semiconductors, Curr. Sep. 17 (1998) 87–91.
- [116] Krishnan Rajeshwar, Fundamentals of Semiconductor Electrochemistry and Photoelectrochemistry, Encycl. Electrochem. (2007). doi:10.1002/9783527610426.bard060001.
- [117] G. Karlberg, G. Wranglen, On the mechanism of crevice corrosion of stainless Cr steels, Corros. Sci. 11 (1971) 499–510. doi:10.1016/S0010-938X(71)80017-3.
- [118] M. Pourbaix, N. Zoubov, Iron, in: M. Pourbaix (Ed.), Atlas Electrochem. Equilibria Aqueous Solut., 2nd ed., NACE, Houston, 1974: pp. 307–321.
- [119] O. Powell, H.B. Harrison, Anisotropic etching of {100} and {110} planes in {100}, J. Micromechanics Microengineering. 11 (2001) 217.
- [120] H. Seidel, Anisotropic Etching of Crystalline Silicon in Alkaline Solutions, J. Electrochem. Soc. 137 (1990) 3612. doi:10.1149/1.2086278.
- [121] P. Hinsinger, Bioavailability of soil inorganic P in the rhizosphere as affected by root-induced chemical changes: a review, Plant Soil. 137 (2001) 173–195.
- [122] W.R. Thurber, R.L. Mattis, Y.M. Liu, J.J. Filliben, Semiconductor measurement technology: The relationship between resistivity and dopant density for phosphorus and boron doped silicon., Washington, 1981.
- [123] C.A. Zorman, M. Mehregany, MEMS: Design and fabrication, in: M. Gad-el-Hak (Ed.), MEMS Handbook. MEMS Des. Fabr., 2nd ed., Taylor & Francis Group, 2006: pp. 1–3. doi:10.1201/9781420036565.
- [124] A. Bogh, J. Electrochem. Soc., 118 (1971) 401.
- [125] J.B. Price, H.R. Huff, R.R. Burgess, in: Semicond. Silicon, The Electrochemical Society Softbound Symposium, Princeton, N.J., 1973: p. 339.
- [126] M.P. Seah, S.J. Spencer, F. Bensebaa, I. Vickridge, H. Danzebrink, M. Krumrey, T. Gross, W. Oesterle, E. Wendler, B. Rheinländer, Y. Azuma, I. Kojima, N. Suzuki, M. Suzuki, S. Tanuma, D.W. Moon, H.J. Lee, H.M. Cho, H.Y. Chen, A.T.S. Wee, T. Osipowicz, J.S. Pan, W.A. Jordaan, R. Hauert, U. Klotz, C. van der Marel, M. Verheijen, Y. Tamminga, C. Jeynes, P. Bailey, S. Biswas, U. Falke, N. V. Nguyen, D. Chandler-Horowitz, J.R. Ehrstein, D. Muller, J.A. Dura, Critical review of the current status of thickness measurements for ultrathin SiO<sub>2</sub> on Si Part V: Results of a CCQM pilot study, Surf. Interface Anal. 36 (2004) 1269–1303. doi:10.1002/sia.1909.
- [127] X.G. Zhang, Electrochemistry of silicon and its oxide, Kluwer Academic/Plenum Publishers, New York, 2001. doi:10.1007/s10008-003-0371-2.
- [128] S.H. Teoh, Fatigue of biomaterials: A review, Int. J. Fatigue. 22 (2000) 825–837.

doi:10.1016/S0142-1123(00)00052-9.

- [129] C.E. Stromeyer, The Determination of Fatigue Limits under Alternating Stress Conditions, *Proc. R. Soc. A.* 90 (1914) 411–425. <https://doi.org/10.1098/rspa.1914.0066>.
- [130] E.S. Park, Understanding of the Shear Bands in Amorphous Metals, *Appl. Microsc.* 45 (2015) 63–73. doi:10.9729/am.2015.45.2.63.

# Curriculum Vitae

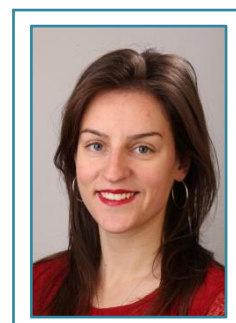
## EMILIJA ILIC

Date of Birth: Sept. 5, 1990

Place of Birth: Sarajevo, Bosnia and Herzegovina

Citizenship: Canadian (since 1995)

ema.ilic90@gmail.com



---

## SKILLS SUMMARY

- Strong background in electrochemistry, corrosion, and materials science
- Practical knowledge with electrochemical characterization techniques and equipment
- Excellent analytical, problem solving, and organizational skills developed while working as a research scientist at various institutes
- Excellent oral and written communication skills developed while interacting with customers and vendors during employment at IBM and Toyota

---

## EDUCATION

### PhD | Empa – Swiss Laboratories for Materials Science and Technology

Dübendorf, Switzerland | Sept 2015– Sept 2019)

- Developed and implemented methodologies and experimental protocols for assessing corrosion process at a coating/substrate interface
- Conducting crevice corrosion, stress corrosion cracking and tribology experiments to characterize the behavior of DLC coatings on TiAlV and CoCrMo articulating implants in physiological electrolytes

### MASc in Applied Chemistry and Chemical Engineering | University of Toronto

Toronto, Canada | Sept 2013–Aug 2015

- Investigated the corrosion of copper in anaerobic saline solutions for the development of resistant vessels for the long-term storage of nuclear waste in deep geological repositories
- Implemented hydrogen evolution measurements for calculating copper corrosion rate
- Research used by the Nuclear Waste Management Organization of Canada

### BASc in Chemical Engineering Co-op Program | University of Waterloo

Waterloo, Canada | Sept 2008–Apr 2013

---

## EMPLOYMENT HISTORY

### Research Intern | Empa – Swiss Laboratories for Materials Science and Technology

Dübendorf, Switzerland | May–Aug 2012

- Investigated the passivation of Al-Cr-Fe complex metallic alloys in highly acidic electrolytes
- Generated polarization measurements and preformed XPS depth profiling of their oxides

- Investigated the influence of crevice/pitting corrosion in confined electrochemical cells with/without solution exchange pump

#### Research Intern | Dalhousie University

Halifax, Canada | Sept–Dec 2011

- Collaborated with Ocean Nutrition Canada to establish a protocol for adhering edible coatings onto fish oil capsules
- Wrote technical reports and grant proposals for government funding of the project

#### Engineer Intern | Toyota Motor Manufacturing Canada

Cambridge, Canada | Jan–Apr 2011

- Collaborated with internal and external vendors and contractors to resolve mechanical problems
- Managed Kaizen projects between internal engineering, maintenance, ergonomics and safety departments

#### Web Sales Representative Intern | IBM

Stuttgart, Germany | May–Aug 2010

- Developed websites and online teamrooms for internal collaborations
- Identified customer requirements for the development of customized software

#### Research Intern | Institut Européen des Membranes

Montpellier, France | Jan–Apr 2010

- Synthesized membranes grafted with photochromic polymers to control pore size
- Designed and created device capable of accurately measuring the permeability of polymer membranes

---

## PUBLICATIONS

- E. Ilic, A. Pardo, T. Suter, S. Mischler, P. Schmutz, R. Hauert, A methodology for characterizing the electrochemical stability of DLC coated interlayers and interfaces, *Surf. Coatings Technol.* 375 (2019) 402–413.
- E. Ilic, A. Pardo, R. Hauert, P. Schmutz, S. Mischler, Silicon Corrosion in Neutral Media: The Influence of Confined Geometries and Crevice Corrosion in Simulated Physiological Solutions, *J. Electrochem. Soc.* 166 (2019) C125–C133.
- A. Pardo, E. Ilic, K. Thorwarth, M. Stiefel, R. Hauert, Corrosion fatigue in DLC-coated articulating implants: an accelerated methodology to predict realistic interface lifetime, *Sci. Technol. Adv. Mater.* 20 (2019) 173–186.
- E. Ilic, A. Pardo, R. Hauert, P. Schmutz, S. Mischler, Delayed delamination mechanisms of DLC coatings on articulating implants, in: *eCM Online Periodical, Collection. 1; Meet the Expert Implants Conference Abstracts*, AO Foundation, Olten, 2019: p. P2.
- E. Ilic, A. Pardo, R. Hauert, P. Schmutz, S. Mischler, Lifetime Estimation of Coated Articulating Implants: accelerated testing to address crevice, stress and fatigue corrosion, in: *eCM Online Periodical, Collection. 1; Meet the Expert Implants Conference Abstracts*, AO Foundation, Olten, 2018: p. P1.

- R. Hauert, E. Ilic, A. Pardo, P. Schmutz, S. Mischler, Accelerated tests for coating adhesion life-time estimation in body fluid, in: eCM Online Periodical, Collection. 1; Meet the Expert Implants Conference Abstracts, AO Foundation, Olten, 2018: p. 7.
- 

## CONFERENCE CONTRIBUTIONS

- Swiss Medtech Day 2019, Bern, Interface Stability Assessment and Engineering of Coated Implants (*poster*)
  - Meet the Expert Implants 2019, Olten, Delayed delamination mechanisms of DLC coatings on articulating implants (*poster and extended abstract proceedings*)
  - EuroCorr 2018, Krakow, Crevice corrosion investigations of silicon in simulated body fluid conditions (*oral presentation*)
  - Meet the Expert Implants 2018, Olten, Lifetime estimation of coated articulating implants (*poster and extended abstract proceedings*)
  - EuroMat 2017, Thessaloniki, Delayed delamination mechanisms of DLC coatings on articulating implants (*oral presentation*)
  - EuroCorr 2017, Prague, Crevice and stress corrosion cracking of DLC coated implant interlayers (*oral presentation*)
  - SAOG Meeting, Freiburg, Predicting deterioration phenomena at coating/substrate interfaces (*poster*)
  - Junior EuroMat 2016, Lausanne, Delayed delamination mechanisms of diamond-like carbon coatings on articulating biomedical implants (*poster*)
- 

## INTERESTS

- Drawing, travelling, hiking and Latin dancing

